Effects of Pre-Ionization on the Gas-Puff Z-Pinch

by

Akash Prafulchandra Shah

A dissertation submitted in partial fulfillment
of the requirements for the degree of
Doctor of Philosophy
(Applied Physics)
in the University of Michigan
2022

Doctoral Committee:

Professor Ryan McBride, Chair
Professor Ronald Gilgenbach
Professor Nicholas Jordan
Professor Mahadevan Krishnan
Professor Carolyn Kuranz
Professor Yue Ying Lau

Akash Prafulchandra Shah
akashah@umich.edu
ORCID iD: 0000-0002-5403-8077

ACKNOWLEDGMENTS

This work was supported in part by a seed grant from the Michigan Memorial Phoenix Project and in part by the DOE-NNSA through the SSAA Program under Cooperative Agreement DE-NA0003764.

TABLE OF CONTENTS

LIST OF FIGURES

FIGURE

LIST OF TABLES

TABLE

LIST OF APPENDICES

ABSTRACT

This dissertation presents: (1) the development of a gas-puff z-pinch system for the MAIZE pulsed power facility; (2) experiments carried out to characterize the system's performance on MAIZE; and (3) experiments to test the effects of pre-ionization, if any, on the implosion dynamics, energetics, and current distribution.

Z-pinches rely on the axisymmetric compression of a plasma by driving a current through its axis, a process which can result in efficient x-ray and neutron production. Understanding z-pinches is crucial to studies in nuclear fusion, materials properties, radiation science, and laboratory astrophysics. Gas-puff z-pinches, in particular, rely on the compression of a puff of gas delivered by a nozzle and fast-valve assembly. This dissertation describes the modeling, designing, and construction of such an experiment. The hardware creates a z-pinch target with two concentric hollow shells: an outer-shell with inner radius of 2.0 cm and outer radius of 2.2 cm, and an inner-shell with inner radius of 0.9 cm and outer radius of 1.0 cm. A central solid-filled jet can be added in the future. This experiment is driven by the MAIZE linear transformer driver, which is a 1-MA, 200-ns class current pulse generator. Diagnostics tools fielded include an interferometer, a Rogowski current probe, B-dot current probes, a 12-frame visible light imager, a 4-frame extreme ultraviolet light imager, polycrystalline-diamond x-ray detectors, a bolometer, bubble detectors, and a beryllium probe activation detector.

This dissertation then describes a series of experiments carried out to benchmark the performance of the newly built and integrated experimental platform. In particular, argon and deuterium shots were carried out at different densities in order to establish optimal pinch performance. It was found that when using argon gas for inner-shell-only experiments, total x-ray yields of up to 720 J were observed with strong K-shell signals. When using deuterium gas for inner-shell-only experiments, total neutron yields of up to 4.9×10^8 neutrons were observed. Outer-shell-only experiments were less prolific, in terms of both x-ray and neutron output. Total x-ray yields of only up to 420 J with weak K-shell signals were observed with argon gas. Total neutron yields of only up to 1.8×10^7 neutrons were observed with deuterium gas. It was also observed that the inner shell was useful in stabilizing the outer shell against instability growth when both were pinched simultaneously in a given experiment (i.e., a shell-on-shell stabilized implosion).

With an understanding of the performance of the gas-puff z-pinch, tests were carried out to

study the effects of applying a separate pre-ionization step. Pre-ionization was seeded by emissions from a thin, velvet-tipped copper wire when pulsed with a high voltage. For both inner-shell-only and outer-shell-only experiments with argon gas, it was observed that pre-ionization did not impact current delivered to the pinches early in time, but it did increase current flowing through the pinch at late times. For the outer-shell-only experiment with deuterium, it was observed that pre-ionization resulted in improved current delivery to the pinches and increased neutron yields. By contrast, for inner-shell-only experiments with deuterium gas, it was observed that pre-ionization resulted in increased current losses and decreased neutron yields.

CHAPTER 1

The Pre-Ionization Paradox Presented

Z-pinches can efficiently manufacture high-power x-rays and fusion neutrons, and understanding this process is crucial to various scientific aspirations in nuclear fusion [1, 2, 3, 4], material properties [5, 6], radiation science [7, 8], and laboratory astrophysics [9]. The magnetized liner inertial fusion concept utilizes a z-pinch of a laser preheated fuel magnetized with an axial magnetic field to achieve fusion relevant conditions. The large pressures achieved in a z-pinch are useful for testing the behavior of materials in these extreme conditions such as shock formation. Further the z-pinch allows for developing an understanding of the atomic and plasma physics mechanisms by which x-rays and neutrons are generated in the pinch. Lastly, by taking advantage of plasma scaling laws, the z-pinch can produce laboratory-scale astrophysical plasmas such as accretion disks, white dwarf photospheres, and galactic nuclei. Indeed, the z-pinch is a wonderfully complex and utilitarian tool and the importance of its further study cannot be overstated.

A z-pinch results from the axisymmetric compression of a plasma. A high-amplitude fast-rising current pulse from the discharging capacitors of a pulsed-power generator (e.g., a Marx generator or a linear transformer driver (LTD) [10, 11, 12, 13]) ionizes a cylindrically symmetric "target", allowing it to conduct the current pulse in the axial direction. By Ampère's law, this results in an azimuthal magnetic field. The axial current and azimuthal self-magnetic field produce an inward-pointing Lorentz force, which drives the plasma to the axis of symmetry, where it is further compressed. Examples of such cylindrically symmetric loads that can be z-pinched include wire arrays [14, 15], liners [16], hohlraums [17, 18], dense plasma foci [19, 20], and gas-puffs [21, 22, 23, 24, 25].

The gas-puff z-pinch target consists of an axisymmetric puff of gas, delivered by a nozzle and fast-valve assembly. The fast-valves open and quickly close, which allows gas to flow from a reservoir to the nozzles, where it is distributed in the target region of the pulsed power generator. At this stage of the z-pinch, the gas distribution is non-conducting and must be ionized before it will conduct the current output from the pulsed power generator. With the gas ionized, the circuit of the pulsed power generator is now complete with a conducting target, and the generator discharges into the gas-puff. This forces the ionized gas-puff to accelerate radially inwards, ultimately causing

the gas-puff to stagnate on axis, which typically results in an intense burst of x-rays or neutrons. Figure 1.1 summarizes the chronology of the gas-puff z-pinch. The performance of the z-pinch is sensitive to the initial gas density distribution. Furthermore, the performance of the z-pinch is ostensibly sensitive to the initial plasma distribution that results from the application of a separate pre-ionization step, a study of which is presented in this dissertation.

1.1 Early Pre-Ionization Studies in the Literature

Pre-ionization is the process by which the initial gas distribution in the target region of the pulsed power generator is forced to undergo a phase change from an electrically non-conducting gaseous state to an electrically conducting plasma state. The various methods of pre-ionizing the gas include the use of microwave, electron beam, or ultraviolet irradiation of the gas-puff. Note that such pre-ionizing methods are not strictly necessary for the gas-puff to be pinched: the gas-puff can be ionized when the capacitors of the pulsed power generators start to discharge. At the start of the z-pinch, as the voltage across the electrodes in the target region of the generator reaches a sufficiently high level, in excess of the Paschen minimum associated with the inter-electrode distance and gas density, the gas is forced to ionize. For clarity, this dissertation refers only to the use of an external ionization source— typically electron beam, microwave, or ultraviolet irradiation of the gas-puff— as "pre-ionization".

The effects of pre-ionization on the gas-puff z-pinch are both understudied and paradoxical. Table 1.1 catalogs the studies carried out of the effects of pre-ionization on the performances and dynamics of various gas-puff z-pinches fielded on various pulsed power generators. In general, pre-ionization, irrespective of source, is seen to increase x-ray yield and reduce shot-to-shot variability in the yields. However, higher yields are seen without pre-ionization in some cases. Effects of pre-ionization on the compression of the z-pinch is seen in some cases and not others. Additionally, the z-pinch is stabilized by pre-ionization, but this process is not extensively studied. Effects of pre-ionization on neutron output are not studied. Indeed, these studies demonstrate the need to quantify the effects, if any, of pre-ionization on the implosion dynamics, on the current distribution, and on the x-ray and neutron output of the gas-puff z-pinch. This dissertation attempts to do so.

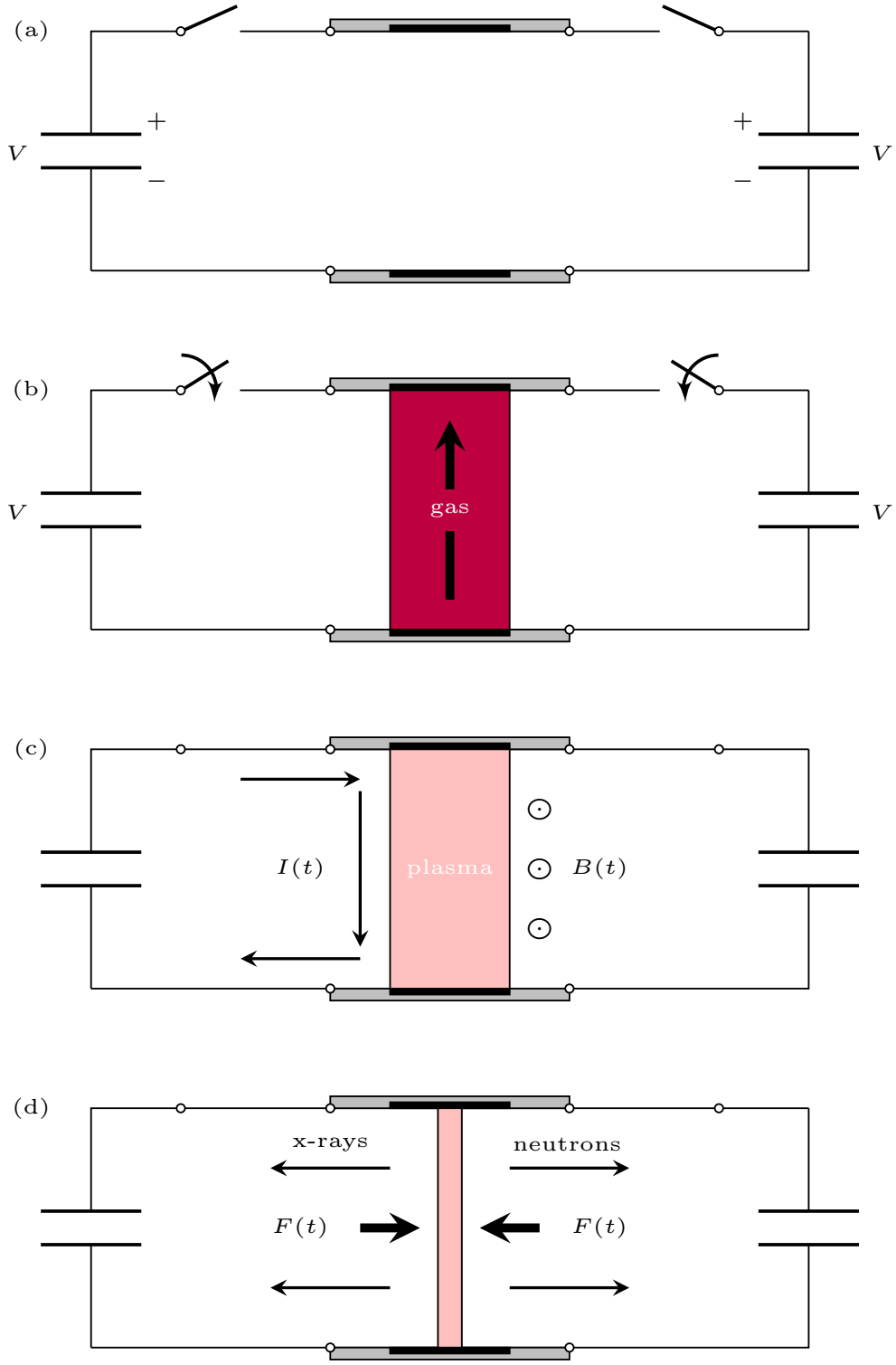

Figure 1.1: Summary schematic of a gas-puff z-pinch. In (a), the capacitors of the pulsed power generator are charged to a potential difference of V. In (b), the gas-puff target is injected by the nozzle and fast-valve hardware from bottom to top. In (c), the gas is pre-ionized and the capacitors that make up the pulsed power generator begin to discharge, which results in a compression of the plasma. In (d), the gas-puff stagnates on axis, resulting in the output of x-rays or neutrons.

Table 1.1: Summary of Early Pre-Ionization Studies in the Literature

No.	Institution	Driver	Nozzle; Radius	Pre-Ionization; Hardware	Results and remarks	Ref.
1	University of California, Irvine	1.5 MA, 1.25 μs	Shell; 20 mm	Electron beam; carbon bristles	Reduced instabilities; higher compression.	[26]
2	Weizmann Institute of Science	1.1 MA, 600 ns	Shell; 19 mm	Electron beam; carbon bristles	Reduced instabilities; increased reproducibility, x-ray yield, and implosion time.	[27]
3	High Current Electronics Institute	1.7 MA, 120 ns	Shell; 30 mm	Electron beam; spark discharge	No change in x-ray yield and compression.	[28, 29]
4	High Current Electronics Institute	1.7 MA, 120 ns	Shell-on-shell ; 30 mm, 14 mm	Microwave; magnetron	Increased reproducibility and x-ray yield.	[28, 29]
5	Naval Research Laboratory	3.0 MA, 150 ns	Solid; 35 mm	Ultraviolet; flashboard	Increased x-ray yield.	[30, 31]
6	Naval Research Laboratory	3.0 MA, 150 ns	Shell-on-jet; 60 mm	Ultraviolet; flashboard	Increased reproducibility; reduced x-ray yield.	[30, 31]

1.2 Scope of Dissertation

To extend previous studies on pre-ionization, this dissertation presents: (1) the development of a new gas-puff z-pinch experimental platform for integration into the MAIZE pulsed power facility at the University of Michigan; (2) the performance of the new gas-puff platform on MAIZE; and (3) the effects of pre-ionization on gas-puff z-pinch performance on MAIZE. These subjects are laid out as follows.

Chapter 1 introduces the the z-pinch and motivates the need for further study of the effects of pre-ionization on the gas-puff z-pinch. A summary of early studies into pre-ionization is given and the reader oriented to the objectives of this dissertation as they relate to these early studies. A summary of findings from this dissertation is also furnished.

Chapter 2 explores the dynamics and energetics of the ideal z-pinch, where an infinitely thin, perfectly conducting liner is pinched. An examination of how the real target that is the gas-puff z-pinch deviates from such an ideal target is detailed. The gas-puff z-pinch is presented as a sequence of four phases: (1) the initialization phase, where the gas flows from the nozzles to form the target; (2) the pre-ionization phase where, the gas breaks down to create an initial plasma distribution; (3) the implosion phase, where the pinch dynamics result in the formation of instabilities; and (4) the stagnation phase, where the pinch energetics result in x-ray and neutron yields.

Chapter 3 details the experimental setup behind the studies presented in this dissertation. The MAIZE pulsed power generator, which is a linear transformer driver that has a current pulse output of up to 1 MA with a rise-time of 200 ns, is presented. The process of developing the gas-puff z-pinch hardware is outlined, including simulating the implosion of gas-puff z-pinches on a MAIZE-like driver, developing the fast-valves and nozzles, designing the transmission lines for integrating the hardware into MAIZE, and fabricating the auxiliary systems that support the gas-puff z-pinch. Finally, the MAIZE diagnostics suite is presented including the new diagnostics developed and fielded for the gas-puff platform, which include a Mach-Zehnder interferometer, an x-ray sensitive polycrystalline-diamond-sensor-array, and neutron sensitive bubble detectors and a beryllium probe activation detector.

Chapter 4 describes experiments conducted to characterize the newly developed gas-puff z-pinch hardware on MAIZE. First, a discussion of fielding interferometry without firing MAIZE is presented. This was done to characterize the neutral gas distribution as a function of the nozzle and fast-valve parameters. From the large parameter sweeps conducted with full z-pinch implosions of both argon and deuterium, a selection of optimum parameters were determined for MAIZE. Experimental results from various gas-puff z-pinch configurations with the outer and inner shells and with both argon and deuterium gases are presented to show optimum performance in terms of pinch timing, x-ray yield, and neutron yield.

Chapter 5 reports on the pre-ionization studies carried out on these optimized pinches, whereby the initial plasma distribution was examined, including its effects on the implosion trajectories, current distribution, and yields. The experimental setup to generate the pre-ionization plasma is described, followed by a presentation of outer and inner shell experiments with both argon and deuterium.

Chapter 6 synthesizes the various threads presented in this dissertation and surveys the future of the field.

1.3 Summary of Results

The main takeaways of the ideas and results presented in this dissertation can be summarized as follows:

1. A new gas-puff z-pinch experimental platform has been developed and integrated into the MAIZE pulsed power facility, alongside a number of auxiliary support systems. The nozzle and fast-valve are designed to produce a nested multi-shell gas-puff target. The system is capable of providing a central jet (with outer radius of 0.8 cm), a concentric inner shell (with inner radius of 0.9 cm and outer radius of 1.0 cm), and a concentric outer shell (with inner radius of 2.0 cm and outer radius of 2.2 cm). While the central jet remains to be added to the system, experiments with the inner and outer shells have been successfully executed.

2. Interferometry was fielded to diagnose the performance of the gas-puff nozzles and fast-valves and to build a relationship of the neutral gas density distribution as a function of the gas pressure in the valves for argon. For deuterium, this relationship is determined from z-pinch experiments rather than interferometry. This allows for translation from units of pressure in the valves to units of density in the target region. Additional diagnostics were installed for experiments where MAIZE was fired to pinch the gas; these diagnostics recorded x-ray spectra, x-ray yields, and neutron yields.

3. Parameter scans were conducted experimentally to find the optimal liner mass for the various gas-puff z-pinch configurations tested on MAIZE. These were either outer-shell-only or inner-shell-only experiments, and they were conducted for argon and deuterium separately. With a stored energy of 5.7 kJ, the optimal soft x-ray yields obtained for argon gas were 420 J for the outer-shell-only experiment (a wall-plug efficiency of 7.2%) and 720 J for the inner-shell-only experiment (a wall-plug efficiency of 12.6%). The optimal neutron yields obtained for deuterium gas were 1.8×10^7 neutrons for the outer-shell-only experiment and a 4.9×10^8 for the inner-shell-only experiment.

4. An electron beam irradiation technique was used to test the effects of pre-ionizing the gas. This was accomplished using a velvet-tipped copper wire, pulsed with a high voltage. The pre-ionization coupled 6.5 J of energy into the gas-puff experiment prior to firing MAIZE. The results suggest that argon z-pinches are largely insensitive to the pre-ionization. By contrast, deuterium outer-shell-only experiments resulted in increased current delivered to small radius and increased neutron yield, while deuterium inner-shell-only experiments resulted in decreased current delivered to small radius and decreased neutron yield.

Ultimately, this work surveys only a small portion of the physics-rich field of z-pinches. This dissertation aims to convey the importance of initial conditions on the trajectories and results of the gas-puff z-pinch. An improved understanding of the entirety of the pinch process will prove invaluable in scientific aspirations as related towards nuclear fusion, material properties, radiation science, and laboratory astrophysics. With known initial mass density distribution and known initial plasma density distribution, simulations can be benchmarked and tested against experiments, which improves their predictive capabilities. It is hoped that the research presented here is used as inspiration for more detailed studies in the future.

CHAPTER 2

The Z-Pinch

2.1 Ideal Z-Pinches

To envisage the dynamics and energetics of the gas-puff z-pinch, we consider an ideal z-pinch, which we examine from the first principles of electrodynamics. Here, the implosion employs a perfectly conducting and infinitely thin shell, through which the capacitors of the pulsed power generator are discharged. The force on a charged particle is given by the Lorentz force law,

$$\mathbf{F} = q\left(\mathbf{E} + \mathbf{v} \times \mathbf{B}\right) \tag{2.1}$$

where q is the particle charge, $\mathbf{E}$ is the electric field, $\mathbf{v}$ is the particle velocity, and $\mathbf{B}$ is the magnetic field. $\mathbf{E}$ and $\mathbf{B}$ are solutions of Maxwell's equations, which, in differential form, are given by

$$\nabla \cdot \mathbf{E} = \frac{\rho}{\epsilon_0} \tag{2.2}$$

$$\nabla \cdot \mathbf{B} = 0 \tag{2.3}$$

$$\nabla \times \mathbf{E} = -\frac{\partial \mathbf{B}}{\partial t} \tag{2.4}$$

$$\nabla \times \mathbf{B} = \mu_0 \mathbf{J} + \mu_0 \epsilon_0 \frac{\partial \mathbf{E}}{\partial t} \tag{2.5}$$

where ϵ_0 is the permittivity of free space, μ_0 is the permeability of free space, ρ is the volume charge density, and $\mathbf{J}$ is the areal current density.

Given the perfect conductor assumption, $\mathbf{E} = 0$ and $\frac{\partial \mathbf{E}}{\partial t} = 0$, simplifying Eq. 2.5 to Ampère's law gives

$$\nabla \times \mathbf{B} = \mu_0 \mathbf{J} \tag{2.6}$$

which, in integral form, is given by

$$\oint \mathbf{B} \cdot d\mathbf{l} = \mu_0 \iint \mathbf{J} \cdot d\mathbf{a} \tag{2.7}$$

where **B** is integrated along a closed path, and **J** is integrated over the surface area enclosed by the same path, as shown in Fig. 2.1. The total machine current, I, flows axially along the thin shell of radius r. This gives

$$\mathbf{J} = \frac{I}{2\pi r}\delta(r' - r)\hat{\mathbf{z}} \tag{2.8}$$

where we distinguish between the free variable, r', and the location of the thin shell, r. Therefore $\delta(r'-r)$ ensures that the current is isolated to the infinitely thin shell (note that the units of $\delta(r'-r)$ are $\left[\frac{1}{\mathrm{m}}\right]$ to give units of **J** as $\left[\frac{\mathrm{A}}{\mathrm{m}^2}\right]$, an areal current density, as expected). Assuming a cylindrically symmetric system, an axial current results in a constant azimuthal magnetic field, B_θ, at a given radial distance, r. The left side of Eq. 2.7 then reduces to

$$\oint \mathbf{B} \cdot d\mathbf{l} = \int_{\theta=0}^{2\pi} B_\theta r' d\theta = 2\pi r' B_\theta \tag{2.9}$$

Given the current distribution of Eq. 2.8 and the area enclosed by the path integral of Eq. 2.9, the right side of Eq. 2.7 reduces to

$$\mu_0 \iint \mathbf{J} \cdot d\mathbf{a} = \mu_0 \int_{r'=0}^{r'} \int_{\theta=0}^{2\pi} \frac{I}{2\pi r}\delta(r' - r) r' dr' d\theta = \begin{cases} 0 & \text{if } r' < r \\ \mu_0 I & \text{if } r' \geq r \end{cases} \tag{2.10}$$

B is then given as

$$\mathbf{B} = B_\theta \hat{\boldsymbol{\theta}} = \begin{cases} 0 & \text{if } r' < r \\ \frac{\mu_0 I}{2\pi r'} & \text{if } r' \geq r \end{cases} \tag{2.11}$$

Rewriting Eq. 2.1 as a force per area, or pressure, on the liner surface, and substituting in Eq. 2.8 and Eq. 2.11 gives

$$\frac{\mathbf{F}}{A} = \frac{1}{2}\left(\mathbf{J} \times \mathbf{B}\right) = -\frac{\mu_0 I^2}{8\pi^2 r^2}\hat{\mathbf{r}} \tag{2.12}$$

which acts on the shell in a radially inward direction, to compress it [32]. With the directions of the various vectors known, we consider the implosion as a one dimensional scalar problem for simplicity of notation. The dynamics of the implosion can be derived by noting that

$$\frac{F}{A} = \frac{m}{2\pi r h}\ddot{r} = -\frac{\mu_0 I^2}{8\pi^2 r^2} \tag{2.13}$$

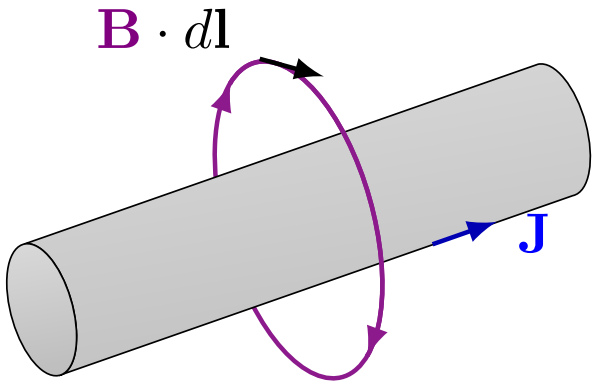

Figure 2.1: A long current-carrying cylinder with current density **J**, which creates an azimuthally symmetric magnetic field **B**. When $\mathbf{B} \cdot d\mathbf{l}$ is integrated along a closed path (as shown), the result is proportional to the current enclosed by the path, as given by Ampère's law.

where h is the length of the liner [33]. This implies

$$\hat{m}\ddot{r} = -\frac{\mu_0 I^2}{4\pi r} \tag{2.14}$$

where we define $\hat{m}$ as the mass per unit length. Solving Eq. 2.14 for $r(t)$ by imposing a current pulse, $I(t)$, gives the radial trajectory of such an ideal pinch. This ideal thin-shell model is solved computationally and the algorithm is given in Appendix B.1. Figure 2.2 illustrates the trajectory of two such ideal pinches: one with $r(t=0) = 2.2$ cm and $\rho = 1.3 \times 10^{-6}$ g·cm^{-3}; and the other with $r(t=0) = 1.0$ cm and $\rho = 16 \times 10^{-6}$ g·cm^{-3}. Note that we integrate these densities over the volume of a real distribution (i.e., the distribution from the nozzles of a gas-puff) and apply the entirety of the mass and driver current at the radius stated. Both are given a current pulse that peaks at 500 kA in 200 ns. While both pinches reach stagnation before peak current, such a model is known to under-predict the stagnation time of a real z-pinch experiment, which we expect to implode slower due to a more radially distributed current density.

In addition to the pinch dynamics, we are typically interested in the pinch energetics. It is generally desired that the energy stored in the capacitors of the pulsed power generator is efficiently coupled to the pinch. Consider the kinetic energy of the shell, which can be determined as follows. First, we multiply Eq. 2.14 by the shell velocity, $\dot{r}$, to give the mechanical power (i.e., the rate of doing mechanical work)

$$\hat{m}\dot{r}\ddot{r} = -\frac{\mu_0 I^2}{4\pi} \cdot \frac{\dot{r}}{r} \tag{2.15}$$

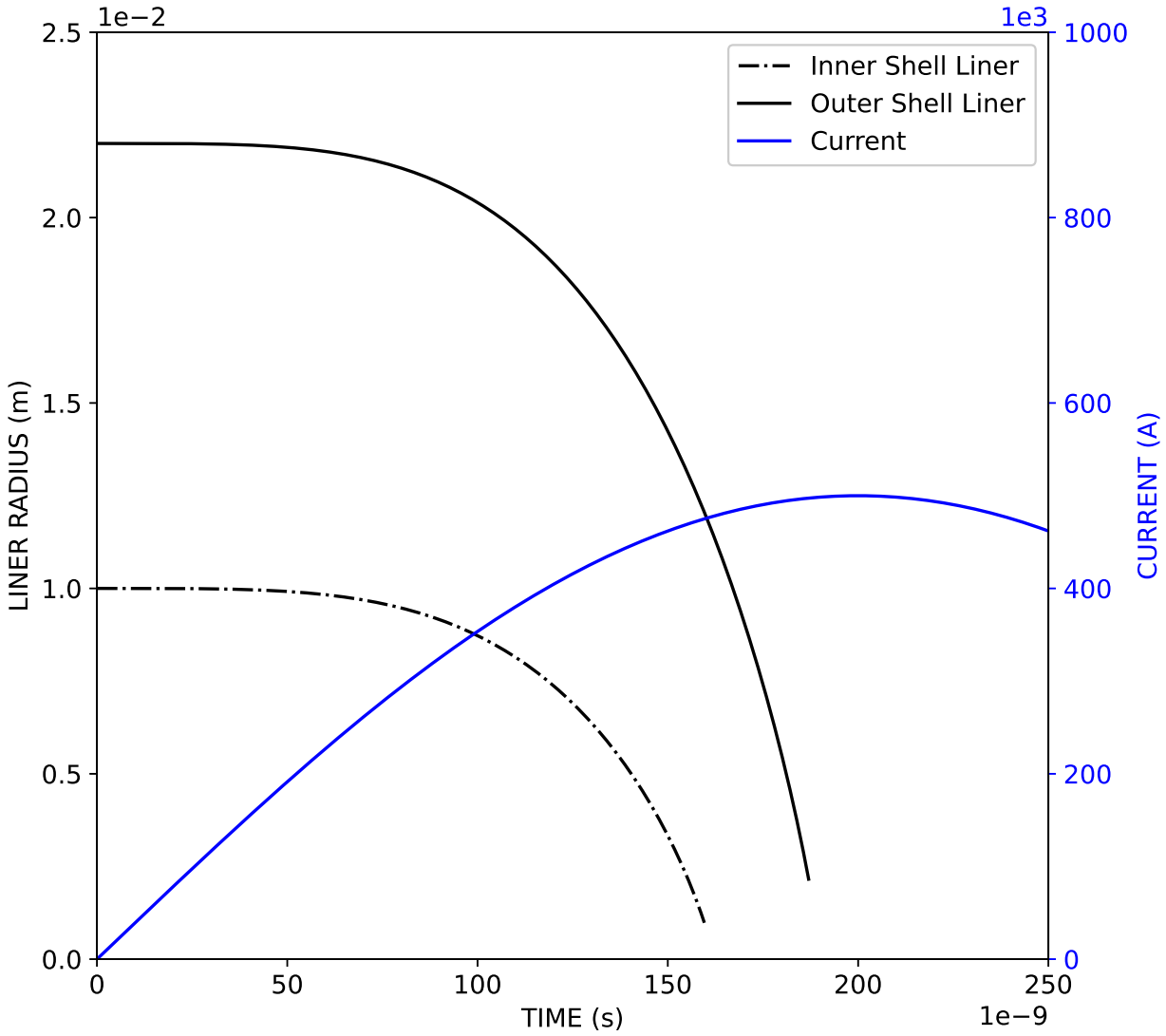

Figure 2.2: Implosion dynamics of two liners driven by a prescribed current pulse. The outer shell is defined by $r_{out} = 2.2$ cm, $r_{in} = 2.0$ cm, and $\rho = 1.3 \times 10^{-6}$ g·cm^{-3}, while the inner shell is defined by $r_{out} = 1.0$ cm, $r_{in} = 0.9$ cm, and $\rho = 16 \times 10^{-6}$ g·cm^{-3}. The current pulse peaks at 500 kA in 200 ns. Each simulation is stopped when the implosion reaches a convergence ratio of ten, which is typical for gas-puff z-pinch implosions. The inner shell stagnates just after 150 ns, while the outer shell stagnates before 200 ns.

Rearranging Eq. 2.15 gives

$$\frac{d}{dt}\left(E_K\right) = \frac{d}{dt}\left(\frac{1}{2}\hat{m}\dot{r}^2\right) = \hat{m}\dot{r}\ddot{r} = -\frac{\mu_0 I^2}{4\pi}\cdot\frac{\dot{r}}{r} = -\frac{\mu_0 I^2}{4\pi}\frac{d}{dt}\left(\ln\left(r\right)\right) \tag{2.16}$$

where E_K is the kinetic energy of the shell. Consider a pinch that implodes from some initial radius $r = r_i$ at time $t = t_i$ to some final radius $r = r_f$ at time $t = t_f$. The kinetic energy acquired by the shell when it reaches r_f can be determined by integrating Eq. 2.16 from $t = t_i$ to $t = t_f$. This is done by noting that

$$E_{K,f} = \int_{t=t_i}^{t_f}\frac{d}{dt}\left(E_K\right)dt = -\int_{t=t_i}^{t_f}\frac{\mu_0 I^2}{4\pi}\frac{d}{dt}\left(\ln\left(r\right)\right)dt \tag{2.17}$$

and integrating by parts. The final kinetic energy is then given by

$$E_{K,f} = \frac{\mu_0}{4\pi}\int_{t=t_i}^{t_f}\frac{dI^2}{dt}\ln\left(\frac{r(t)}{r_f}\right)dt \tag{2.18}$$

Note that the implosion time, t_f is dependent on the shell mass, $\hat{m}$.

To optimize the kinetic energy delivered to the implosion as a function of the shell mass, take the partial derivative of the final kinetic energy with respect to the shell mass in Eq. 2.18 and set it equal to 0. This is shown by

$$\frac{\partial E_{K,f}}{\partial \hat{m}} = \frac{\mu_0}{4\pi}\int_{t=0}^{t_f}\frac{dI^2}{dt}\cdot\frac{1}{r}\cdot\frac{\partial r}{\partial \hat{m}}dt = 0 \tag{2.19}$$

where we note that $\frac{\partial r}{\partial \hat{m}} > 0$ because a heavier liner implodes slower than a lighter liner, and therefore a heavier liner always has a larger radius at a given time in the implosion. If t_f is less than or equal to the time of peak current, then $\frac{dI^2}{dt} > 0$ and Eq. 2.19 is always positive. However, if t_f is taken to be after peak current, then $\frac{dI^2}{dt} < 0$, and a t_f can be found such that $\frac{\partial E_{K,f}}{\partial \hat{m}} = 0$. To optimize delivery of driver energy to the pinch, the mass of the pinch must be selected such that the implosion stagnates at some point just after peak current.

Note that while this ideal z-pinch model imposes a driver current, $I = I(t)$, it is advantageous to couple the dynamics of the pinch to the pulsed power generator circuit [34]. This can be useful because the imploding pinch can alter the geometry of the circuit sufficiently to alter the current delivered by the generator. Such a model is developed in Sec. 3.2. Additional features can also be implemented, where we consider the equilibrium of the stagnated z-pinch on axis (Bennet equilibrium [35]); the driver current needed to sustain radiation output from the stagnated pinch (Pease-Braginskiĭ current [36]); a finite mass distribution where additional gas is swept up as the thin shell implodes (the snowplow model [37]); and the formation of a shockwave ahead of the

imploding liner (the shock model [38]). This discussion serves to emphasize the fact that the model presented above disguises a tremendous amount of physics that constitutes a real z-pinch.

2.2 Gas-Puff Z-Pinches

A three dimensional imploding plasma column is an immensely complex physical object. This section briefly investigates the real gas-puff z-pinch and how it differs from the ideal z-pinch presented above. The gas-puff z-pinch is examined as a sum of four related, yet distinct phases: (1) the initialization phase, where the neutral gas is injected into the load region of the pulsed power generator (Sec. 2.2.1); (2) the pre-ionization phase, where the initial plasma distribution is formed from the neutral gas distribution (Sec. 2.2.2); (3) the implosion phase, where the plasma begins to pinch (Sec. 2.2.3); and (4) the stagnation phase, where the z-pinch forms on axis, emitting x-ray and neutron radiation (Sec. 2.2.4).

2.2.1 Initialization Phase

The first step in the gas-puff z-pinch is to produce the neutral gas distribution that will be pinched. The neutral gas is supplied by a reservoir and stored in the plenum of the fast-valve and nozzle assembly, which is sealed off from the nozzles by the fast-valve. The fast-valve must open and close quickly such that sufficient gas flows into the nozzles to form the target but not so much gas that the vacuum conditions of the experiment are negatively impacted. The fast-valve is electrically controlled using a fast-rising current pulse from a capacitor discharge. The gas flowing out of the fast-valve is accelerated by flowing through a region of choked flow in the throat. The gas exits the plenum at the sound speed of the gas, which is a function of its temperature and species. It is typically accelerated to supersonic speeds by the throat. The gas flows into the nozzle from the throat. The supersonic speed of the gas flow from the throat ensures an axially uniform distribution: the gas at the plane of the nozzle is similarly distributed as the gas closer to the anode mesh above the imploding region. The shape of the nozzle further ensures an azimuthally symmetric gas distribution. Note that unlike the infinitely thin shell model of Sec. 2.1, the mass of the liner has a finite radial distribution.

2.2.2 Pre-Ionization Phase

With the gas-puff z-pinch target formed with an electrically non-conducting neutral gas distribution, it must undergo a phase change to an electrically conducting plasma state to provide a current channel across the electrodes to complete the pulsed-power circuit prior to being pinched. Consider first the case where the driver itself creates the initial plasma distribution. When the capacitors of

the pulsed power generator begin their discharge process, the voltage across the electrodes in the target region of the pulsed power device rapidly increases. Electrons seeded in the target region by ionization are accelerated towards the anode. With typical neutral gas number density distribution on the order of 10^{16} cm^{-3} to 10^{18} cm^{-3}, and a typical electron scattering cross section with the neutral gas of 10^{-15} cm^2, the mean free path of an electron is much shorter than the inter-electrode distance, which is on the order of 1 cm. Electrons therefore undergo sufficiently many ionizing collisions with the neutral gas to create an electron avalanche.

As discussed in Sec. 2.2.1, the gas-puff hardware initializes the neutral gas distribution with a particular radial distribution given by the performance of the nozzle and fast-valve assembly. Note that the avalanching process described above is dependent on this distribution: too low of a gas density results in insufficient ionizing collisions to create an avalanche, and too high of a gas density results in rapid electron recombination, which also results in insufficient ionizing collisions. With a real gas density distribution, the initial conducting channel is created at the radii where the avalanche formation is favored. The conductivity of the target increases with increasing electron density in the gas-puff. At a sufficiently high conductivity, the driver current is carried along the outer surface of the target as a result of the skin effect. This stems from the fact that perfect conductors cannot accommodate electric fields. The skin depth of the current conducting channel is typically on the order of 10^{-4} cm, which is much smaller than the typical radius of the initial gas distribution of 1 cm. Note that unlike the infinitely thin shell model of Sec. 2.1, the conductivity of the target is finite and changes as a function of time.

Using the initial driver voltage to create this current conducting surface by a breakdown of the gas across the electrodes is a stochastic process. The initial electrons are seeded in an unsystematic fashion as determined by the cathode properties, which impacts its work function, which could impact the implosion dynamics of the pinch. It may therefore be desirable to seed the initial electron distribution using an external source. Note that in this dissertation, the use of an external source is referred to as "pre-ionization". Various pre-ionization techniques include the use of electron beams, microwaves, and ultraviolet radiation. A summary of various mechanisms used in previous studies found in the literature is given in Table 1.1.

2.2.3 Implosion Phase

The pulsed power circuit is now complete with a conducting plasma channel across the electrodes in the target. The Lorentz force that results from the current pulse of the pulsed power generator accelerates the plasma radially inward to form a z-pinch. When imploding, z-pinches are ubiquitously afflicted by the magneto-Rayleigh-Taylor (MRT) instability [33]. Classically, the RT instability is engendered when a heavy fluid is supported against gravity by a light fluid. Perturba-

tions of the interface grow exponentially in time. In MRT, the magnetic field outside the plasma is analogous to the light fluid, and the inward pointing Lorentz force, which results in an inward acceleration of the plasma, is effectively an outward pointing gravitational field. MRT is detrimental to stability and reproducibility in gas-puff z-pinches.

In addition to MRT, gas-puff z-pinches are notorious for encouraging a zippering effect, whereby the implosion of the plasma takes place sequentially in time along the gas-puff column instead of simultaneously at all axial locations between the anode and cathode [39]. Zippering can result from a conical gas outflow from the nozzle or from an axial density profile, which occurs when gas outflow has not reached steady state, and downstream gas densities are lower than upstream gas densities. Like MRT, zippering can be detrimental to gas-puff z-pinches by reducing the power coupled to the plasma at stagnation. Experimentally, zippering can be mitigated by proper timing between the nozzle opening and the pulsed power driver discharging. Note that unlike the assumptions made with the infinite thin-shell model of Sec. 2.1, both MRT and zippering result in an implosion that is not axially symmetric.

2.2.4 Stagnation Phase

As the implosion of the gas-puff z-pinch progresses, the electrical energy stored in the capacitors is converted to kinetic and thermal energy in the imploding liner. At stagnation, portions of the plasma can be heated sufficiently to ionize the inner-most electron energy levels. Additionally, electron beams, generated by local instability mode disruptions in the stagnation column, can knock out inner-shell electrons in the dense plasma on the anode side of the disruption [40]. As outer-shell electrons and free electrons fill these inner-shell vacancies, characteristic x-rays are emitted. During stagnation, this energy is emitted as K-shell x-ray radiation. Experimentally, the K-shell yield as a function of peak driver current has been shown to scale as I^4 for peak current amplitudes below ~ 5 kA and as I^2 for higher amplitudes [27, 41].

With deuterium targets, the gas-puff z-pinch also functions as a neutron source. While more detailed studies are needed, it is generally understood that a large fraction of the neutrons produced in a gas-puff z-pinch are beam-target instead of thermonuclear in origin. Beam-target neutrons are a consequence of high-energy deuterium ions accelerated in regions of extremely high electric fields, typically localized around instability structures. This mechanism can be diagnosed by the anisotropy of the neutron yield, which, in the frame-of-reference of the laboratory, favors the axis of the pinch. Thermonuclear neutrons, on the other hand, have an isotropic distribution. Irrespective of the mechanism, the gas-puff z-pinch neutron yield as a function of peak driver current has been shown to scale as I^4 [42].

Note that both x-ray and neutron yields are also dependent on the geometry of the gas-puff,

the gas species used, and on the rise-time of the driver. Various heuristic models of gas-puff z-pinch implosions have been developed to predict K-shell yields given the relevant parameters, but they have not yet demonstrated the desired reliability [27]. This is primarily because each gas-puff z-pinch experiment has its own complex and idiosyncratic behavior, due to non-ideal and nonlinear physics such as instability growth and current delivery. Therefore, the energetics of the z-pinch (e.g., how electrical energy is coupled to the load and how K-shell yield is affected by the coupling) is difficult to understand from first principles. Note that unlike the thin-shell model of Sec. 2.1, the driver energy does not couple to the target solely as kinetic energy. The entire implosion is in a complex state of flux, with energy input from the driver as kinetic and thermal energy, and energy output from the implosion as various radiation mechanisms as well as complex, and possibly turbulent, plasma flows.

CHAPTER 3

Experimental Configuration

3.1 The MAIZE Pulsed Power Generator

The gas-puff z-pinch experiments that will be presented in this dissertation are fielded on the MAIZE pulsed power generator. As shown in Fig. 3.1, MAIZE is a single-cavity linear transformer driver (LTD) [43, 44]. It consists of 40 capacitor-switch-capacitor "bricks", which are arranged on the outer perimeter of a 3-meter-diameter cylindrical metallic cavity and are connected in parallel to the load. MAIZE is capable of outputting a 1 MA peak-current pulse, with a rise-time of 200 ns when the capacitors in the bricks are charged to ± 100 kV and discharged synchronously into a matched load impedance. This corresponds to a stored energy of 16 kJ. Note that while the MAIZE capacitors are capable of functioning at charge voltages of ± 100 kV, experiments are typically carried out at charge voltages of ± 60 kV to reduce operational stress on the various components of the brick. This corresponds to a stored energy of approximately 5.7 kJ. To deliver the desired current pulse to the load, it is crucial that the discharge of the 40 bricks is well-timed relative to each other. A novel implementation of diagnosing the timing of the discharging bricks is presented in Appendix A [45].

The current output from the bricks is conducted to the load region with a radial-to-conical low-inductance transmission line. The conical section of the transmission line allows for the load to be elevated from the plane of the bricks to a plane that allows for diagnostic access. In addition to the current path to the load, there exists an undesirable parallel current path between the capacitors of a brick, as shown in Fig. 3.2. It stems from the unique structure of an LTD, whereby all of the pulsed power components are housed in a metallic cavity to protect the diagnostics on the outside of the cavity from the electromagnetic pulse and stray fields. The current flowing through the parasitic path is minimized by placing highly ferromagnetic "cores" inside the loop of the undesirable circuit. These cores make the parasitic path a high-impedance path relative to the parallel path to the load. This is due to the high permeability of the cores, making the parasitic path highly inductive. Use of the cores also results in small but non-negligible energy losses due

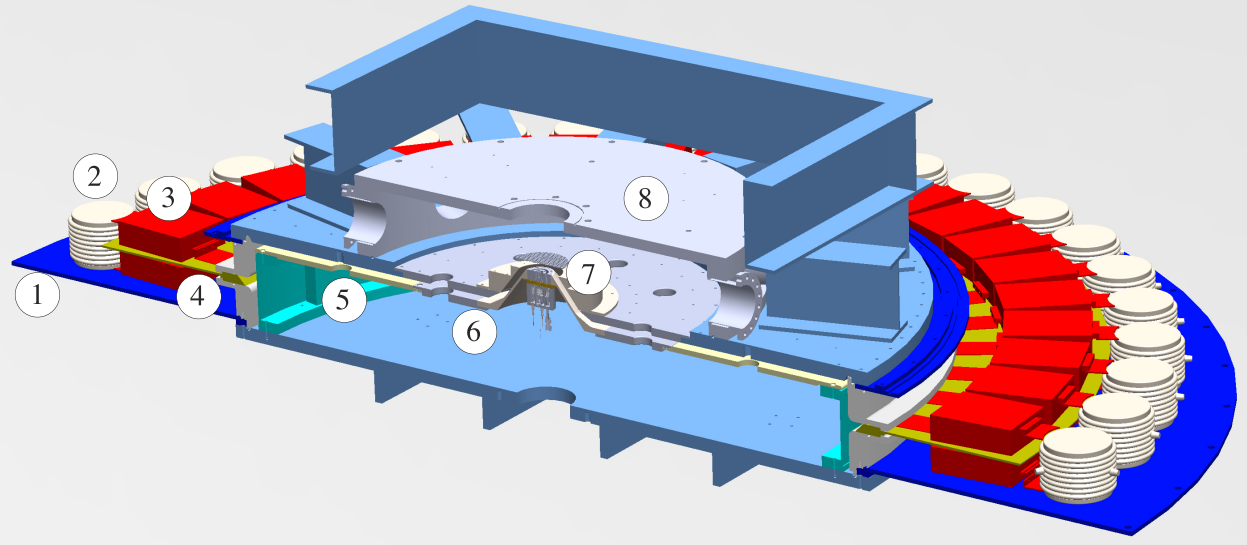

Figure 3.1: A CAD cross-section of the MAIZE LTD showing: (1) oil section, which houses the bricks; (2) spark-gap switch; (3) capacitors; (4) high voltage insulator; (5) radial transmission line section; (6) conical transmission line section; (7) load region (with gas-puff load hardware); and (8) vacuum chamber. Note that the top plate, outer walls of the oil section, and the ferromagnetic cores are not pictured.

to eddy currents and resistive diffusion into the cores, which can be modeled in circuit simulations using a large resistance in parallel with the load.

In summary, the bricks, cores, transmission lines, and load can be modeled by an equivalent RLC circuit. The compact architecture of a single-cavity LTD results in a relatively high total capacitance connected to the load via a relatively low total inductance, and it is therefore considered a low-impedance or "soft" driver. On MAIZE, the total capacitance is 800 nF and the total inductance is approximately 20 nH, which gives a total system impedance of approximately 0.16 Ω. Note that while the total capacitance of MAIZE is always constant, the total inductance, which is a function of the load geometry, can change. The effects of a low-impedance driver can be understood by considering a fast-pinching z-pinch experiment. As the pinch implodes, the geometry of the load region, and therefore the inductance of the circuit, rapidly changes. This distorts the current pulse and imprints an undesirable "inductive dip", which reduces the peak current and, by extension, the Lorentz force driving the pinch. Note that multiple LTD cavities connected in series can lead to a higher impedance or "stiffer" driver, but MAIZE is a "soft" single-cavity LTD. Prior to developing any new experiment for MAIZE, such as a gas-puff z-pinch, it behooves the user to model the circuit as well as the dynamics of the pinch to verify its desired performance.

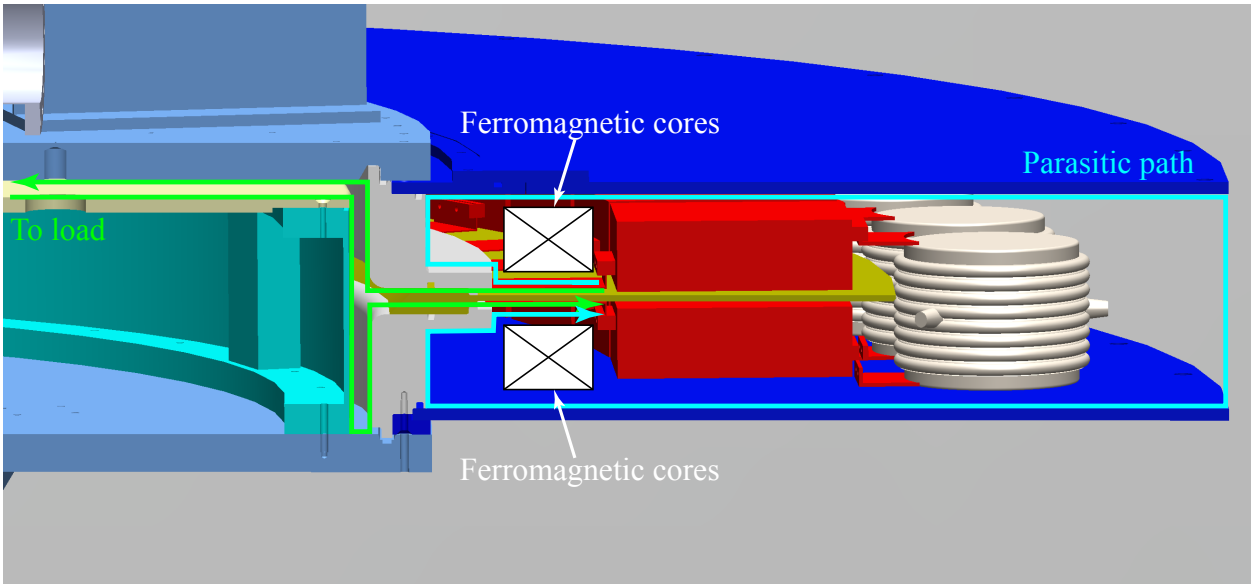

Figure 3.2: There are two possible current paths across the capacitors of a brick: one to the load (shown in green), and another across the top plate, outer ring, and bottom plate, around the ferromagnetic cores (shown in cyan). The former is the desired path and the latter is undesired. The cores add a high inductance to the parasitic current path, forcing the current into the load.

3.2 Gas-Puff Z-Pinch Model on MAIZE

Developing a gas-puff z-pinch requires that we first establish parametric constraints on the density distribution of the gas in the load, such that it can be pinched on a MAIZE-like driver. As discussed in Sec. 2.1, it is understood that the implosion time of the pinch should be roughly equivalent to the current pulse rise time in order to maximize the machine energy delivered to the stagnating plasma column. To this end, the density of the load needs to be tailored to implode when the MAIZE current pulse peaks (i.e., at 200 ns). An over-massed load will implode late in time, while an under-massed load will implode earlier in time, both resulting in inefficient coupling of driver energy to the z-pinch. Such timing considerations inform the nozzle parameters (i.e., the nozzle radius and gas pressure), which determines the density distribution of the gas in the load.

In addition to optimizing delivery of driver energy to the plasma, judicious selection of the density distribution can help in stabilizing the z-pinch. Z-pinches are afflicted by the magneto-Rayleigh-Taylor (MRT) instability, which is detrimental to achieving a stable and reproducible gas-puff z-pinch [33]. Mitigating the growth of the MRT instability can be achieved by using tailored density profiles [46] and multi-species implosions [23, 47]. Both of these instability mitigating methods require multiple nozzles in concentric shells to form a load of nested columns. A density profile with $\frac{\partial \rho(r,z)}{\partial r}$ sufficiently less than zero such that the imploding shell does not accelerate will stabilize MRT. One of the ways in which this can be achieved is by fielding a lighter outer

shell, which implodes onto a heavier inner shell. Multi-species gas-puff z-pinches use an outer shell gas species with higher atomic mass number than that of the gas in the inner shells. These have been experimentally shown to reduce MRT instability modes in addition to promoting yield reproducibility. Note that the zippering effect can be mitigated by ensuring proper timing between the nozzles opening and MAIZE discharging such that there is an axially uniform gas-distribution during the discharge.

In evaluating possible configurations, it was decided that a triple-nozzle system (a central jet surrounded by two concentric shells) would be an appropriate testbed for gas-puff z-pinches on MAIZE, as has been implemented on other drivers [47, 48, 49]. The mass density can be adjusted such that it is highest in the central jet, lower in the inner shell, and lower yet in the outer shell. Additionally, the gas species for each nozzle can be uniquely selected to implode a high-Z gas (such as argon or neon) onto a low-Z gas (such as deuterium). The radii of the triple-nozzle system is informed by similar experiments at peer institutions whereas the gas density has to be selected to best implode on MAIZE. This section develops a simple 0-D voltage-driven thin-shell model to determine these densities.

The thin-shell model couples the implosion dynamics of the z-pinch to the driver circuit via the computational algorithm presented in Appendix B.2. This coupling is of particular importance when considering low-impedance drivers, such as single-cavity LTDs (e.g., MAIZE). As discussed above, the changing load impedance during the course of an implosion can reduce the output current of the driver, to the detriment of the z-pinch experiment. The voltage-driven model was used to determine the implosion trajectory of a gas density distribution in the load. This would inform the gas pressures in the fast-valve that ultimately forms the load. Note that while the model assumes all the mass of the gas distribution is collected at the location of the liner's outer surface, it provides a useful heuristic in predicting the performance of the circuit for a given implosion.

We consider separately the implosion of the two concentric shells of the gas-puff experiment in order to explore possible nozzle radii and mass distributions. The outer shell is tested with $r_{out} = 2.2$ cm, $r_{in} = 2.0$ cm, and $\rho = 1.3 \times 10^{-6}$ g·cm^{-3}. Similarly, the inner shell is tested with $r_{out} = 1.0$ cm, $r_{in} = 0.9$ cm, and $\rho = 16 \times 10^{-6}$ g·cm^{-3}. In particular, r_{out} is the radius of the outer surface of the shell while r_{in} is the radius of the inner surface of the shell. The model assumes the mass distribution in the shell is collected at the outer surface, to which it applies the driving magnetic pressure. Both shells are given MAIZE-like driver parameters and they experience an implosion as shown in Fig. 3.3. These parameters result in the stagnation of the gas-puff z-pinch just after peak current for each of the shells, suggesting an efficient coupling of the driver energy to the implosion. Note that this voltage-driven model is still an ideal thin-shell model, and thus it generates implosion trajectories that are faster than those observed in actual z-pinch experiments.

Note that fine adjustment of the pressures in the fast-valve can be used to change these densities

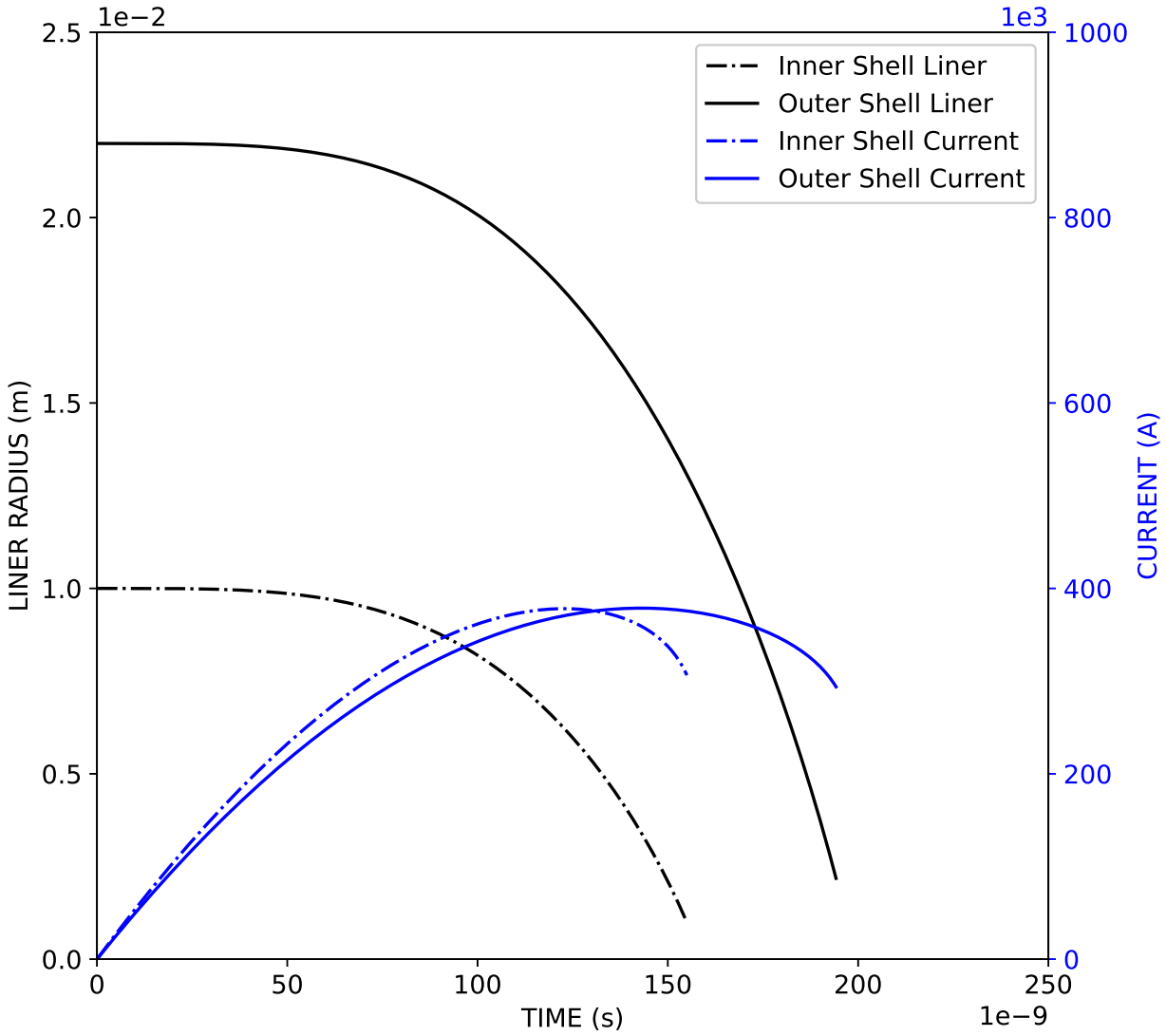

Figure 3.3: Implosion dynamics of the outer (top) and inner (bottom) shells given MAIZE-like driver parameters. The outer shell is defined by $r_{out} = 2.2$ cm, $r_{in} = 2.0$ cm, and $\rho = 1.3 \times 10^{-6}$ g·cm^{-3}, while the inner shell is defined by $r_{out} = 1.0$ cm, $r_{in} = 0.9$ cm, and $\rho = 16 \times 10^{-6}$ g·cm^{-3}. The MAIZE capacitors are charged to ± 60 kV. Each simulation is stopped when the implosion reaches a convergence ratio of ten, which is typical for gas-puff z-pinch implosions. The inner shell stagnates just after 150 ns, while the outer shell stagnates just before 200 ns.

to better time the implosion in an experimental setting. In particular, a gas-puff z-pinch experiment will not have the entirety of the mass of the liner located at a specific radial location but will instead be radially distributed. Further note that while the model implodes each shell individually, adjustment of the gas pressures with both shells present will also result in a well-timed implosion on MAIZE. The implosion model supports the fact that MAIZE can be coupled to the gas-puff z-pinch with reasonable efficiency.

3.3 Gas-Puff Z-Pinch Hardware

Details of the nozzle and fast-valve hardware are discussed in Sec. 3.3.1. Mounting this new hardware onto MAIZE required a redesign of specific sections of the transmission lines on MAIZE, and this process is discussed in Sec. 3.3.2. A CAD cut-out of the nozzle and fast-valve assembly, mounted onto the redesigned MAIZE transmission lines, is shown in Fig. 3.4. Additional auxiliary systems that support the experiment include: a gas manifold, which supplies the fast-valve with gas that ultimately forms the load (Sec. 3.3.3); a fast-valve driver, which sends a current pulse to the fast-valve so as to open and close the valve (Sec. 3.3.4); and a logic circuit, which ensures the presence of gas in the load region in order to avoid an inadvertent discharge of the MAIZE capacitors into an open circuit (Sec. 3.3.5). A summary schematic of the entire network is shown in Fig. 3.5.

3.3.1 Gas-Puff Nozzle and Fast-Valve

The nozzle and fast-valve system function to produce a gas-puff load with a specific gas density distribution. These critical hardware components were manufactured by Alameda Applied Sciences Corporation (AASC) [50]. Note that while the objective is to develop a triple-shell gas-puff experiment, the manufactured hardware currently only has the inner and outer shells enabled, while the central jet can be added at a future date. Currently, the nozzles and fast-valve system are being used to create a z-pinch load with two concentric shells.

Before the gas is injected into the load region of MAIZE, it is stored in the plenum, a section of the valve that is sealed off from the vacuum chamber. The plenum is pressurized by a gas line that is connected to a gas bottle through the gas manifold. This plenum pressure determines the load density profile. Each of the two valves (one for the outer shell and the other for the inner shell) in our system has a unique and independently pressurized plenum. In order for the valve to create a gas flow that results in a well-formed and symmetrical gas distribution, it must open and close quickly.

A rapid response from the fast-valve is achieved by actuating a highly inductive coil by driving

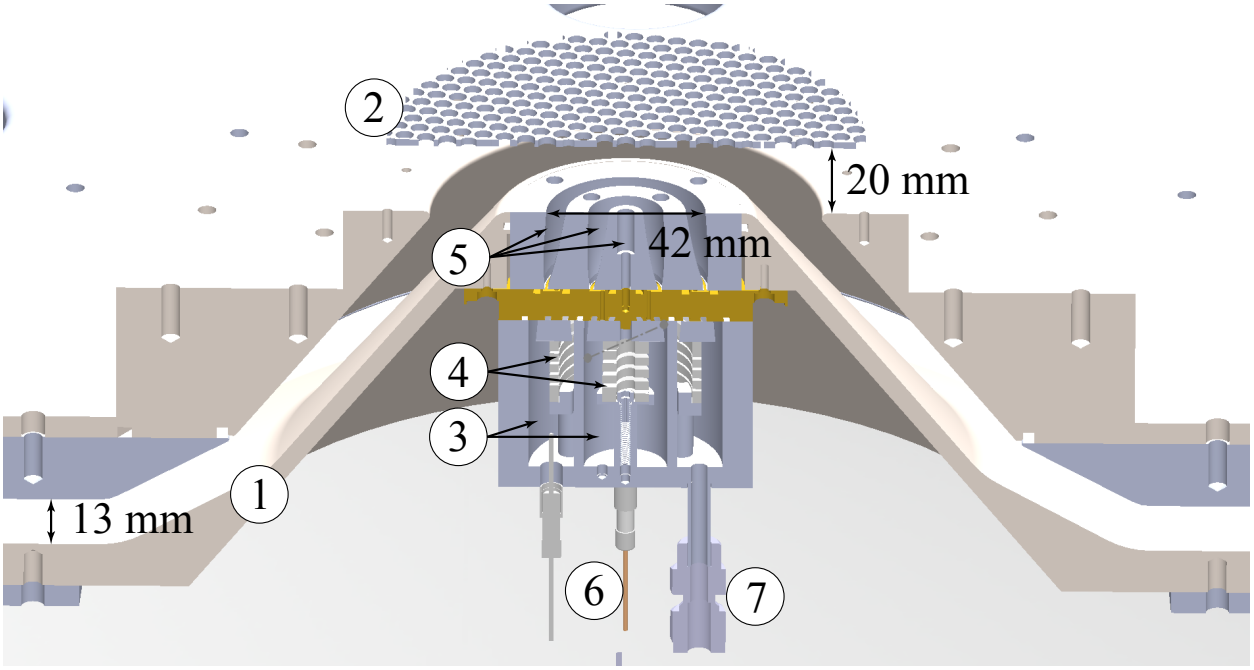

Figure 3.4: A CAD cross-section rendering of the MAIZE load region showing: (1) redesigned MAIZE conical transmission lines with a 13 mm gap along their entire length; (2) anode metallic mesh 20 mm above the cathode; (3) outer shell and inner shell plena; (4) outer shell and inner shell inductive coil; (5) outer shell, inner shell, and central jet nozzles; (6) inner shell electrical connection; and (7) outer shell gas connection. Note that the central jet plenum and inductive coil can be installed in the future.

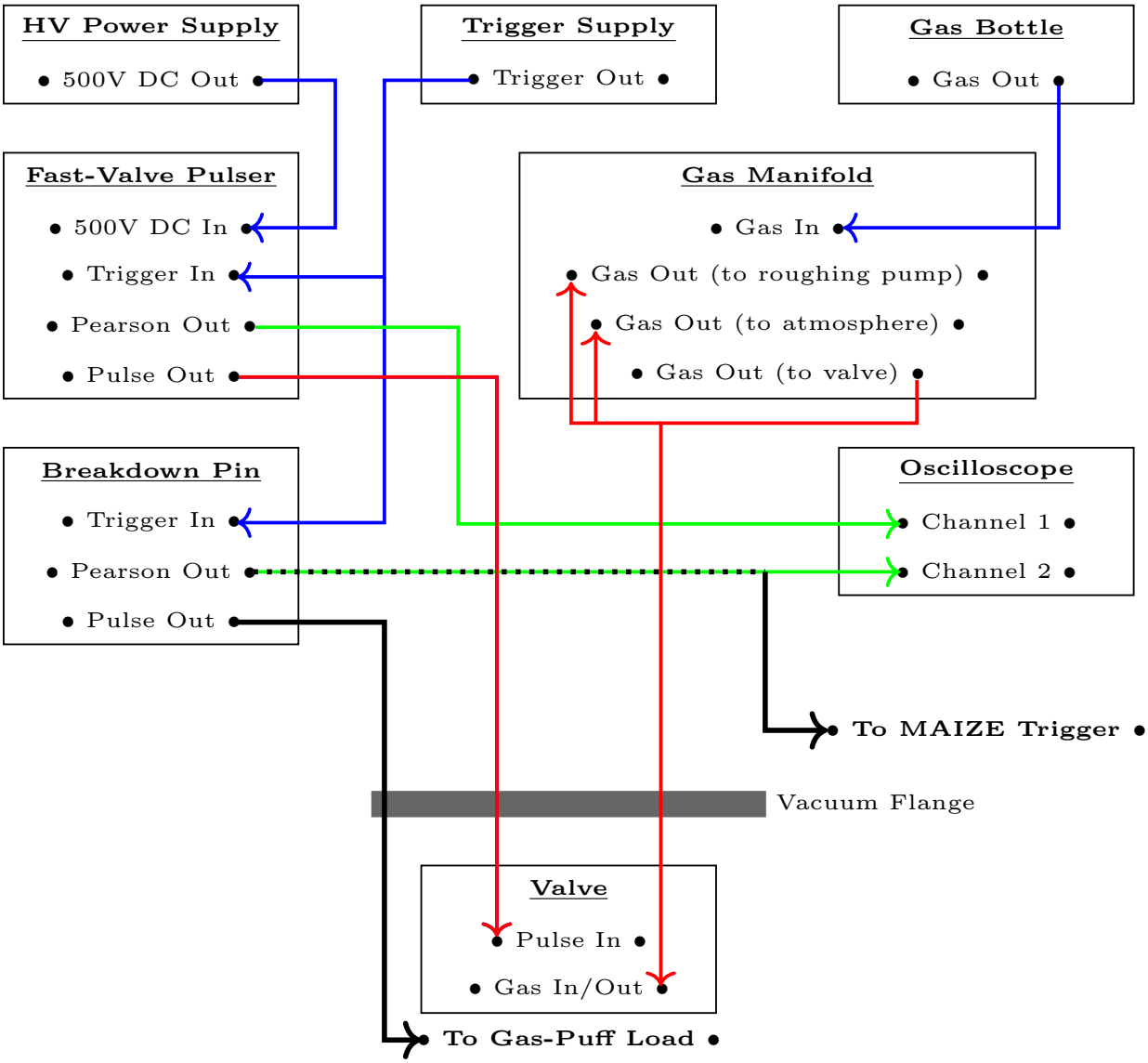

Figure 3.5: A schematic of the overall gas-puff z-pinch system on MAIZE, showing how the various subsystems are connected. Note that two separate HV power supplies and fast-valve drivers are used to drive each valve independently. Additionally, the gas manifold has a unique input and output for each of the two fast-valves. The output of the breakdown pin circuit feeds through a Pearson coil, the signal of which is used to trigger MAIZE and its diagnostic suite with the appropriate time delays.

a current pulse through the coil. Specifically, the valve is designed such that the coil presses against an o-ring on a metallic plate to seal the plenum from the downstream vacuum chamber. Driving a current with a sufficiently fast rise-time through the inductive coil induces an eddy current in the metallic plate, which in turn induces a repulsive force between the coil and the metallic plate and causes the low-mass coil to accelerate away from the plate. This movement of the coil breaks the seal and allows gas to flow out of the plenum. As the current pulse decays, the restoring force of the spring returns the coil to its original position to reseal the plenum. Note that the nozzles and fast-valve function similarly to those developed for the Z pulsed power facility at Sandia National Laboratories [50].

As gas flows out of the plenum, it is forced through a throat-plate, which is an aperture that defines an area of choked flow to accelerate the gas to supersonic velocities. For our system, a single throat plate with a separate aperture for each shell is used. The throat plate controls the azimuthal symmetry of the gas in the load region, and so it demands high precision in its fabrication. AASC used a laser to cut the throat plate in a thin stainless steel foil and then verified the tolerances by digitizing an image of the throat plate and using image processing software to ensure a sufficiently high degree of azimuthal symmetry.

From the choked flow in the throat plate, the gas flows into the nozzle. The geometry of the nozzle pieces ensures an azimuthally uniform, non-turbulent gas-flow and density distribution in the load region of the pulsed power device. The nozzle has an inward tilt, which minimizes the divergence of the gas-flow as it emerges from the nozzles into the vacuum chamber. Such a non-divergent and supersonic flow ensures that the gas rapidly and uniformly bridges the gap between the anode and cathode, completing the pulsed power circuit for a z-pinch experiment.

3.3.2 Transmission Line

For the MAIZE current pulse to flow along the transmission lines and through the gas-puff load, the nozzle and fast-valve have to be physically integrated into the MAIZE circuit. Specifically, this requires merging the nozzle and fast-valve assembly into the MAIZE transmission lines. In theory, a pulsed power device can be manufactured with only radial transmission lines. However, due to the azimuthal distribution of capacitors and switches, such a design severely limits diagnostic access to the load region. This problem is overcome by axially elevating the load region from the capacitor plane to a diagnostics plane, generally defined by the vacuum chamber ports [51].

The price for an axial translation of the transmission lines for diagnostic access is an increase in circuit impedance. Specifically, these elevated transmission lines have a higher inductance, which is a function of their geometry. MAIZE is a low-impedance driver, so it is important that the transmission lines be designed such that their inductance is minimized. An optimized power feed

is curved, which can be reasonably approximated by a straight conical feed [32]. On MAIZE, the transmission lines from the capacitor outputs are primarily radial down to a radius of 15 cm, at which point they transition to the conical structure.

The conical section of the power feed was redesigned to accommodate both the existing radial power feed and the newly fabricated nozzle and fast-valve assembly at the diagnostics plane. To this end, we evaluated the inductance of various conical transmission line geometries, whereby the overall transmission line structure is broken up into smaller, discrete sections that can be easily evaluated using the inductance formula for a coaxial transmission line; the partial inductances from the discrete sections are then summed to find the total inductance of the structure. This process is outlined in additional detail in Appendix C. We tested a range of various geometries and selected one after accounting for inductance as well as ease of manufacturing (see Fig. 3.6). The selected geometry has a calculated inductance of 7 nH. Note that this is only the inductance of the conical section— it must be added to the inductance of the rest of the MAIZE discharge circuit, which includes the load, the switches, and the radial section of the transmission lines. Further note that this new low-inductance transmission line is now used for other experiments platforms on MAIZE as well.

On MAIZE, the nozzle and fast-valve system is mounted on the conical section of cathode. The nozzle defines the cathode plane of the gas-puff z-pinch, and a metallic mesh, located 2 cm above the cathode plane, defines the anode plane. The transmission line design maintains a conservative 13-mm gap between the anode and cathode. A conservative gap spacing helps to ensure that stray gas that circulates into the power feed during a gas-puff shot sequence will not close the large A-K gap in the transmission lines and reduce the driver current at the load. Note that the MAIZE current flows along the nozzle surface during a shot and can damage the nozzle due to localized heating and arcing. In practice, the nozzles are refurbished, or even replaced, after approximately 100 shots on MAIZE.

3.3.3 Gas Manifold

The nozzle and fast-valve must be supplied with gas, which ultimately goes on to form the experimental load for the gas-puff z-pinch. The gas manifold, as shown in Fig. 3.7, is the control unit that supplies gas to the two plena of the two corresponding fast-valves (one plenum for each shell). To this end, the gas manifold has two inputs and two outputs. Gas bottles supply the inputs of the manifold and are selected for the gas species desired for each particular shell. Note that if the two shells of the z-pinch are to be constructed from the same species, then a single gas bottle can supply both inputs of the manifold by teeing off a single line from the bottle. Also note that gas regulators at the output of the gas bottles are unique to the species of gas stored in the bottle. Care

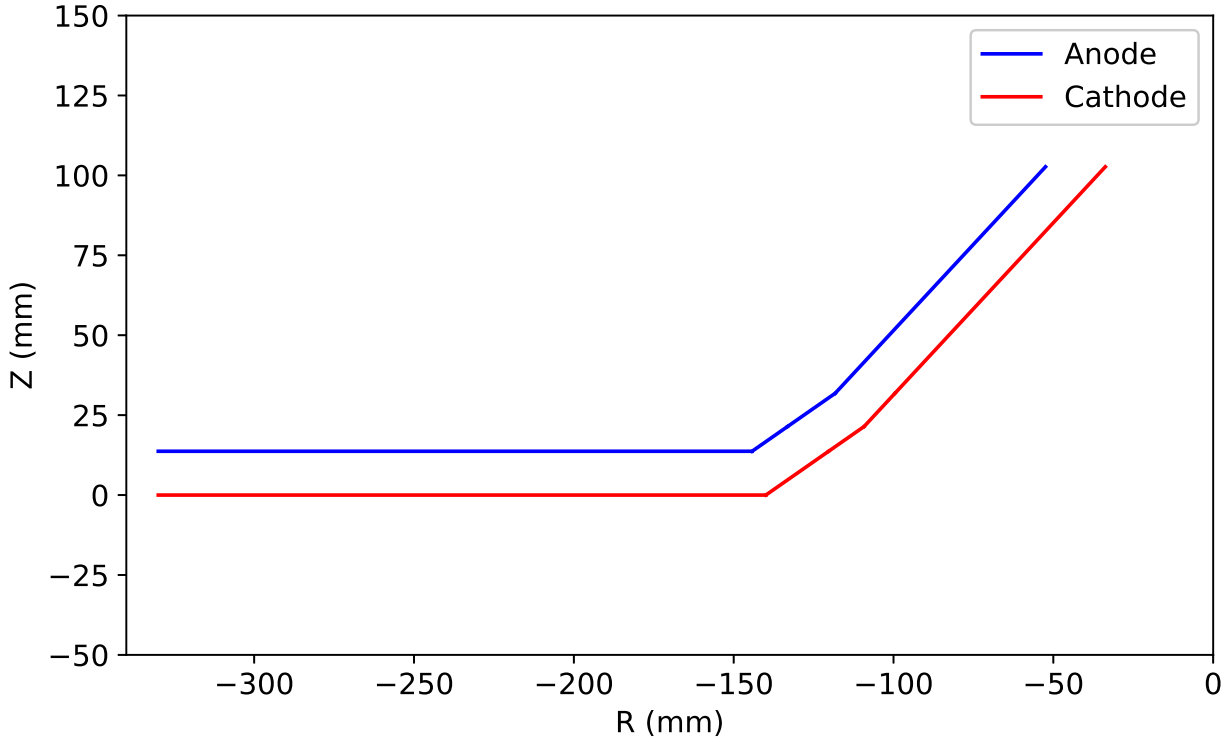

Figure 3.6: Transmission line geometry as designed in Python. The transmission line is designed to fit into the radial portion of the transmission line and elevate the gas-puff hardware to the diagnostic plane in a straight conical shape. The inductance of the transmission line is 7 nH as calculated by numerical integration of infinitely small coaxial subdivisions of the design.

must be taken to ensure appropriate regulator size is in use for each gas bottle.

Each of the inputs in the gas manifold flows through a valve to the output. Opening the output valve allows gas to flow to the plenum of the fast-valve; leaving the output valve open for a sufficiently long time ($\sim$ 10 s) will equalize the pressure of the plenum to that set on the output of the gas bottle. A pressure gauge is placed on the output end of the manifold to indicate the gas pressure in the plenum. On each of the plena outputs in the manifold, two additional parallel paths are constructed for the gas from the bottles to flow along: one through a valve to a vacuum roughing pump, and the other through a separate valve to atmosphere. The former allows the plena to be pumped down, and the latter allows the plena to be vented to atmosphere. Note that we use aluminum lines to allow the lines to be pumped down below atmospheric pressure.

During initial setup of the fast-valve pressures using the gas manifold, we first close off the output valves to isolate the gas bottle from the plena. We then evacuate the plena by opening the roughing valves. We open the output valves to fill the plena with the desired gas. Repeated pumping down and filling of the plena with the desired gas is advised to dilute trace contaminants such as air or previously used gas species. After sufficient flushing out of contaminants, the output valve and roughing valve are tweaked to achieve the desired plena pressure. After the experiment is completed, the vent valve can be used to bring the plena to atmosphere. The gas manifold allows for precise control of the plena pressures, which in turn determines the desired density distribution of the gas-puff z-pinch.

3.3.4 Valve Driver

In addition to precise plena pressures, the rapid opening and closing of the fast-valves is also required in getting the desired gas density in the load region of MAIZE. As discussed above, a current pulse sent to the fast-valves actuates an inductive coil to break a seal in the plenum through which gas flows out and into the nozzles. As the current pulse decays, it resets the seal for the next shot. This current pulse is provided by the fast-valve driver. The fast-valve driver consists of a capacitor, which is charged to a positive voltage of 600-700 V by a high-voltage power supply. The capacitor is discharged by the closing of a switch, which is triggered by a 5-V pulse. The current pulse profile is characterized by the impedance of the inductive coil in the valve. Due to the geometry of the valves for the inner and outer shells, the inductive coils which form the seal in their respective shell have a different inductance. A unique capacitor voltage is required to achieve the proper opening and closing of each of the two valves, and so each valve has its own driver and high-voltage power supply.

Note that the cables connecting the drivers to the nozzle and fast-valve system, which is mounted onto the cathode in the vacuum chamber, create an alternate and undesirable current

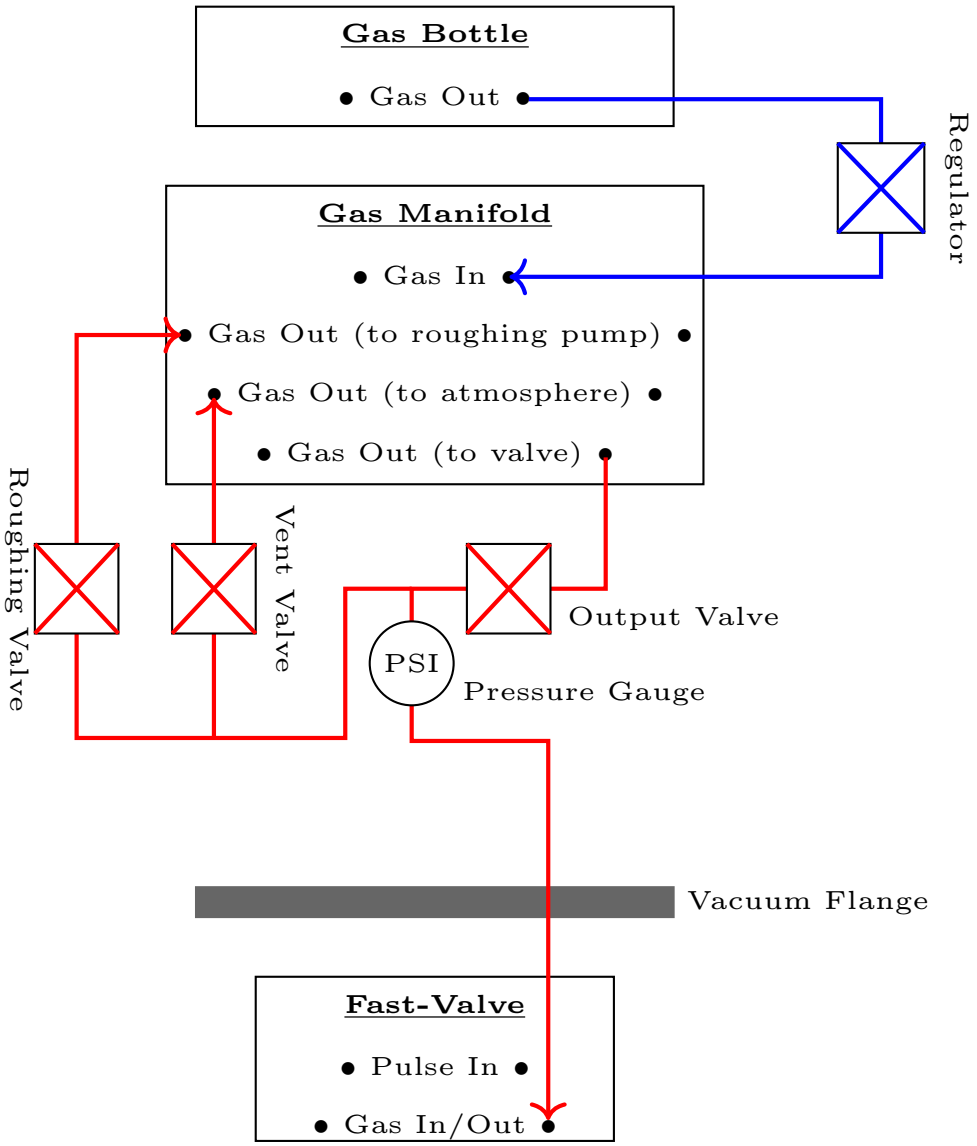

Figure 3.7: Schematic of the gas manifold. The manifold allows for precise control of the gas pressure in the plenum of the fast-valve with the output valve. It also allows for cleaning out the plenum prior to the experiment taking place with the roughing valve and venting the plenum after the experiment is over with the vent valve. Note that there are two separate manifolds for each of the two shells to ensure independent control of the pressures and gas species in each shell.

path that conducts a fraction of the MAIZE pulse back to the drivers. The MAIZE current can flow along the ground braids of the coaxial cables that connect the valve-drivers to the fast-valves. To avoid this, we ensure that the MAIZE circuit, including the nozzle and fast-valve system, is inductively isolated from the valve-drivers by feeding the power and gas lines that supply the nozzles and fast-valves through a large metallic coil. The power and gas lines are wrapped in a metallic over-braid from the metallic coil to the MAIZE vacuum chamber. Additional care is taken to ensure that the metallic over-braid wraps over the vacuum flange through which the power and gas lines are fed into the vacuum chamber.

3.3.5 Logic Circuit

Prior to discharging the MAIZE capacitors through the double-shell structure of the gas in the load region, we must independently verify the presence of the gas. This verification provides the breakdown logic for MAIZE to fire and is required to ensure that the pulsed power device does not discharge into an open circuit, in the unlikely event of a malfunction in any of the large number of components that go into the gas-puff z-pinch experiment. Firing MAIZE into an open circuit can dramatically reduce the lifespan of various electrical components and can occasionally irreparably damage them.

For the MAIZE gas-puff, the breakdown logic is provided by the discharge of a 10-kV, 1-μF capacitor through the neutral gas (see Fig. 3.8). The positively charged capacitor is discharged by closing a spark-gap switch to ground, which results in a negative-polarity pulse. This negative pulse is coupled to the gas through a thin metallic wire, which sits above the anode return current structure. The height that the wire sits at is selected to ensure a breakdown of the gas between the wire and the MAIZE anode. A Pearson coil on the output of the logic circuit provides the trigger signal for MAIZE. This logic circuit will only fire if there is a specific amount of gas through which it can discharge. With the complete development of the gas-puff z-pinch hardware and associated systems integrated into the MAIZE circuit and shot sequence, experiments can be fielded and studied.

3.4 Diagnostics Suite

The MAIZE facility includes diagnostics for neutral densities (e.g., a Mach-Zehnder interferometer), current (e.g., a Rogowski coil and B-dots), plasma imaging (e.g., visible-light self-emission imaging, and extreme ultraviolet self-emission imaging), x-ray radiation (e.g., a bolometer and polycrystalline diamond detectors), and neutron radiation (e.g, bubble detectors and a beryllium probe activation detector). The typical diagnostics setup on a gas-puff z-pinch experiment is shown

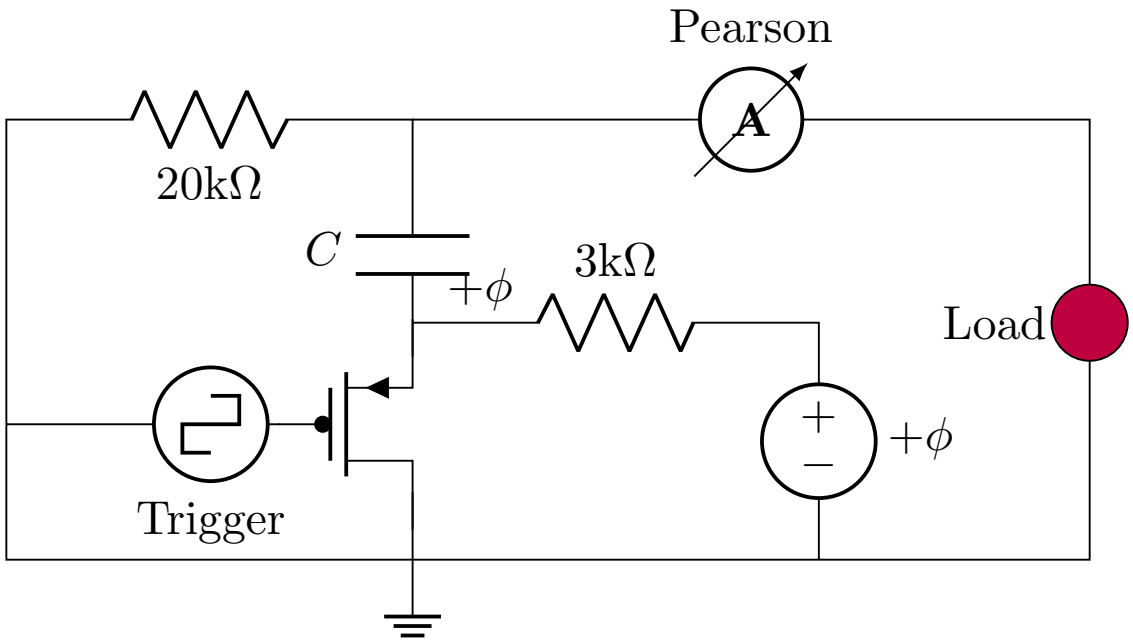

Figure 3.8: The MAIZE logic circuit. A capacitor is discharged through the gas-puff load only when the load has a sufficient density. Monitoring the current output of the capacitor with a Pearson coil provides the trigger signal for MAIZE to fire.

in Fig. 3.9.

3.4.1 Neutral Density

The gas-puff z-pinch hardware produces a neutral gas distribution in MAIZE's target region in the initiation phase of the experiment. We constructed a 2D Mach-Zehnder interferometer with a 532-nm wavelength, 2-ns pulse-width laser beam, which is expanded from 2 mm to 60 mm, split into two equal path lengths, and then recombined to form an interference pattern, as shown in Fig. 3.10. One of the split paths traverses the gas-puff to form the probe beam while the other forms the reference beam. The probe beam experiences a phase change as it crosses the region of a high index of refraction due to the gas in the load region relative to the reference beam. The interference pattern is imaged with a Canon XTi Rebel DSLR camera. An interference image before and during the injection of the gas-puff is acquired.

A computer script was written to analyze the interference patterns and extract the density distribution in the load region. This script is discussed in more detail in Appendix D. We used the interferometer to quantify the evolution of the gas density in the load region with time. This informs the delay between when the nozzles fire and when MAIZE fires. We also used the interferometer to quantify the gas density as a function of the fast-valve pressure. This informs plena

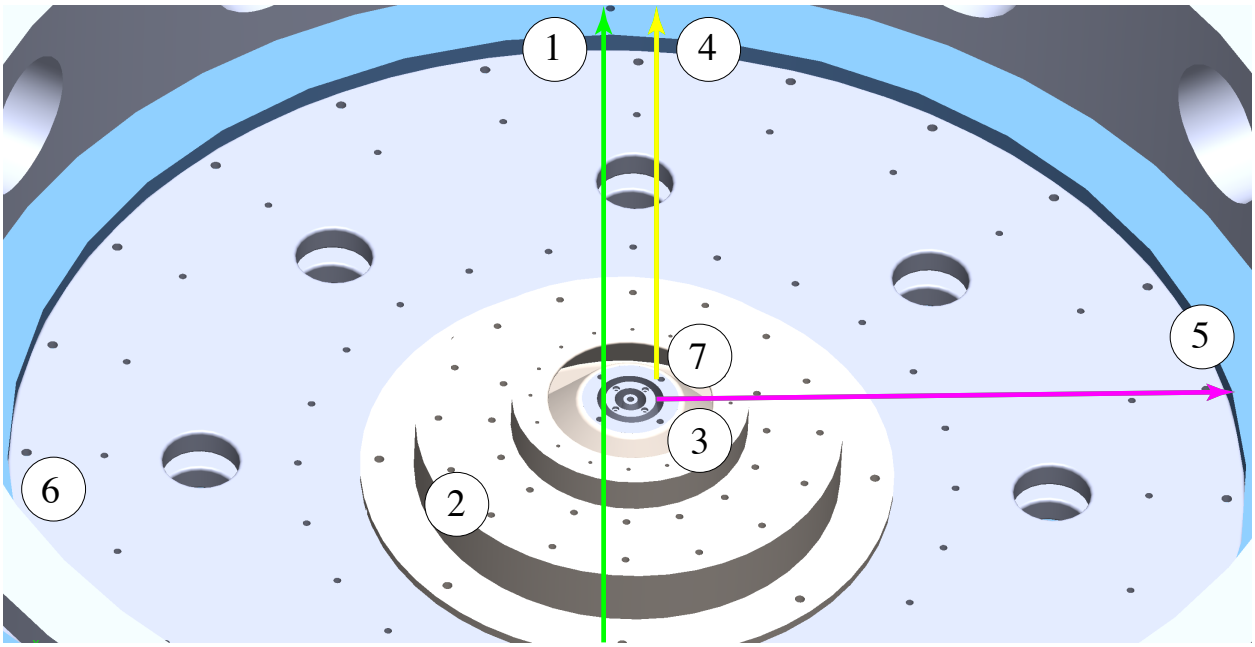

Figure 3.9: The typical diagnostics setup during a gas-puff z-pinch experiment showing the general location and use of: (1) the 2D Mach-Zehnder interferometer for neutral gas density measurements; (2) the anode Rogowski coil and (3) the load B-dot for current measurements; (4) the visible-light self-emission imaging; (5) the extreme ultraviolet-light self-emission imaging; and (6) the nickel bolometer and (7) the PCD array for x-ray measurements. The bubble detectors and beryllium activation probe for neutron diagnostics are placed outside the vacuum chamber.

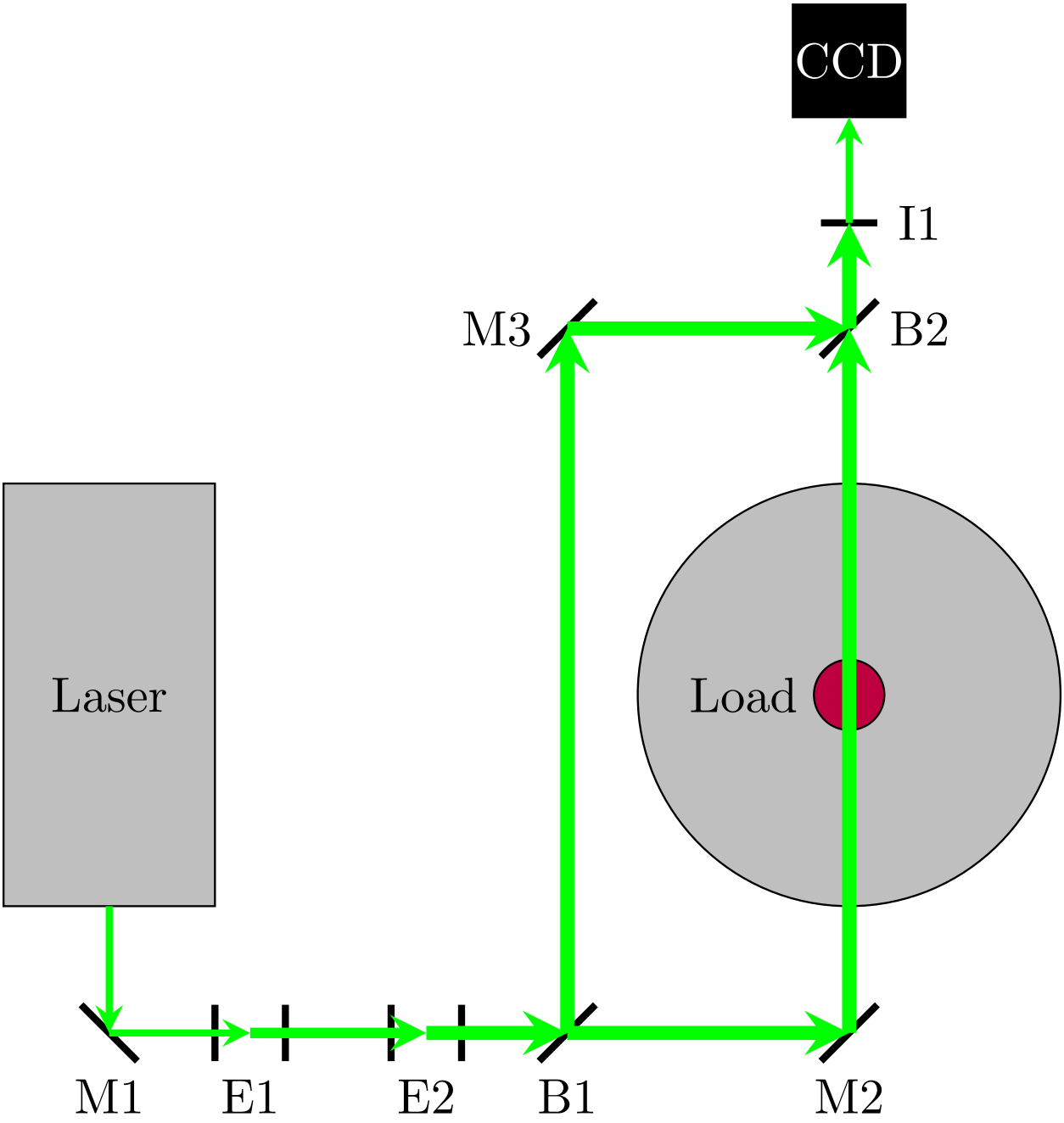

Figure 3.10: A schematic of the 2D Mach-Zehnder interferometer that was developed to characterize the neutral gas density distribution produced by the gas-puff fast-valves and nozzles on MAIZE. The laser outputs a 2-ns pulse-width, 5-mm diameter beam at a wavelength of 532 nm. This beam is aligned to the interferometer with the mirror M1. It is expanded to about 15 mm with the expander E1 and then to about 50 mm with the expander E2. The reference and probe beams are split with the beamsplitter B1. The probe beam is reflected by the mirror M2 and the reference beam by the mirror M3, both recombining on the beamsplitter B2 to form an interference pattern. The imaging lens I1 focuses the interference pattern onto the CCD, which is a Canon XTi Rebel DSLR camera.

pressure to obtain a particular density distribution (i.e., a mass distribution that will implode and stagnate at the time of peak drive current on MAIZE). We determined the optimal time delays and fast-valve pressures for the inner and outer shells separately. Note that the interferometer can also be configured to run during the pinching of the gas-puff to diagnose the plasma characteristics.

3.4.2 Current

MAIZE is discharged after the formation of the gas-puff target. The MAIZE load current is measured using a Rogowski coil, which consists of a helical winding of a wire with the lead at one end returning to the other end through the center of the helices. The entire arrangement is then wrapped to form a torus. The Rogowski coil monitors the current encircled by the torus. Its operating principle is based on the generation of a potential difference across the ends of the coil, which is proportional to the *change* in magnetic flux within the area of the torus. Since the shape of the coil is static, the time-rate-of-change of the magnetic flux is detected, which, in turn, is proportional to the *change* in current flowing through the torus. Note that this signal must be integrated to determine the current. On MAIZE, the Rogowski coil is located on the inner edge of the anode such that all the current flowing across the cathode is entirely encircled by the torus.

The current is also measured using B-dot probes. Similar to the Rogowski coil, these consist of a simple wire loop, which pick up the time-rate-of-change of the magnetic flux through the area of the loop, which is proportional to the time-rate-of-change in current. Note that the orientation of the B-dot to the current is slightly different than the Rogowski coil. While the current flows through the latter, no current flows through the former. Rather, the B-dot is located at the radius of an Ampèrian loop through which the current flows. For the experiments in this dissertation, the B-dots were located at a particular radius from the center of the gas-puff z-pinch, to diagnose the current flowing through the target during the experiment.

3.4.3 Plasma Imaging

In the pre-ionization, implosion, and stagnation phases of the gas-puff z-pinch, the plasma emits light in the 400-700 nm wavelengths. The dynamics of each of these stages is diagnosed by visible-light self-emission imaging. MAIZE employs an Invisible Vision Ultra UHSi 12-frame fast framing camera to capture the light output from the plasma. The exposure of each of the 12 frames can be set to as low as 5 ns and frame rates as high as 200,000,000 frames per second, which corresponds to an inter-frame time of 0 ns (i.e., back-to-back frames). This allows diagnosis of the plasma dynamics with nano-second temporal resolution, which is critical for an experiment that takes place on the order of the MAIZE current rise-time of 200 ns. A computer code was written to allow the user to define the z-pinch liner edges in order to quantify the implosion trajectory (see

Appendix E).

The implosion and stagnation phases of the gas-puff z-pinch plasma are also characterized by light in the 100-400 nm ultra-violet wavelengths. The dynamics of each of these stages is diagnosed by extreme ultraviolet self-emission imaging. MAIZE employs a four-frame time-gated micro-channel-plate (MCP) camera. Here, light from the pinch passes through one of four pinholes and creates phosphorescence on the MCP, which is imaged with a Canon XTi Rebel DSLR camera. The four pinholes and four MCP channels provides four frames with 5 ns exposure with frame rate of 66,666,666 frames per second, which corresponds to an inter-frame time of 15 ns. Note that this frame rate can be changed by selecting appropriate cable lengths within the MCP power supply. Like the fast-framing camera, this provides the necessary temporal resolution for a z-pinch experiment.

3.4.4 X-Ray

The stagnation phase of the gas-puff z-pinch is characterized by an intense burst of x-rays. MAIZE uses a bolometer to characterize the x-ray yield. A bolometer consists of a metallic strip through which a constant current is passed and which is exposed to the incident x-ray photons. The x-ray radiation deposits energy into the metal, which heats the metal and thus causes the metal's electrical resistivity to change. As a result, the voltage source that supplies the constant current also changes. Monitoring this voltage provides a quantifiable diagnosis of for the total x-ray energy deposited into the metal. In particular, MAIZE employs a nickel-element bolometer, which is sensitive to soft x-rays of energies up to 2 keV.

We set up a filtered array of four polycrystalline-diamond-detectors (PCDs) to help quantify the x-ray spectrum of the output radiation. PCDs consist of two electrodes separated by a diamond fill and biased to about 400 V. X-rays incident on the diamond produce electrons, which are accelerated and collected by the positively biased electrode. Monitoring this voltage provides information on the incident x-rays. Filters with unique sensitivities to x-ray energies can be placed on the PCD to diagnose the x-ray spectrum. In particular, we used PCDs with a 2.5 μm copper and 50-μm polypropylene filter; a 4 μm silver filter; a 5 μm molybdenum filter; and a 10 μm titanium and 50 μm polypropylene filter. Each filter has a unique transparency profile to incoming x-ray photon energies, as shown in Fig. 3.11. Looking at the difference in the amplitude between two PCDs with different filters allows us to acquire coarsely resolved spectral information about the x-rays. For instance, the difference between the signal on the PCD with the 4-μm silver filter and on the PCD with the 5-μm molybdenum filter gives the x-rays in the 2.5 keV to 3.4 keV range, which should capture argon K-shell emission in the 3.0 keV to 3.2 keV range.

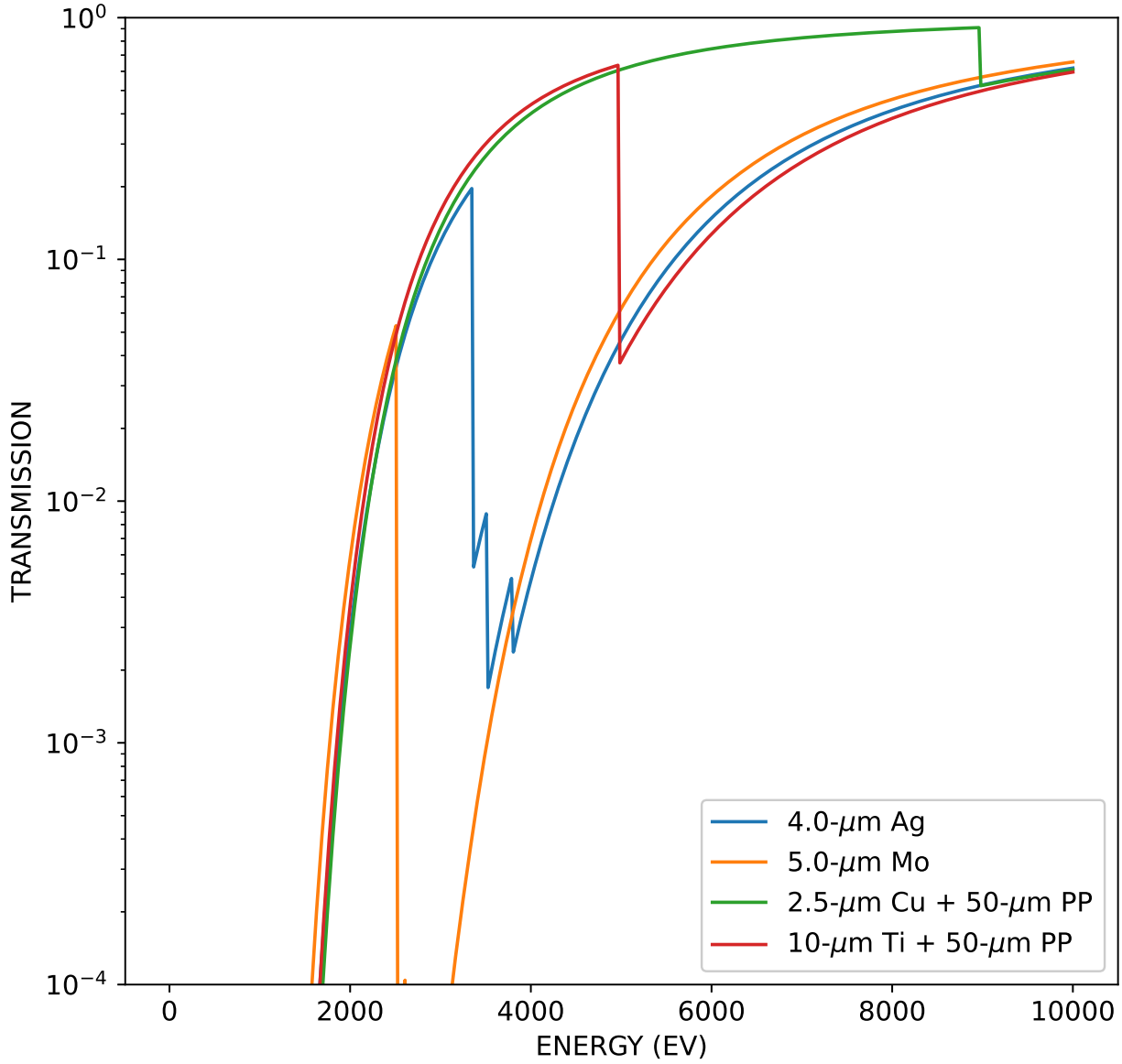

Figure 3.11: Response curves of the filters selected for the array of four PCDs. The differences between the signals recorded for on any two of the PCDs fielded gives the x-ray power for photon energies that are found in the transmission windows formed by taking the differences between the corresponding transmission curves plotted in this figure. This technique provides coarse spectral information.

3.4.5 Neutrons

We also set up an array of neutron bubble detectors and a beryllium probe detector to quantify the neutron output for when we pinch deuterium in the gas-puff z-pinch. Pinching deuterium can result in nuclear fusion reactions (primarily deuteron-deuteron reactions). Approximately 50% of these primary reactions result in the release of a 2.45-MeV neutron. Significant numbers of 2.45-MeV neutrons can be detected with bubble detectors and nuclear activation diagnostics.

Bubble detectors make use of $\sim 10^5$ droplets of super-heated liquid dispersed through a clear $8\ \mathrm{cm}^3$ polymer. Neutrons incident on these pockets perturb the liquid, converting it into a gas in a localized region, forming a bubble in the epoxy. Counting the bubbles in the detector after a pinch event quantifies the neutron yield. Then, knowing the distance of the detectors from the pinch event and the detector sensitivity, the yield can be calculated by

$$Y = \frac{4\pi\alpha b d^2}{\beta} \tag{3.1}$$

where α is a calibration factor, β is the bubble detector sensitivity in bubbles per mrem, b is the bubble count, and d is the distance from the pinch in cm. With the personal neutron dosimetry bubble detectors used, $\alpha = 28.8 \times 10^3$. Note that the $4\pi d^2$ factor is premised on the assumption that the neutron output from the pinch is isotropic. This assumption allows yields to be easily calculated. However, the z-pinch at the 1-MA level largely produces beam-target instead of thermonuclear neutrons; the latter have an isotropic distribution and the former favor the axis of the pinch. We field an array of bubble detectors with low, medium, and high sensitivities both on and off the axis of the pinch. This setup allows us to understand the spatial distribution of the neutron output from the z-pinch, even with the assumption of isotropy in the simplified yield calculation of Eqn. 3.1.

The beryllium activation probe relies on the activation of beryllium to form an unstable ^{6}He isotope, the decay of which releases beta electrons [52]. The beta electrons are absorbed in a plastic scintillator and subsequent visible light pulses are counted using a multi-channel analyzer. Since the counted light pulses are correlated to the output from the ^{6}He decay, the signal forms an exponentially decaying curve. Under proper functioning of the diagnostic, the half-life measured from the decay constant of the curve should be the half-life of ^{6}He, 807 ms. Measuring the initial activity from the curve allows us to calculate the initial production of ^{6}He, which can be extrapolated to the neutron yield using a modified version of Eqn. 3.1.

CHAPTER 4

Benchmarking the Gas-Puff Z-Pinch on MAIZE

4.1 Initial Density Distribution

With the gas-puff z-pinch experimental hardware built and integrated physically into the MAIZE pulsed power generator and its workflow, the next step is to characterize the initial density distribution of the system as a function of its parameters. Specifically, the initial density distribution must be characterized as it evolves in time to determine when to discharge MAIZE. The gas-puff should be pinched when there is a collimated and axisymmetric gas distribution across the anode and cathode in the target region. For example, if MAIZE is fired too early, then the the gas flow may not have fully formed a target just after the opening and closing of the fast-valves. If MAIZE is fired too late, then the gas flow might be uncollimated and asymmetric as a result of expansion a long time after the opening and closing of the fast-valves. The initial density distribution must also be characterized as a function of the plenum pressure to determine the mass of the liner that will be efficiently pinched. Additionally, each of the inner and outer shells of the gas-puff hardware must be characterized.

We use the newly constructed 2D Mach-Zehnder interferometer to this end, as described in Sec. 3.4.1. We characterize the initial density distribution with argon in a series of four experiments to understand the optimal outer-shell timing, the inner-shell timing, the outer-shell plenum pressure, and the inner-shell plenum pressure. The results of the timing experiments for both shells are shown in Fig. 4.1, and the results of the plenum pressure experiments for both shells are shown in Fig. 4.2. For each experimental parameter tested, a pre-shot interference pattern is obtained (i.e., without the nozzles firing) and one or two shot interference patterns are obtained (i.e., with the nozzles firing). For these characterization studies, MAIZE was not fired. Details of image processing are presented in Appendix D. A computer code was written to automate this image processing and was used to determine the mass density distribution. The mass density is then averaged over 50 rows of pixels per image in the axial direction. The error margin is given by the standard deviation of the average density of each of the 50 rows of pixels. Note that if two shot images are obtained,

then the average and standard deviation in the density is determined over a total of 100 pixels. More shots were taken for some experiments to improve the signal-to-noise ratio.

The timing experiments were carried out by maintaining a constant plenum pressure and varying the timing between when the fast-valve fires and when the interference pattern is acquired. The plenum pressure is set at 10 psi for both the inner and outer shells. For the outer-shell, a target is seen forming at 600 μs after the fast-valve of the outer-shell fires, peaking at 800 μs, and then decreasing. We select 700 μs after the fast-valve of the outer-shell fires as the time to discharge MAIZE. Similarly, for the inner-shell, the gas target is seen forming at 300 μs after the fast-valve fires, peaking at 500 μs, and maintaining a steady-state flow. We select 500 μs after the fast-valve of the inner-shell fires as the time to discharge MAIZE.

The pressure experiments were carried out by maintaining a constant timing, as determined by the timing experiments (i.e., 700 μs for the outer-shell and 500 μs for the inner-shell), and varying the plenum pressures. For both shells, there is less gas for both high and low pressures and more gas for intermediate pressures. This is explained by the fact that at very high pressures, there is more force holding o-ring seal against the metallic plate that constitutes the fast-valve, and so it does not open as much as in cases with lower gas pressures. On the other hand, at very low pressures, there is less gas that is puffed into the target region. The full-width-at-half-maximum of the density for each pressure is selected to give the relationship between the plenum pressure and the density distribution, as shown in Fig. 4.3. The pressure can then be selected to form the desired density distribution. For instance, a -13.2 psi argon outer-shell plenum pressure corresponds to neutral density of 0.020×10^{18} cm^{-3} (or 1.3×10^{-6} g·cm^{-3}), while a -4.0 psi argon inner-shell plenum pressure corresponds to neutral density of 0.23×10^{18} cm^{-3} (or 16×10^{-6} g·cm^{-3}). These are the densities tested in the models of Fig. 2.2 and Fig. 3.3 presented above.

Note that these interferometry experiments were carried out with only argon, while we intend to pinch both argon and deuterium. Since deuterium is comprised of much lighter molecules than argron, deuterium's gas flow from the nozzles is faster. Thus, the optimal times for discharging MAIZE after the fast-valves open are shorter for deuterium than argon. For deuterium, we select 500 μs after the fast-valve of the outer-shell fires and 300 μs after the fast-valve of the inner-shell fires as the time to discharge MAIZE. Additionally, deuterium flow as a function of plenum pressure is different than that of argon. As will be discussed in Sec. 4.2, each gas and shell is pinched by firing MAIZE and by sweeping across a range of density distributions. Since the liner mass that corresponds to a particular implosion trajectory is constant and independent of the gas species (note that we did not define the gas species in the models discussed in Sec. 2.1 and Sec. 3.2), the deuterium plenum pressure that corresponds to a particular implosion trajectory has the same mass as that of an implosion with argon. This allows for translation between plenum pressure and density distributions for deuterium, as also shown in Fig. 4.3.

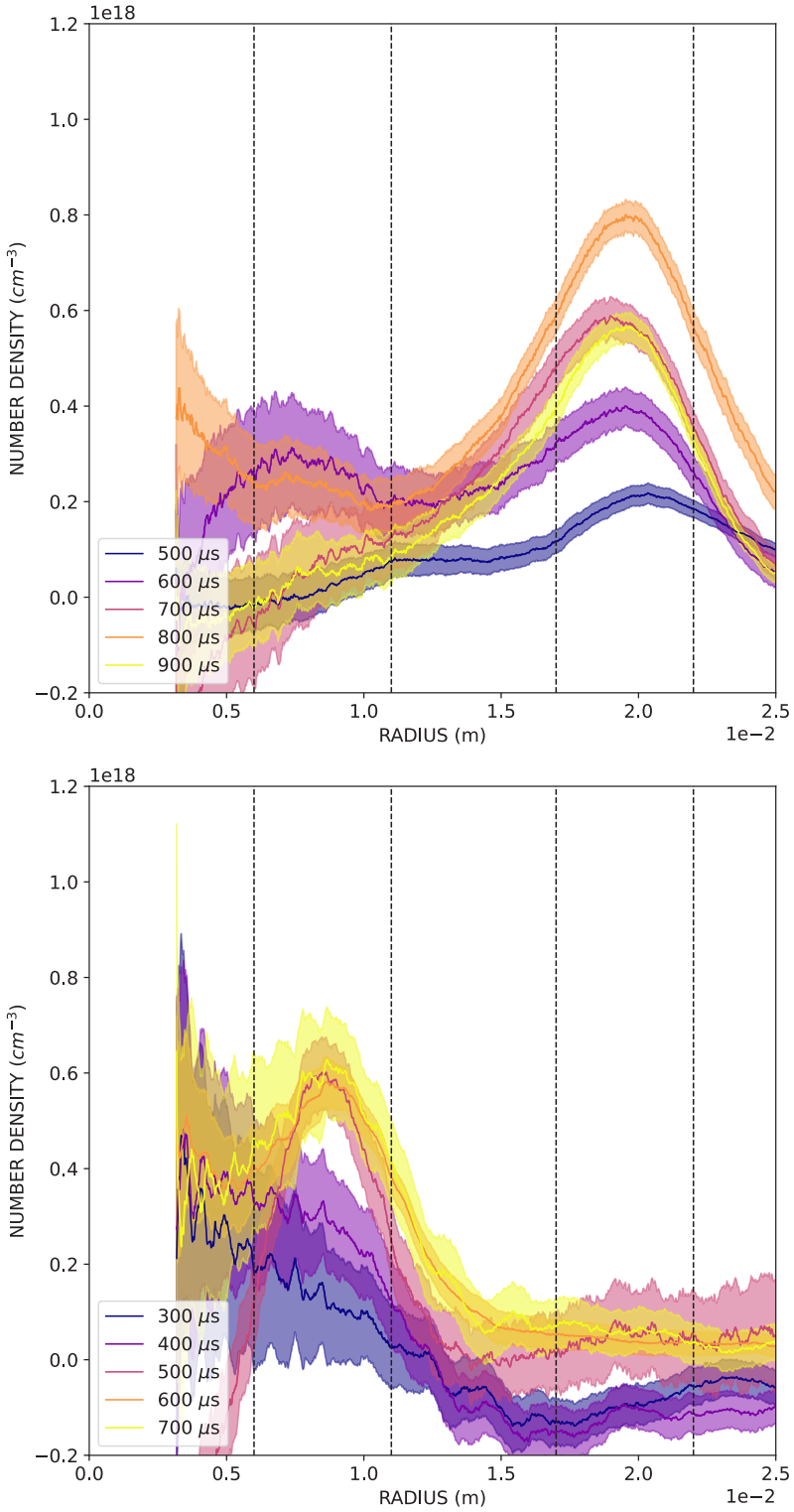

Figure 4.1: Interferometry results from the timing experiments for the outer-shell (top) and inner-shell (bottom). Two shot images were taken for the outer-shell and one shot image for the inner-shell. As can be seen for each experiment, there is little to no gas at earlier times, after which a collimated and steady target forms. From these experiments, the timing is selected as 700 μs for the outer-shell and 500 μs for the inner-shell. For these experiments, only argon gas was used.

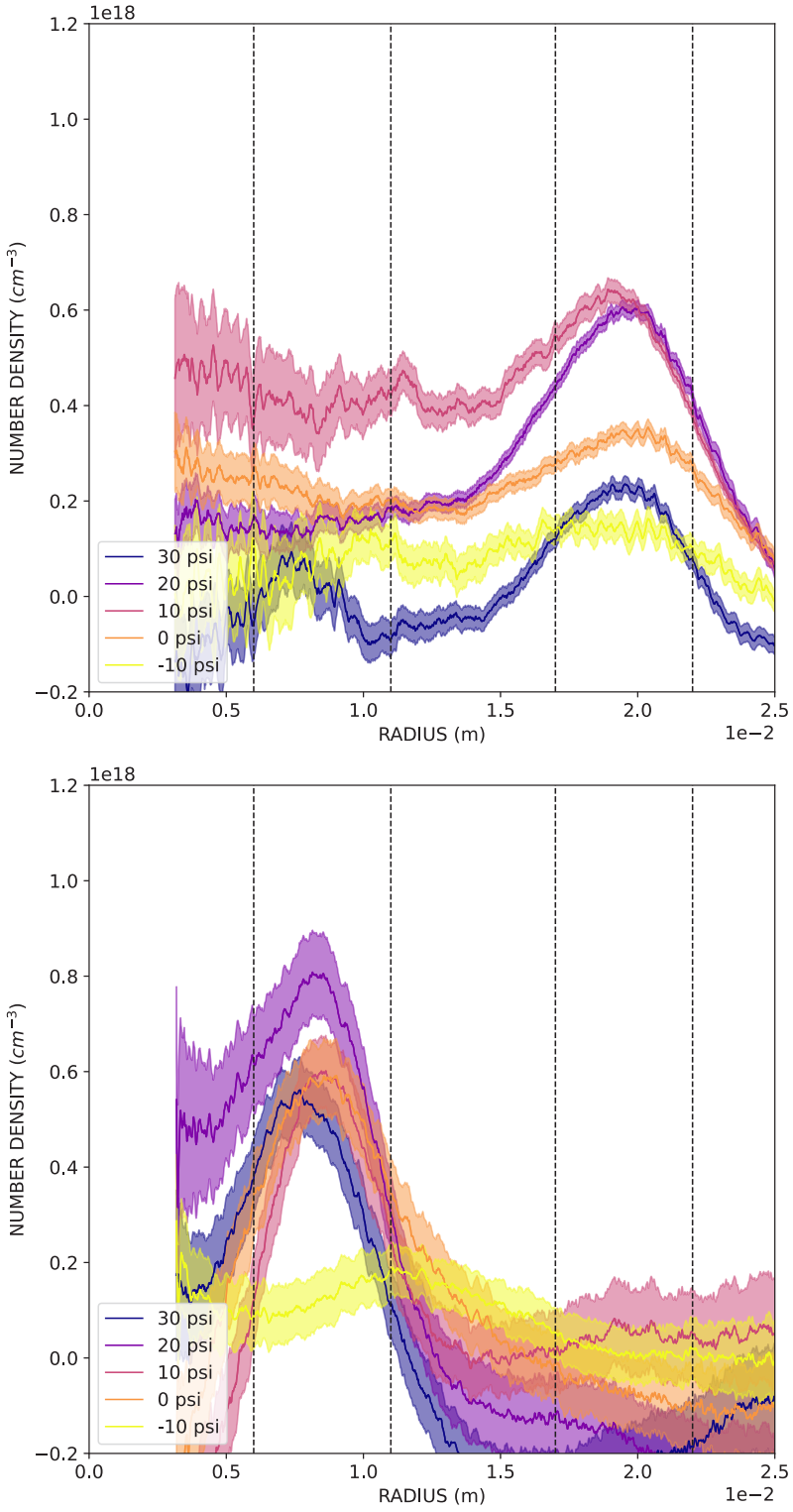

Figure 4.2: Interferometry results from the pressure experiments for the outer-shell (top) and inner-shell (bottom). One shot image was taken for the outer-shell and one shot image for the inner-shell. For these experiments, only argon gas was used. As can be seen for each experiment, there is little to no gas at higher and lower pressures and a lot of gas for intermediate pressures. From these experiments, a relationship between plenum pressure and density has been developed.

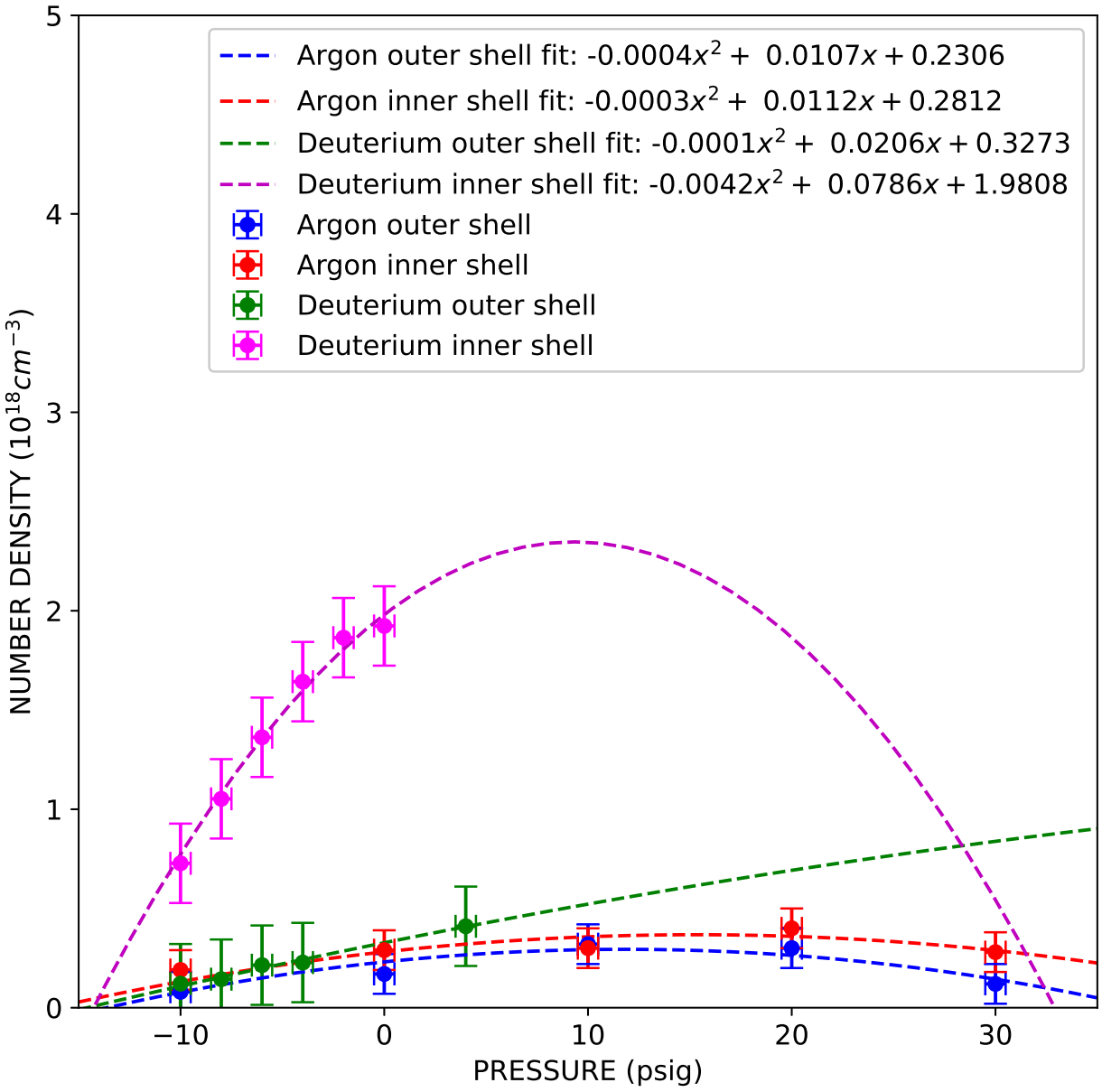

Figure 4.3: Summary of interferometry results giving the relationship between the plenum pressure and the gas-puff neutral number density when MAIZE discharges for argon and deuterium for the outer and inner shells. Note that for these curves to hold for argon, density is measured 500 μs after the inner-shell fast-valve fires, and 700 μs after the outer-shell fast-valve fires, while for deuterium, density is measured 300 μs after the inner-shell fast-valve fires, and 500 μs after the outer-shell fast-valve fires.

4.2 Outer-Shell Gas-Puff Z-Pinch Experiments

After understanding the dynamics of the gas flow of the outer-shell target as a function of the timing and pressure parameters of the fast-valve and nozzles, desired outer-shell densities can be formed for pinching. This section describes the pinch dynamics and energetics of outer-shell z-pinches as these densities are varied for argon, in Sec. 4.2.1, and deuterium, in Sec. 4.2.2. We select a constant 700 μs for argon and a constant 500 μs for deuterium as the time after the fast-valve of the outer-shell fires to discharge MAIZE, which is charged to ± 60 kV for each shot. We then vary the plenum pressure (i.e., the density distributions) for each gas to study how each implosion performs.

4.2.1 Outer-Shell-Only Argon Gas-Puff Z-Pinch Experiments

Outer-shell argon gas-puff z-pinch experiments were carried out with plenum pressures ranging from -12.0 psi to -13.4 psi. Referring to Fig. 4.3, this relates to liner number densities ranging from 0.045×10^{18} cm^{-3} to 0.015×10^{18} cm^{-3}, respectively, or liner mass densities ranging from 3.0×10^{-6} g·cm^{-3} to 1.0×10^{-6} g·cm^{-3}, respectively. In particular, the plenum pressure was varied from -12.0 psi in increments of 0.2 psi to -13.4 psi to test a total of eight plenum pressures. The current pulse, implosion trajectory, K-shell output in the 2.5 keV to 5.0 keV range, and kinetic energy and total x-ray yield for each liner mass density are plotted as a function of time in Fig. 4.4, which demonstrates observable trends. As the liner mass decreases, the time to stagnation is observed to decrease as well. K-shell signals are not observed for most of the high mass shots but are present for the low mass shots. The liner kinetic energy is seen to decrease with decreasing liner mass while the total x-ray energy output is seen to increase with decreasing liner mass. The results for these shots are summarized in Table 4.1.

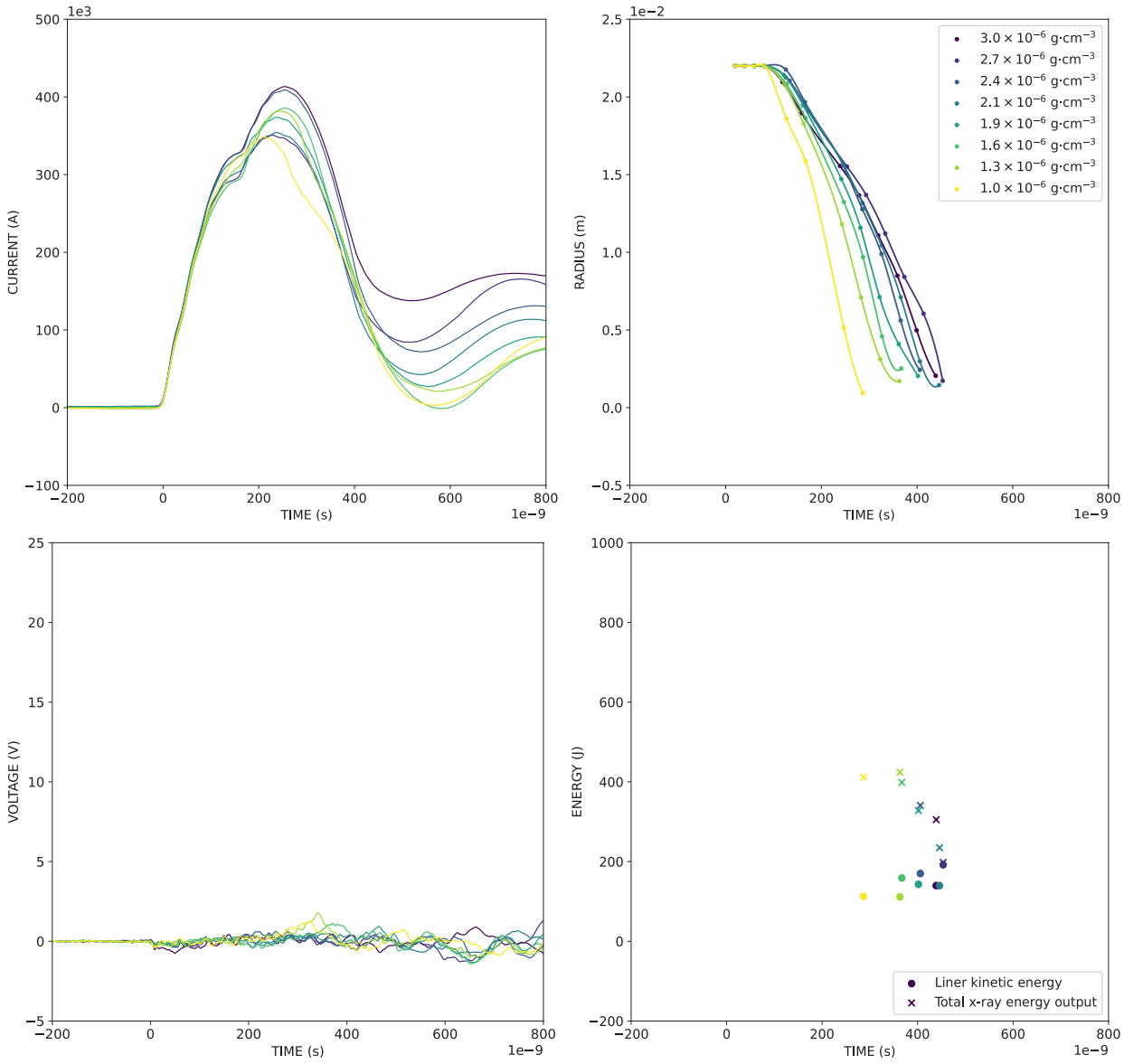

Figure 4.4: Summary of results for argon outer-shell gas-puff z-pinch experiments. The liner mass densities tested range from 3.0×10^{-6} g·cm^{-3} to 1.0×10^{-6} g·cm^{-3}. The plots on the top-left show the current pulse, the plots on the top-right show the implosion trajectory, the plots on the bottom-left show the K-shell output in the 2.5 keV to 5.0 keV range, and the plots on the bottom-right show the kinetic energy and total x-ray energy output.

Table 4.1: Summary of Results with Outer-Shell-Only Argon

Shot No.	Pressure (psig)	Mass Density ($\mathrm{g \cdot cm^{-3}}$)	Peak Current ($\pm 5 \times 10^3$A)	Stagnation Time ($\pm 20 \times 10^{-9}$ s)	Kinetic Energy (J $\pm 25\%$)	K-Shell Signal (± 0.1 V)	X-Ray Yield (J $\pm 10\%$)
2197	-12.0	3.0×10^{-6}	410×10^3	440×10^{-9}	140	0.0	300
2198	-12.2	2.7×10^{-6}	350×10^3	450×10^{-9}	190	0.0	200
2199	-12.4	2.4×10^{-6}	400×10^3	410×10^{-9}	170	0.0	340
2200	-12.6	2.1×10^{-6}	350×10^3	440×10^{-9}	140	0.0	230
2201	-12.8	1.9×10^{-6}	370×10^3	400×10^{-9}	140	0.0	330
2202	-13.0	1.6×10^{-6}	380×10^3	360×10^{-9}	160	1.1	400
2203	-13.2	1.3×10^{-6}	380×10^3	350×10^{-9}	110	1.8	420
2193	-13.4	1.0×10^{-6}	350×10^3	290×10^{-9}	110	1.2	410

We identify argon outer-shell mass densities ranging from 1.0×10^{-6} g·cm^{-3} to 1.6×10^{-6} g·cm^{-3} (or plenum pressures ranging from -13.4 psi to -13.0 psi) as better matched for implosion on MAIZE than higher mass densities. Results for the high yield argon outer-shell shots with mass densities of 1.0×10^{-6} g·cm^{-3} (shot 2193) and 1.3×10^{-6} g·cm^{-3} (shot 2203) are shown in greater detail in Fig. 4.5 (top and bottom, respectively). Note that the resulting implosions are still considerably slower than those of an ideal z-pinch which should stagnate just after peak current. Shot 2193 outputs 410 J of total x-ray energy and shot 2203 outputs 420 J of total x-ray energy. With stored energy of 5.7 kJ stored in the MAIZE capacitors, this corresponds to a wall-plug efficiency of 7.2% and 7.4%, respectively.

4.2.2 Outer-Shell-Only Deuterium Gas-Puff Z-Pinch Experiments

Outer-shell deuterium gas-puff z-pinch experiments were carried out with five separate plenum pressures of 4.0 psi, -4.0 psi, -6.0 psi, -8.0 psi, and -10.0 psi. Referring to Fig. 4.3, this relates to liner number densities ranging from 0.41×10^{18} cm^{-3} to 0.11×10^{18} cm^{-3}, respectively, or liner mass densities ranging from 2.7×10^{-6} g·cm^{-3} to 0.7×10^{-6} g·cm^{-3}, respectively. The current pulse, implosion trajectory, neutron yield as calculated on-axis and off-axis, and kinetic energy for each liner mass density are plotted as a function of time in Fig. 4.6, which demonstrates observable trends. As the liner mass decreases, the time to stagnation is observed to decrease in the expected fashion and as seen with the outer-shell-only argon shots. Neutrons are below the observable threshold for most of the liner masses tested except for a signal observed on axis for a low mass shot. The liner kinetic energy is roughly constant with decreasing liner mass.

The results for these shots are summarized in Table 4.2.

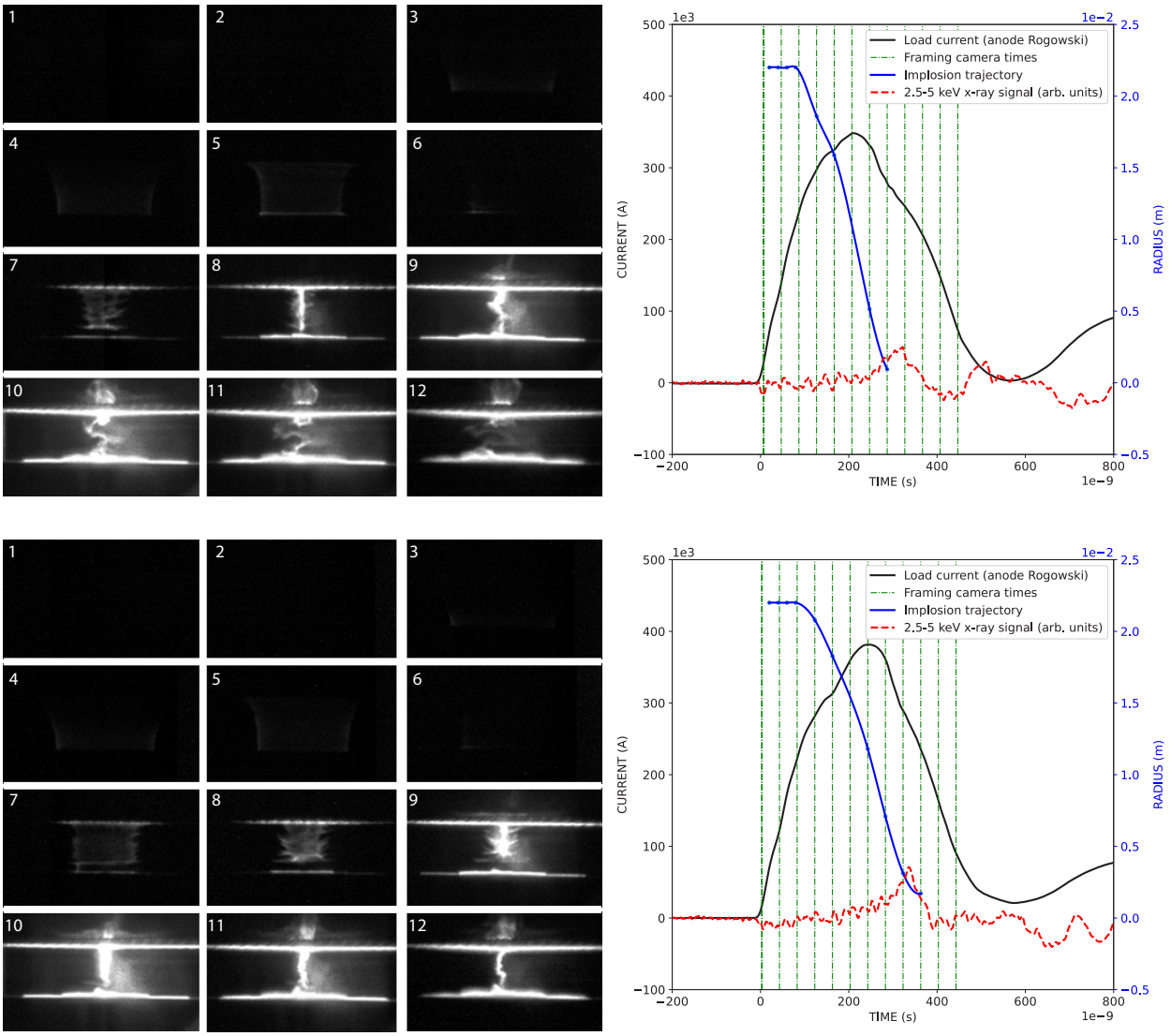

Figure 4.5: Summary of results for argon outer-shell mass density of 1.0×10^{-6} g·cm^{-3} (top) and 1.3×10^{-6} g·cm^{-3} (bottom). The sequence of images on the top and bottom left show the fast-framing camera images of the implosion. The plots on the top and bottom right show the current pulse, timing of the fast-framing camera images, implosion trajectory, and the 2.5 keV to 5 keV argon K-shell signal.

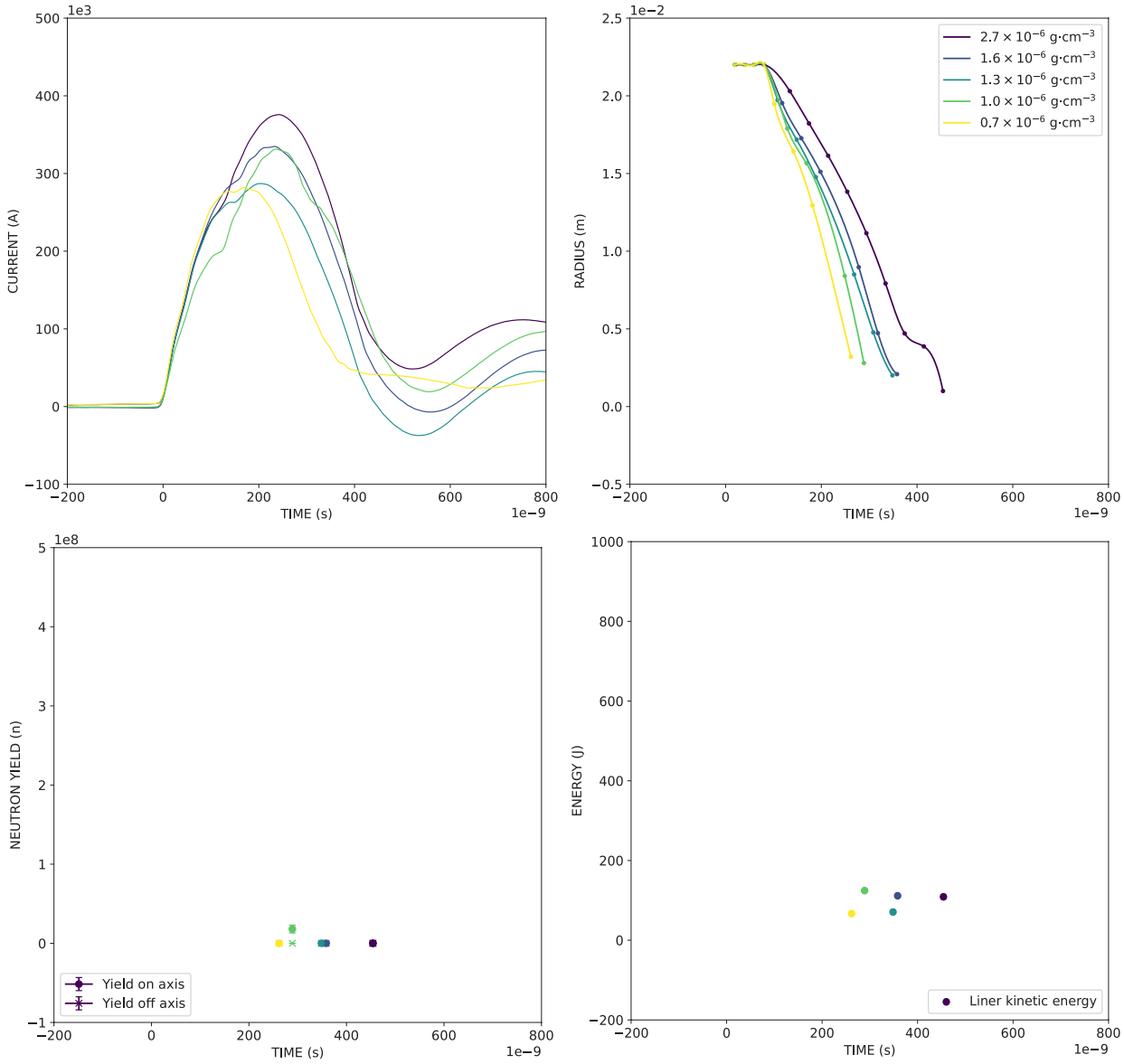

Figure 4.6: Summary of results for deuterium outer-shell gas-puff z-pinch experiments. The liner mass densities tested range from 2.7×10^{-6} g·cm^{-3} to 0.7×10^{-6} g·cm^{-3}. The plots on the top-left show the current pulse, the plots on the top-right show the implosion trajectory, the plots on the bottom-left show the neutron yield as calculated both on-axis and off-axis, and the plots on the bottom-right show the kinetic energy.

Table 4.2: Summary of Results with Outer-Shell-Only Deuterium

Shot No.	Pressure (psig)	Mass Density ($\mathrm{g \cdot cm^{-3}}$)	Peak Current ($\pm 5 \times 10^3$A)	Stagnation Time ($\pm 20 \times 10^{-9}$ s)	Kinetic Energy (J $\pm 25\%$)	Neutron Yield (On-Axis)	Neutron Yield (Off-Axis)
2303	4.0	2.7×10^{-6}	370×10^3	370×10^{-9}	110	0.0	0.0
2304	-4.0	1.6×10^{-6}	330×10^3	360×10^{-9}	110	0.0	0.0
2306	-6.0	1.3×10^{-6}	290×10^3	350×10^{-9}	70	0.0	0.0
2305	-8.0	1.0×10^{-6}	330×10^3	290×10^{-9}	120	1.8×10^7	0.0
2307	-10.0	0.7×10^{-6}	280×10^3	260×10^{-9}	70	0.0	0.0

We identify deuterium outer-shell mass density of 1.0×10^{-6} g·cm^{-3} (or plenum pressure of -8.0 psi) as better matched for implosion on MAIZE than higher mass densities. Note that the resulting implosion of the better matched liner is still considerably slower than that of an ideal z-pinch which should stagnate just after peak current. Results for the high-yield deuterium shot with mass density of 1.0×10^{-6} g·cm^{-3} (shot 2305) is contrasted with the low-yield deuterium shot with mass density of 1.6×10^{-6} g·cm^{-3} (shot 2304) in greater detail in Fig. 4.7 (top and bottom, respectively). Shot 2305 outputs 1.8×10^{7} neutrons as measured on-axis and shot 2304 outputs neutrons below the detector threshold as measured on-axis. Both shots output neutrons below the detector threshold as measured off-axis.

4.3 Inner-Shell Gas-Puff Z-Pinch Experiments

After understanding the dynamics of the gas flow of the inner-shell target as a function of the timing and pressure parameters of the fast-valve and nozzles, desired inner-shell densities can be formed for pinching. This section describes the pinch dynamics and energetics of inner-shell z-pinches as these densities are varied for argon, in Sec. 4.3.1, and deuterium, in Sec. 4.3.2. We select a constant 500 μs for argon and a constant 300 μs for deuterium as the time after the fast-valve of the outer-shell fires to discharge MAIZE, which is charged to ± 60 KV for each shot. We then vary the plenum pressure (i.e., the density distributions) for each gas to study how each implosion performs.

4.3.1 Inner-Shell-Only Argon Gas-Puff Z-Pinch Experiments

Inner-shell argon gas-puff z-pinch experiments were carried out with plenum pressures ranging from 0.0 psi to -13.0 psi. Referring to Fig. 4.3, this relates to liner number densities ranging from 0.28×10^{18} cm^{-3} to 0.085×10^{18} cm^{-3}, respectively, or liner mass densities ranging from 19×10^{-6} g·cm^{-3} to 5.6×10^{-6} g·cm^{-3}, respectively. In particular, plenum pressure was varied from 0.0 psi in increments of 1.0 psi to -13.0 psi to test a total of 13 plenum pressures. The current pulse, implosion trajectory, K-shell output in the 2.5 keV to 5.0 keV range, and kinetic energy and total x-ray yield for each liner mass density are plotted as a function of time in Fig. 4.8, which demonstrates clearly observable trends. As the liner mass decreases, the time to stagnation is observed to decrease, as expected. Highest K-shell signals are observed for the low-intermediate masses while highest total x-ray yield is observed for intermediate-high liner masses. Unlike the outer-shell-only argon shots, the liner kinetic energy here is correlated to the x-ray yield. The results for these shots are summarized in Table 4.3.

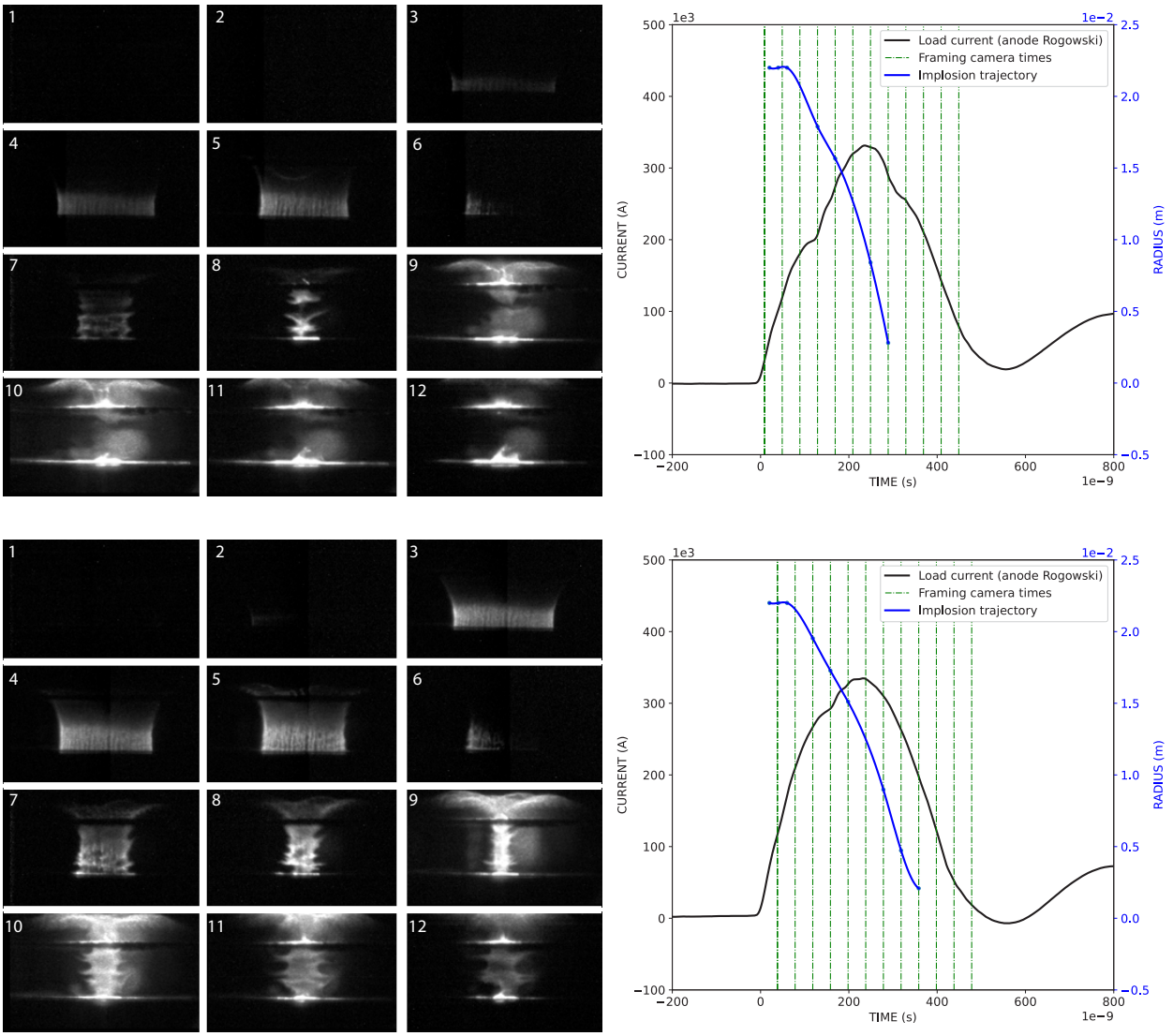

Figure 4.7: Summary of results for deuterium outer-shell mass density of 1.0×10^{-6} g·cm^{-3} (top) and 1.6×10^{-6} g·cm^{-3} (bottom). The sequence of images on the top and bottom left show the fast-framing camera images of the implosion. The plots on the top and bottom right show the current pulse, timing of the fast-framing camera images, and the implosion trajectory.

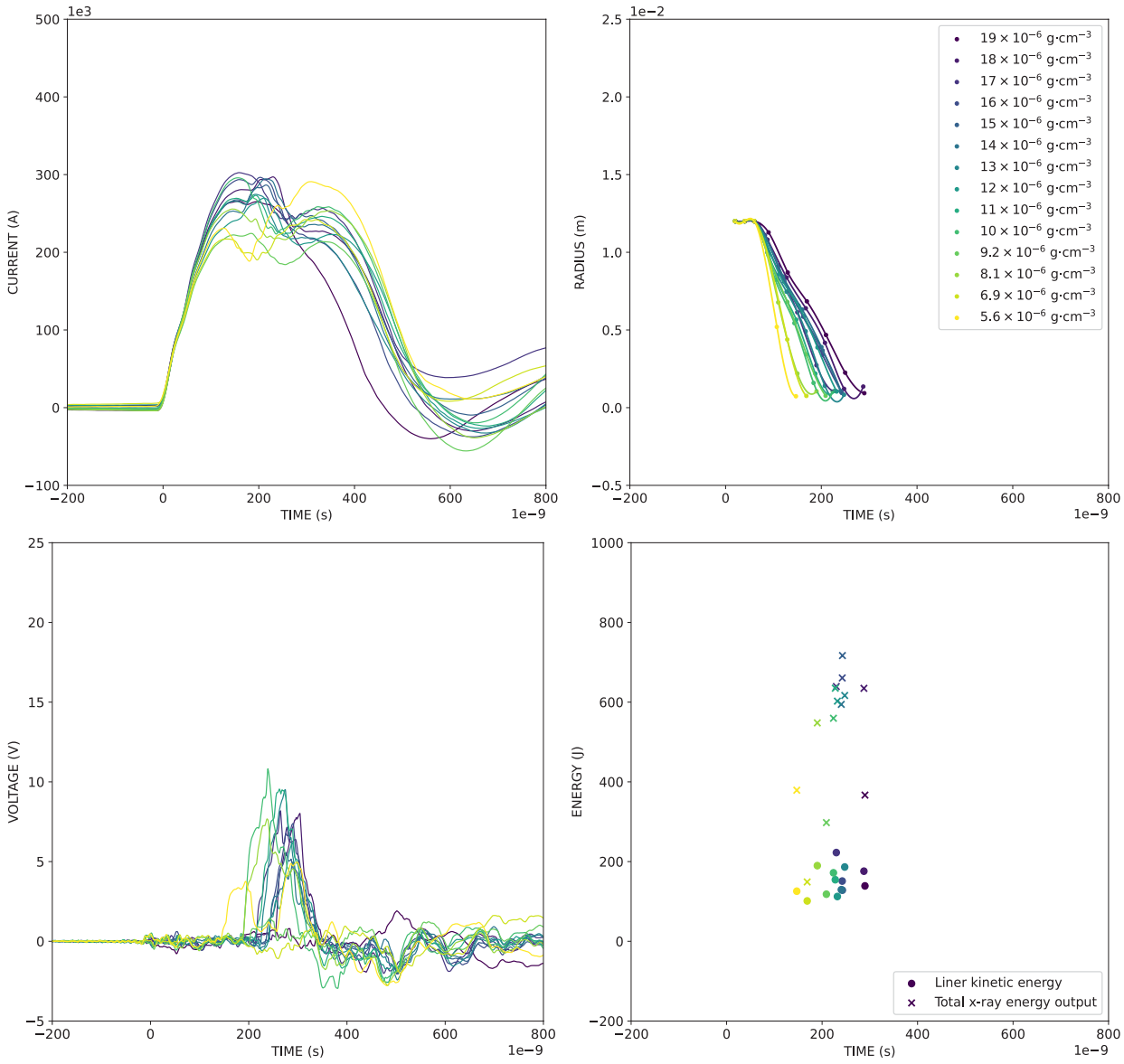

Figure 4.8: Summary of results for argon inner-shell gas-puff z-pinch experiments. The liner mass densities tested range from 19×10^{-6} g·cm^{-3} to 5.6×10^{-6} g·cm^{-3}. The plots on the top-left show the current pulse, the plots on the top-right show the implosion trajectory, the plots on the bottom-left show the K-shell output, and the plots on the bottom-right show the kinetic energy and total x-ray energy output.

Table 4.3: Summary of Results with Inner-Shell-Only Argon

Shot No.	Pressure (psig)	Mass Density ($\mathrm{g \cdot cm^{-3}}$)	Peak Current ($\pm 5 \times 10^3$A)	Stagnation Time ($\pm 20 \times 10^{-9}$ s)	Kinetic Energy (J $\pm 25\%$)	K-Shell Signal (± 0.1 V)	X-Ray Yield (J $\pm 10\%$)
2208	0.0	19×10^{-6}	270×10^3	290×10^{-9}	140	1.9	370
2210	-1.0	18×10^{-6}	300×10^3	250×10^{-9}	180	8.0	630
2212	-2.0	17×10^{-6}	300×10^3	220×10^{-9}	220	8.2	640
2214	-3.0	16×10^{-6}	300×10^3	240×10^{-9}	150	7.4	660
2216	-4.0	15×10^{-6}	290×10^3	240×10^{-9}	130	5.6	720
2207	-5.0	14×10^{-6}	290×10^3	210×10^{-9}	130	5.0	600
2219	-6.0	13×10^{-6}	270×10^3	230×10^{-9}	190	9.5	620
2221	-7.0	12×10^{-6}	270×10^3	220×10^{-9}	110	6.1	600
2223	-8.0	11×10^{-6}	270×10^3	190×10^{-9}	150	9.6	630
2225	-9.0	10×10^{-6}	300×10^3	190×10^{-9}	170	10.8	560
2206	-10.0	9.2×10^{-6}	230×10^3	210×10^{-9}	120	1.4	300
2228	-11.0	8.1×10^{-6}	260×10^3	180×10^{-9}	190	7.7	550
2205	-12.0	6.9×10^{-6}	220×10^3	170×10^{-9}	100	2.8	150
2231	-13.0	5.6×10^{-6}	230×10^3	150×10^{-9}	130	5.0	380

We identify separate masses as better matched for implosion on MAIZE, when considering either total x-ray energy output or K-shell signal amplitudes. While the total x-ray energy output was highest for intermediate-higher liner masses, the K-shell signal was highest for lower-intermediate liner masses. Results for a shot with a high K-shell signature– with mass density of 11×10^{-6} g·cm^{-3} (shot 2223)– is contrasted with a shot with a high total x-ray yield– with mass density of 15×10^{-6} g·cm^{-3} (shot 2216)– in Fig. 4.9 (top and bottom, respectively). Shot 2223 outputs 620 J of total x-ray energy and shot 2216 outputs 720 J of total x-ray energy. With stored energy of 5.7 kJ stored in the MAIZE capacitors, this corresponds to a wall-plug efficiency of 11.0% and 12.6%, respectively.

4.3.2 Inner-Shell-Only Deuterium Gas-Puff Z-Pinch Experiments

Inner-shell deuterium gas-puff z-pinch experiments were carried out with plenum pressures ranging from 0.0 psi to -10.0 psi. Referring to Fig. 4.3, this relates to liner number densities ranging from 1.981×10^{18} cm^{-3} to 0.775×10^{18} cm^{-3}, respectively, or liner mass densities ranging from 13×10^{-6} g·cm^{-3} to 4.8×10^{-6} g·cm^{-3}, respectively. In particular, plenum pressure was varied from 0.0 psi in increments of 2.0 psi to -10.0 psi to test a total of 6 plenum pressures. The current pulse, implosion trajectory, neutron yield on-axis and off-axis, and kinetic energy for each liner mass density are plotted as a function of time in Fig. 4.10, which demonstrates observable trends. Like with the other experiments, we see the time to stagnation of the pinch decreasing with decreasing liner mass. We also see increasing neutron yields with lower liner masses, with higher yields measured on-axis as opposed to off-axis. Like the deuterium outer-shell-only experiment, the kinetic energy coupled to the liner is fairly constant for all the liner masses testes. The results for these shots are summarized in Table 4.4.

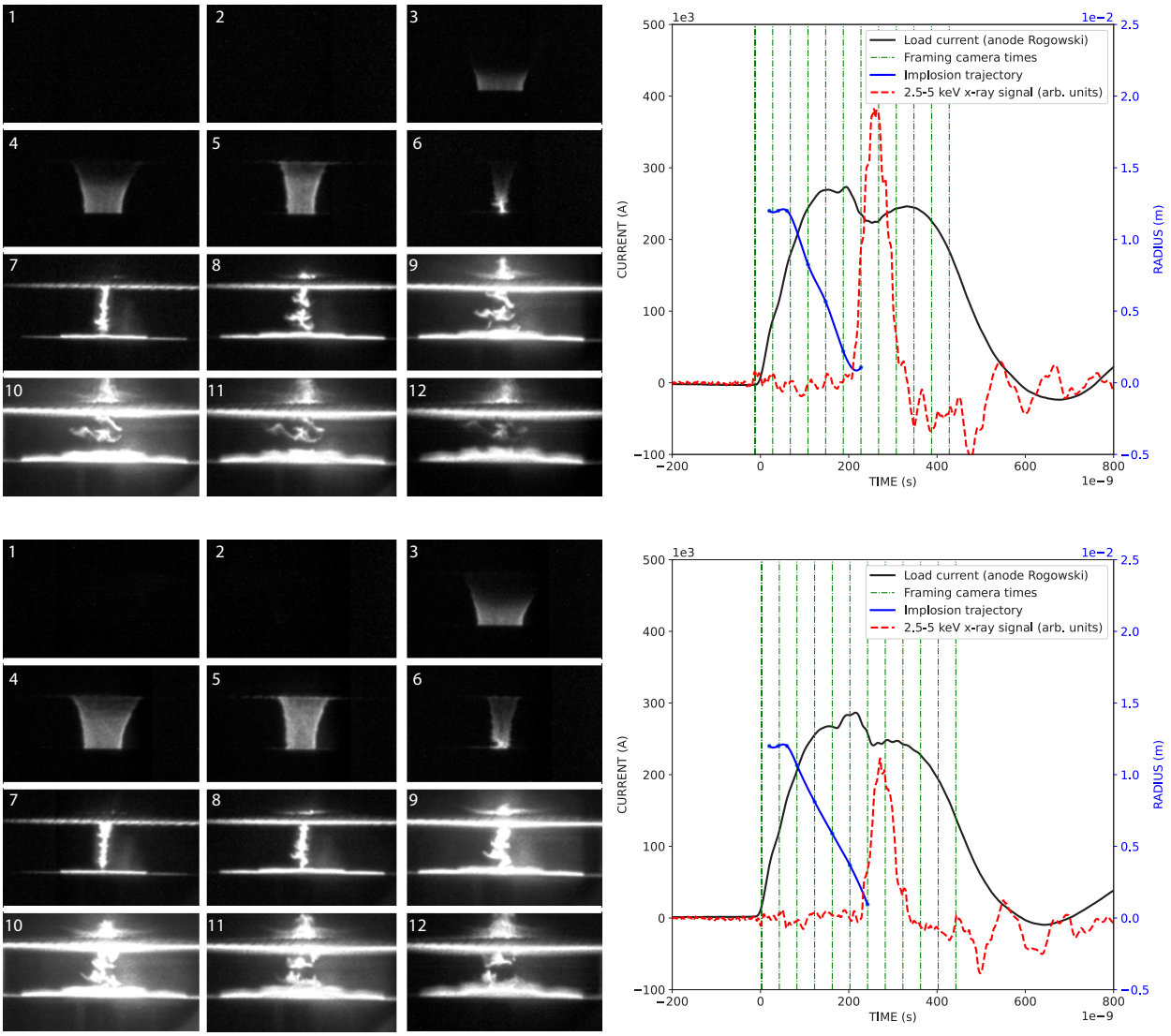

Figure 4.9: Summary of results for argon inner-shell mass density of 11×10^{-6} g·cm^{-3} (top) and 15×10^{-6} g·cm^{-3} (bottom). The sequence of images on the top and bottom left show the fast-framing camera images of the implosion. The plots on the top and bottom right show the current pulse, timing of the fast-framing camera images, implosion trajectory, and the 2.5 keV to 5.0 keV argon k-shell signal.

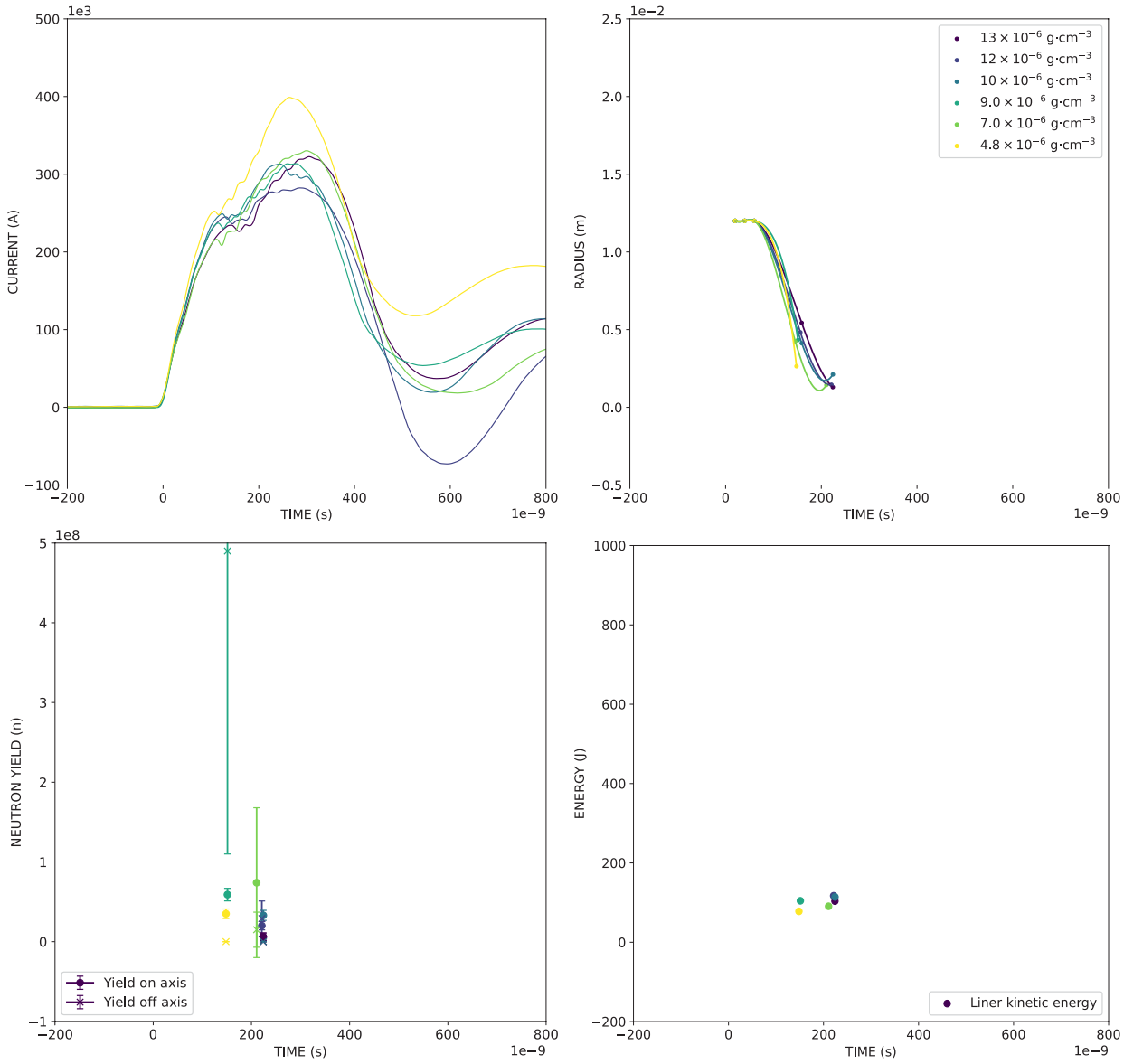

Figure 4.10: Summary of results for deuterium inner-shell gas-puff z-pinch experiments. The liner mass densities tested range from 13×10^{-6} g·cm^{-3} to 4.8×10^{-6} g·cm^{-3}. The plots on the top-left show the current pulse, the plots on the top-right show the implosion trajectory, the plots on the bottom-left show the neutron yield as calculated both on-axis and off-axis, and the plots on the bottom-right show the kinetic energy.

Table 4.4: Summary of Results with Inner-Shell-Only Deuterium

Shot No.	Pressure (psig)	Mass Density $(\mathrm{g} \cdot \mathrm{cm}^{-3})$	Peak Current $(\pm 5 \times 10^3 \mathrm{A})$	Stagnation Time $(\pm 20 \times 10^{-9}$ s)	Kinetic Energy (J $\pm 25\%$)	Neutron Yield (On-Axis)	Neutron Yield (Off-Axis)
2297	0.0	13×10^{-6}	310×10^3	220×10^{-9}	100	4.8×10^6	0.0
2298	-2.0	12×10^{-6}	280×10^3	220×10^{-9}	120	2.0×10^7	2.9×10^7
2299	-4.0	10×10^{-6}	310×10^3	220×10^{-9}	120	3.3×10^7	0.0
2300	-6.0	9.0×10^{-6}	310×10^3	150×10^{-9}	100	5.9×10^7	4.9×10^8
2301	-8.0	7.0×10^{-6}	330×10^3	210×10^{-9}	90	7.4×10^7	1.5×10^7
2302	-10.0	4.8×10^{-6}	400×10^3	150×10^{-9}	80	3.5×10^7	0.0

We identify deuterium inner-shell mass density of 9.0×10^{-6} g·cm^{-3} (or plenum pressures of -6.0 psi) as better matched for implosion on MAIZE than lower or higher mass densities. Note that the resulting implosion of the better matched liner is considerably faster than an ideal pinch which should occur just after peak current. Results for the high yield deuterium shot with mass density of 9.0×10^{-6} g·cm^{-3} (shot 2300) are contrasted with a low yield deuterium shot with mass density of 13×10^{-6} g·cm^{-3} (shot 2297) in greater detail in Fig. 4.11 (top and bottom, respectively). Shot 2300 outputs 5.9×10^{7} neutrons as measured on-axis and 4.9×10^{8} neutrons as measured off-axis. Shot 2297 outputs 6.1×10^{6} neutrons as measured on-axis and neutrons below the detector threshold as measured off-axis.

4.4 Argon Outer-Shell on Deuterium Inner-Shell Z-Pinch Experiments

This section describes the pinch dynamics of argon outer-shell on deuterium inner-shell z-pinches to demonstrate its stabilizing effect. We select an outer-shell argon pressure of -13.5 and an inner-shell deuterium pressure of 10.0 psi. The outer shell (argon) was fired 900 μs prior to discharging MAIZE, while the inner shell (deuterium) was fired 600 μs prior to discharging MAIZE. The MAIZE capacitors were charged to $\pm$60 kV. Note that these experiments were carried out prior to several upgrades and improvements in the shot sequence and were not well informed or diagnosed, hence the variation in setup parameters from the experiments presented above. Also, it was noted that the nozzles and fast-valve did not behave such that the density distribution of the two shells firing together was a linear combination of each of the shells firing individually. As such, Fig. 4.3 cannot be used and the density distribution in the target is not known. Results for the shell-on-shell argon-on-deuterium shot (shot 1948) is contrasted with the outer-shell argon shot (shot 1928) in Fig. 4.12 (top and bottom, respectively). The argon-on-deuterium shot produced no neutrons as measured on-axis and off-axis.

4.5 Discussion

4.5.1 Inductive Dip and Post-Dip Current Amplification

The current traces of both argon and deuterium inner-shell-only implosions experience a dramatic inductive dip, whereby the current is rapidly pulled down. The inductive dips are experienced in shots with lower masses, for both gases, when the time to stagnation was below 250 ns. These can be explained by a rapidly increasing inductance as the pinch rapidly accelerates radially in-

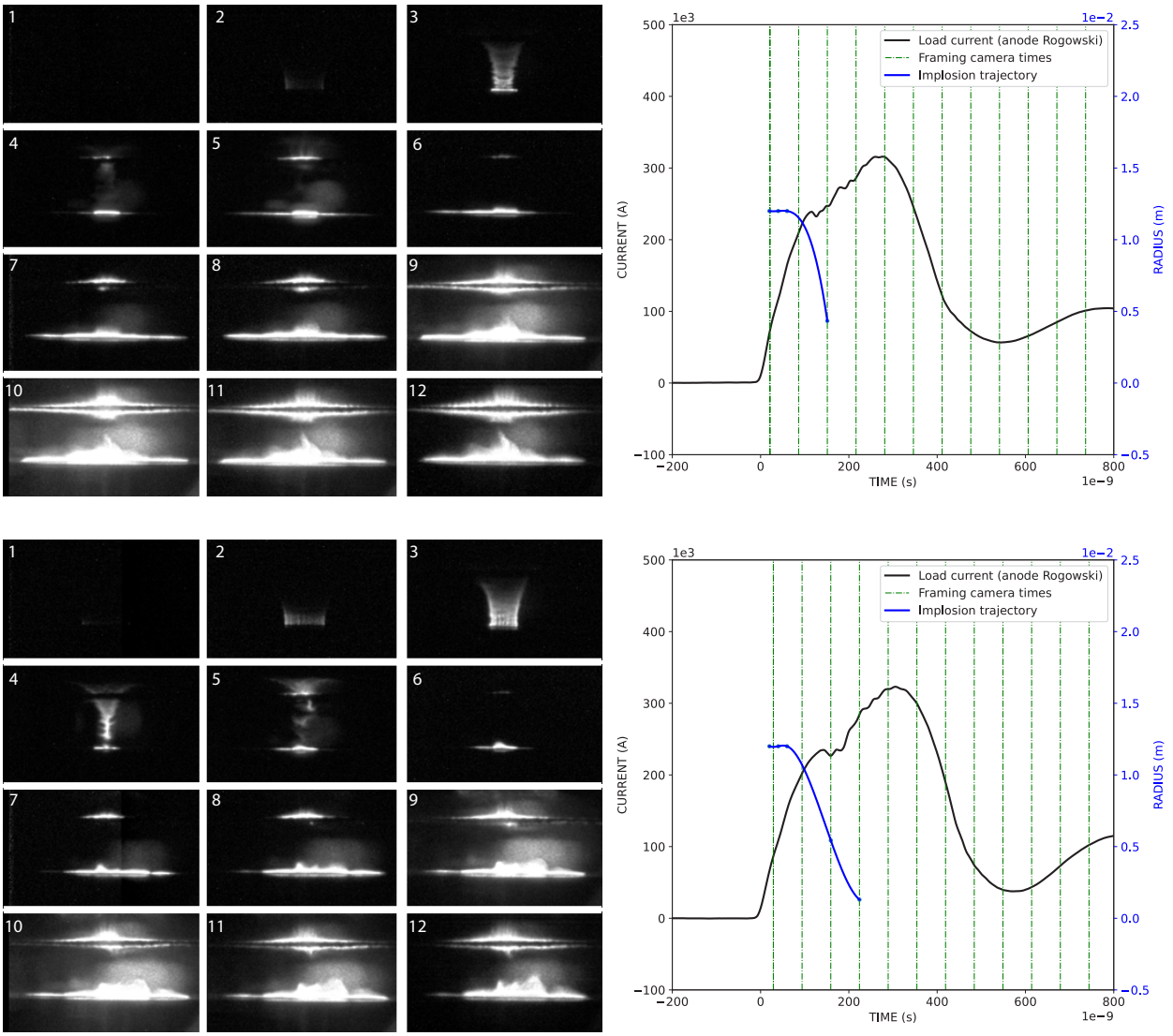

Figure 4.11: Summary of results for deuterium inner-shell mass density of 9×10^{-6} g·cm^{-3} (top) and 13×10^{-6} g·cm^{-3} (bottom). The sequence of images on the top and bottom left show the fast-framing camera images of the implosion. The plots on the top and bottom right show the current pulse, timing of the fast-framing camera images, and the implosion trajectory.

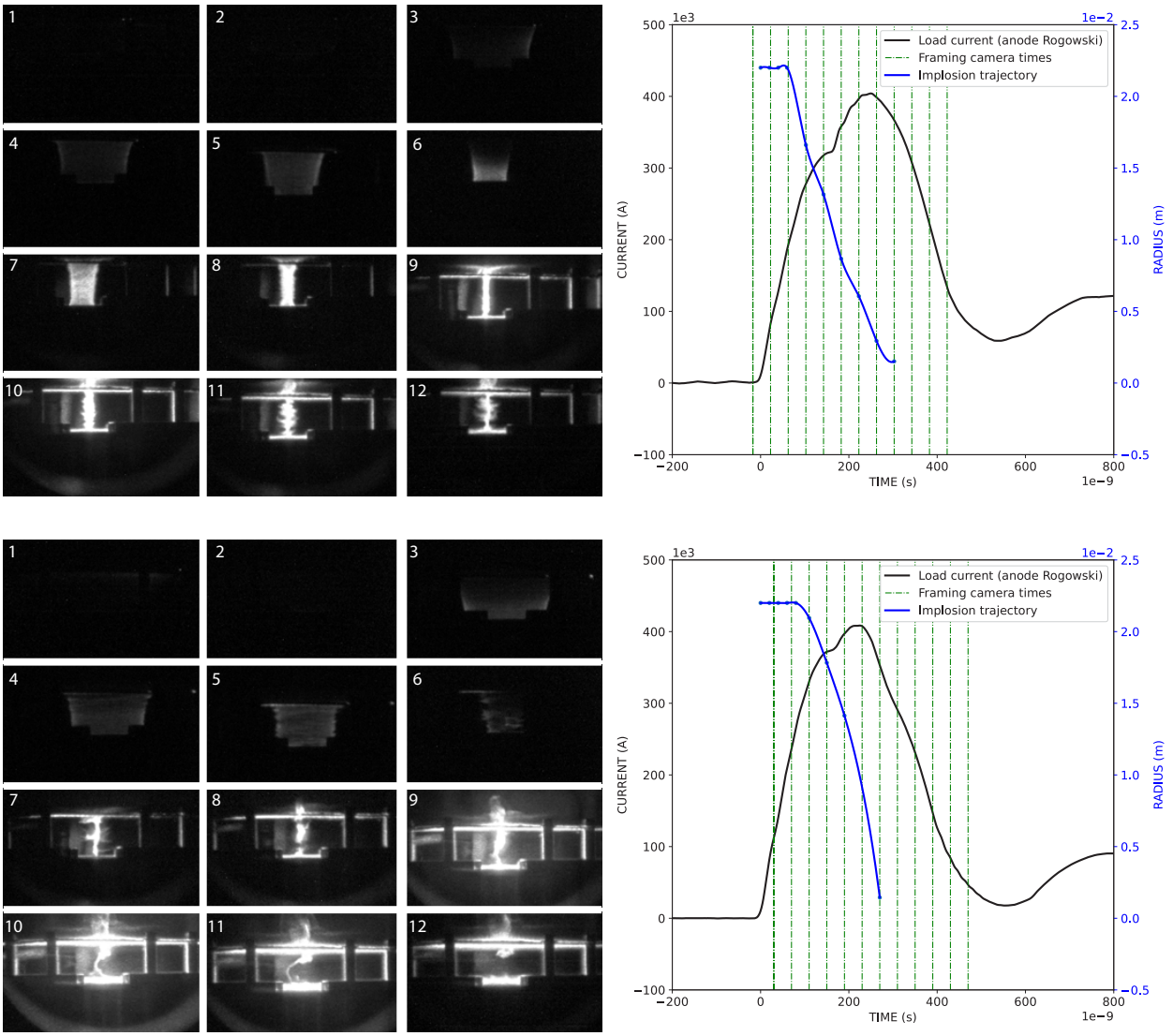

Figure 4.12: Summary of results for argon-on-deuterium shell-on-shell shot (top) and argon outer-shell shot (bottom). The sequence of images on the top and bottom left show the fast-framing camera images of the implosion. The plots on the top and bottom right show the current pulse, timing of the fast-framing camera images, and the implosion trajectory.

wards. MAIZE, a low impedance driver, is rather susceptible to the implosion dynamics, and so the inductive dips are very pronounced in the current traces.

Following the inductive dip, these same current traces experience current recovery and amplification, whereby the current rises. The amplitude of this second peak is higher for lower implosion masses. Current amplification occurs after the pinch stagnates, bounces off its axis of symmetry, and explodes. This rapidly reduces the inductance of the target, and as the capacitors continue to discharge, the magnetic flux is trapped and the current is magnified, in a fashion opposite to that of the inductive dip. The lower masses experience greater current amplification due to the fact that they stagnate and bounce before the capacitors are entirely discharged. This is confirmed by the systematic increase in the amplitude of the second peak as the implosion mass is lowered and the time to stagnation is decreased. Some inner-shell shots with higher masses (high enough for stagnation to occur after the natural rise time of MAIZE) have a slight inductive dip on the falling edge of the current pulse. These dips are not prominent because the change in inductance is slower than with fast implosions. Additionally, these current traces do not experience any perceivable amplification late in time. The contrast in current amplification as experienced by the low-mass (shot 2231) and high-mass (shot 2208) liners in the argon inner-shell-only experiments is shown in Fig. 4.13. Simple zero dimensional modeling of the explosion phase of the z-pinch following stagnation further confirms this phenomenon, as shown in Fig. 4.14. Note that outer-shell-only experiments with argon and deuterium did not demonstrate the current amplification behavior because low stagnation times could not be accessed.

4.5.2 Variation in Implosion Trajectories

Each of the experimental configurations presented in Sec. 4.2 and in Sec. 4.3 demonstrates an imperfect relationship between liner mass and time to stagnation. While the general trend is respected, where lower liner masses implode faster than heavier liner masses, there are notable exceptions between individual cases. We hypothesize that this can be attributed to complex gas flow dynamics, not only in the target region downstream of the nozzles, but also in the gas manifold and the plenum. Note that there is approximately 100 feet of quarter-inch diameter aluminum tubing between the gas manifold, where the pressure gauge and vacuum pump are located, and the plenum of the gas-puff hardware, where the gas that forms the target is stored. Such long lengths of small-diameter tubing is highly resistive to gas flow. While we confirmed that the pressure at the plenum is equivalent to the pressure at the manifold, it is likely that the vacuuming of the lines is imperfect and pressure conditions during shots vary.

A noteworthy contrast was observed in the experiments shown above depending on the material of the gas lines used. Initial experiments were carried out with nylon tubing, in which there was

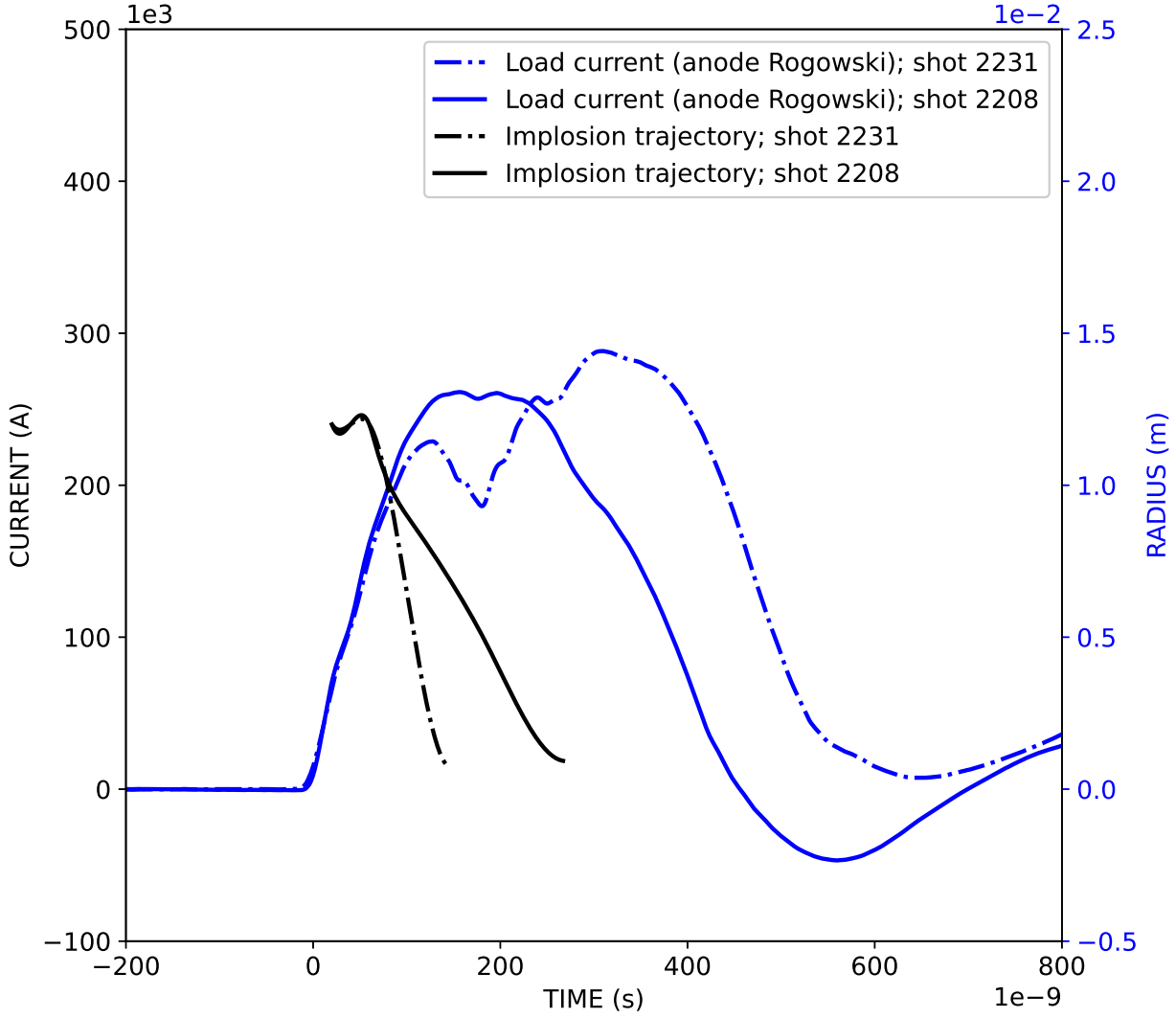

Figure 4.13: Current pulse and implosion trajectory of two argon inner-shell-only implosions with low mass (shot 2231) and high mass (shot 2208) liners.

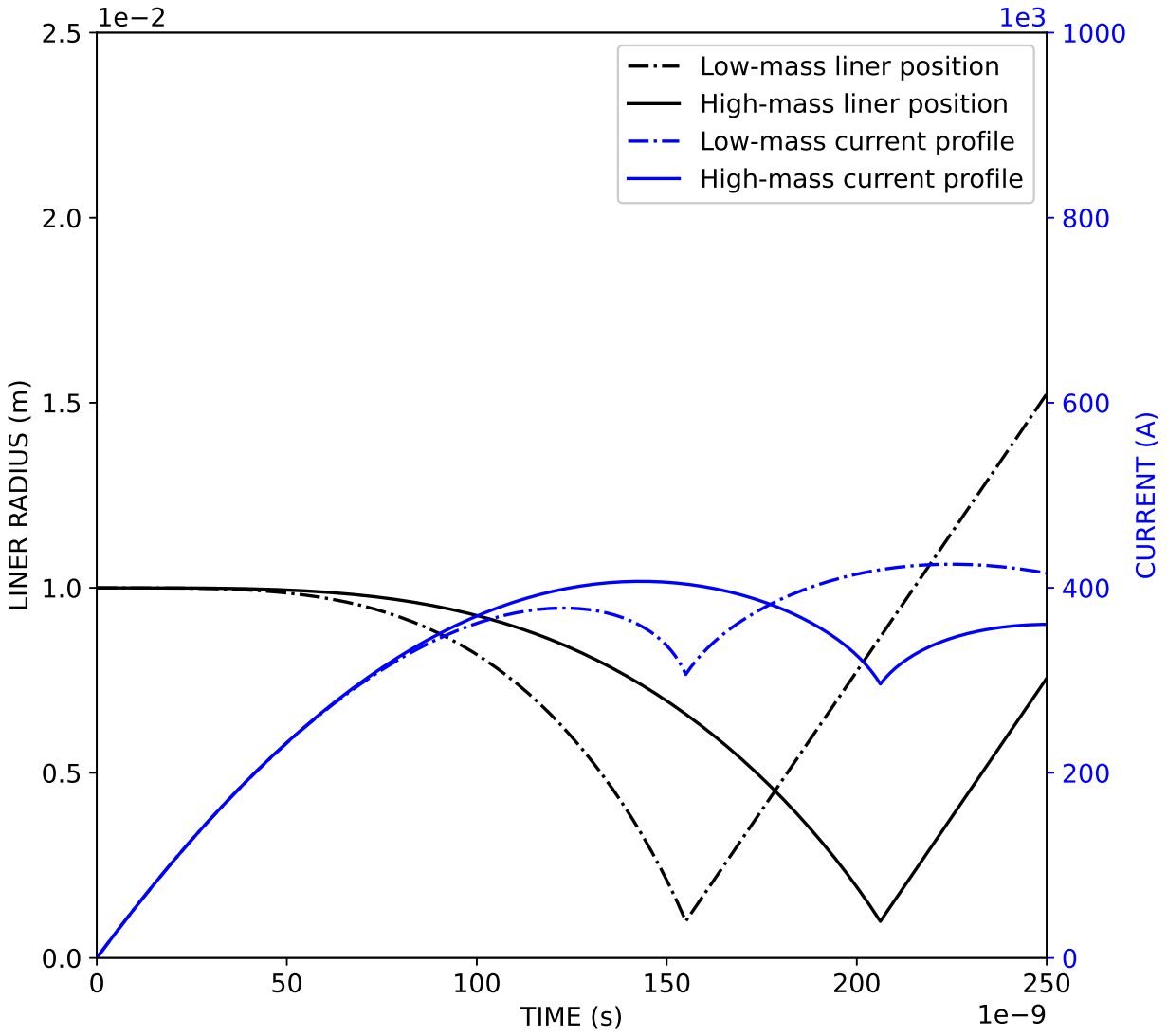

Figure 4.14: Voltage-driven model for the implosion dynamics of the inner-shell given MAIZE-like driver parameters. Here, the liner experiences a constant-velocity explosive phase after stagnation, where it bounces radially outwards. As seen, liners stagnating early experience a larger post-dip current amplification than liners stagnating later in time.

simply no correlation between the liner mass and the time to stagnation of the z-pinch. The implosion time was ostensibly random with respect to the liner mass; in fact similar pressures would stagnate at different times. The contrast in the implosion time versus pressure when using the aluminum gas lines and the nylon gas lines are shown in Fig. 4.15. Upgrading the nylon tubing to aluminum improved the reproducibility of the pinch and led to the observed trends presented above. Further upgrades can be implemented: install a turbo pump backed by a roughing pump to vacuum out the gas lines prior to shots; pump out the gas lines for longer times between shots; and install a residual gas analyzer to verify gas purity prior to shots. This should further improve the linear relationship of time to stagnation versus pressure with the aluminum lines.

4.5.3 Instability Formation

An imploding plasma column such as in a z-pinch is afflicted by the magneto-Rayleigh-Taylor (MRT) instability. The MRT instability growth rate is proportional to the inward acceleration of the plasma [53, 54, 55]. The gas-puff z-pinch outer-shell-only experiments experience a larger inward acceleration due to their initialization at larger radius and, as such, are expected to suffer from larger amplitude MRT instability than inner-shell-only experiments. A sequence of images showing the outer-shell implosions with argon and deuterium are contrasted with those showing the inner-shell implosions in Fig. 4.16, where this prediction is confirmed.

Further, as the plasma radially accelerates and eventually stagnates on axis, a radial equilibrium is achieved, whereby the internal plasma pressure balances the external magnetic driving pressure. This equilibrium is unstable to magnetohydrodynamic instabilities— the sausage and kink instabilities, in particular [56]. The argon gas-puff implosions are dominated by the kink mode late in time as the plasma begins to dissipate (see top-left and bottom-left of Fig. 4.16). The cause for this is unclear and we hypothesize the seeding of the kink modes by the particular implosion trajectories of these liners, such as a generally constant velocity implosion.

Lastly, we note the formation of filamentary structures, parallel to the direction of the axial current flow, unique to the deuterium pinches (see top-right and bottom-right of Fig. 4.16). We hypothesize this to the electrothermal instability (ETI), which has been studied as a mechanism for filament formation in gas-puff z-pinches [57, 58]. ETI is seeded by a temperature dependent resistivity in the plasma. Increasing resistivity with increasing temperature leads to formation of striations perpendicular to the direction of current flow, while decreasing resistivity with increasing temperature leads to formation of filaments parallel to the direction of current flow. The filamentary structures in the deuterium pinches suggest just such an inverse relationship between resistivity and temperature. Detailed and systematic studies of these instabilities formation and mitigation can and should be further explored with the gas-puff z-pinch platform.

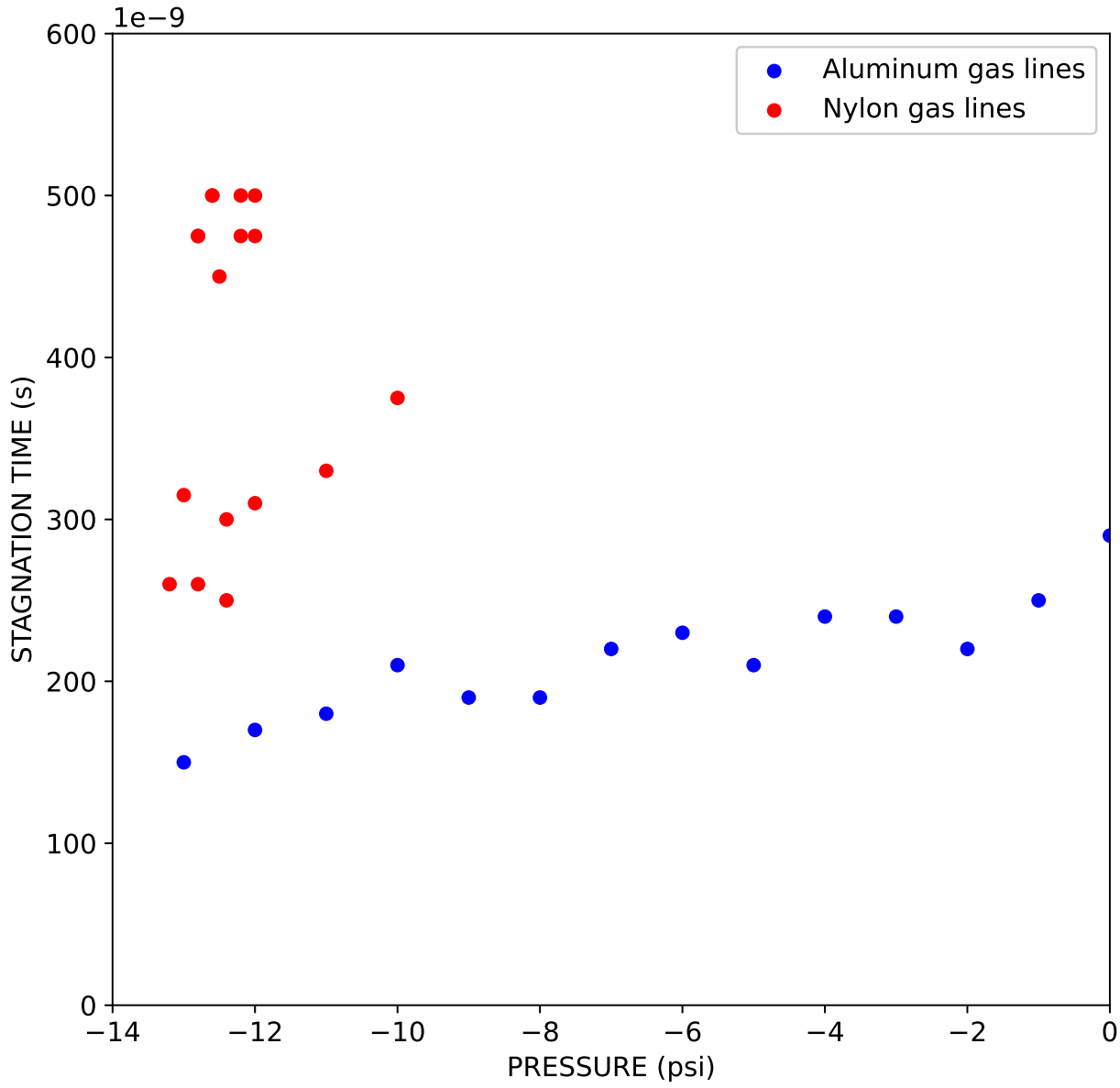

Figure 4.15: Time to stagnation of the z-pinch versus plenum pressure with aluminum and nylon gas lines. The lack of a clear trend in the plot for the nylon gas lines is indicative of their poor performance in the setup.

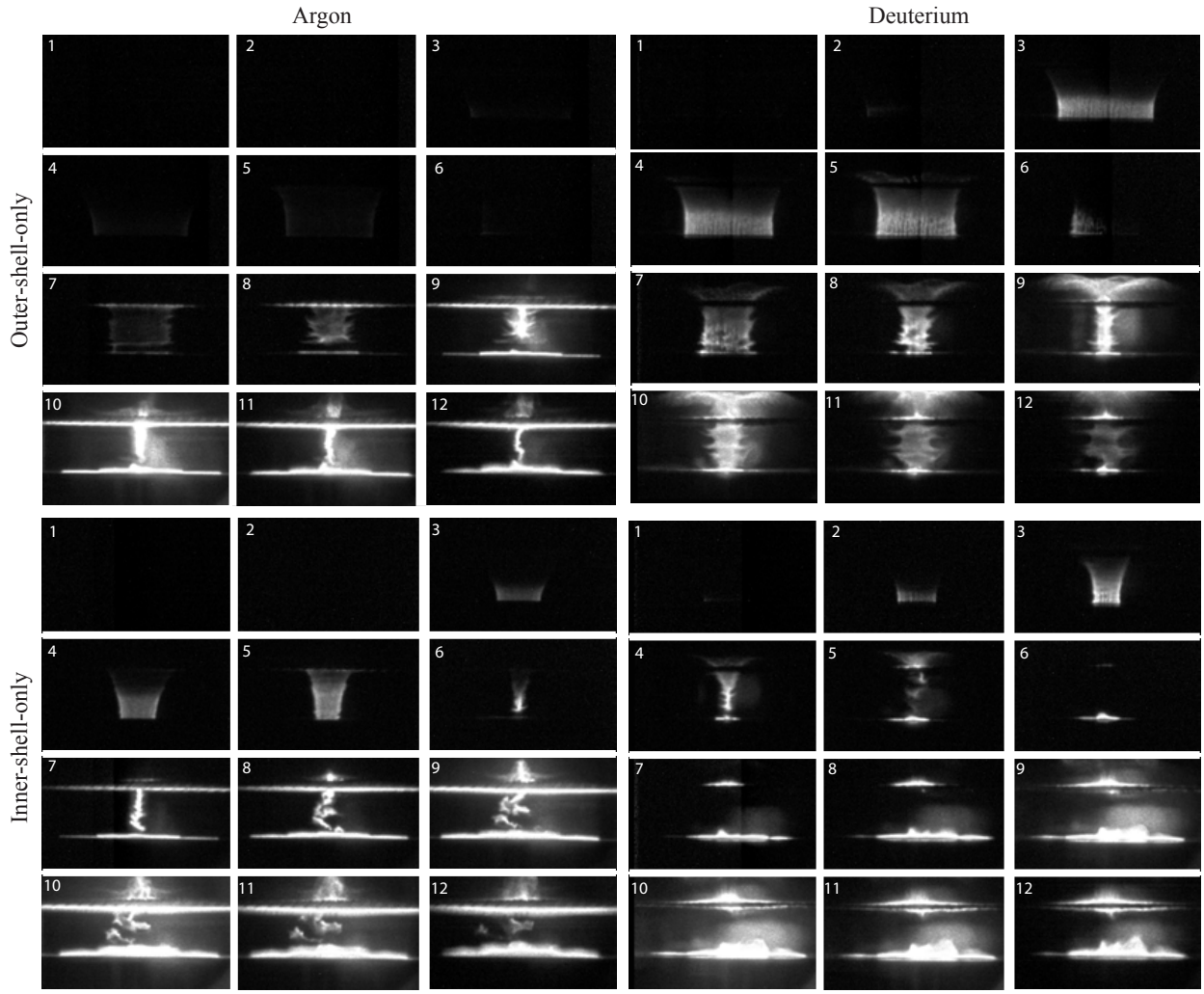

Figure 4.16: Fast framing camera images of the implosion trajectories of argon outer-shell-only (top-left), deuterium outer-shell-only (top-right), argon inner-shell-only (bottom-left), and deuterium inner-shell-only (bottom-right). The various characteristic instabilities unique to each implosion are showcased here.

4.5.4 Energy Partitioning

Consider the energetics of a gas-puff z-pinch. Electrical energy is stored in the capacitors of the pulsed-power driver. It is converted to magnetic energy during discharge as the electrical current generates magnetic fields. The Lorentz force imparts the magnetic energy to the liner in the form of kinetic energy, whereby the liner accelerates and implodes. Upon stagnation, the kinetic energy is converted to thermal energy in the plasma and output as radiation. This outline belies the complexities in each of these energy transitions. For instance, the argon experiments from above consistently confirm higher x-ray energy output than kinetic energy stored in the imploding liner. Hypotheses addressing this discrepancy involve considerations of viscous heating of ions during the implosion [59], as well as 3D effects in the plasma such as radial velocity gradients [60] and turbulence [61].

Moreover, we observe an anti-correlation between the kinetic energy and x-ray yield with the argon outer-shell experiments. Lower liner masses had lower kinetic energy and yet resulted in higher x-ray yields than higher liner masses with higher kinetic energy. This further complicates the hypothesis by suggesting that each of the postulated thermalizing mechanisms is unique to the pinch dynamics, and possibly to the pulsed-power driver. Note that the x-ray yield of the inner-shell was correlated to the kinetic energy. Additional diagnostics tools (e.g., laser Thomson scattering) can provide greater clarity on the subject of energy partitioning, particularly during the implosion and stagnation phases of the pinch.

4.5.5 X-Ray Yield Efficiency

Argon experiments produced a total x-ray output of up to 410 J for the outer-shell and 720 J for the inner-shell. For a stored energy of 5.7 kJ, these output energies correspond to wall-plug efficiencies of 7.2% and 12.6%, respectively. These are highly efficient x-ray sources, which can be employed for a wide range of scientific and engineering applications including radiation effects testing, material opacity measurements, diagnostic development, and dynamic hohlraum studies. The inner-shell is a uniformly more efficient x-ray source than the outer-shell, and each is most efficient (according to bolometer measurements) when the stagnation is timed to when the current is at approximately 90% of its peak amplitude on its falling edge. This is consistent with Ryutov's theoretical estimates for an ideal gas-puff z-pinch as discussed in Chapter 2.

The inner-shell is also a more prolific source of k-shell radiation than the outer-shell. However, there is a discrepancy between the highest total x-ray yield shots and the highest k-shell yield shots. The highest k-shell yields were experienced by liner masses that were lower and imploded faster than those of the highest total x-ray yield shots (see Fig. 4.17). This adds further confusion to the energy partitioning question: not only is the kinetic to thermal energy conversion a result of com-

plex higher dimensional physics, but also the thermal to x-ray energy conversion is related to these phenomena. X-ray spectroscopy can be fielded in addition to Thomson scattering to identify the mechanisms that link kinetic to thermal to x-ray energy conversions, for different current profiles and liner masses.

4.5.6 Neutron Yield Efficiency

Deuterium experiments produced a total neutron output of $\sim 10^7$ neutrons for the outer-shell and of $\sim 10^8$ neutrons for the inner-shell. The inner-shell is a uniformly more efficient neutron source than the outer-shell. It is hypothesized and observed that neutron production from a 1-MA class pulsed-power device is primarily beam-target, as opposed to thermonuclear, in origin. Beam-target neutrons are characterized by an anisotropy in their output: they emit more neutrons parallel to the axis of the pinch than perpendicular. Thermonuclear neutron yields typically have an isotropic profile. We fielded neutron bubble detectors both on-axis and off-axis. With the outer-shell, a neutron signal was only observed on-axis. With the inner-shell, the on-axis neutron signal was generally higher than the off-axis signal. However, the highest yield was calculated off-axis. We hypothesize this is largely due to a high signal floor for the bubble detectors and poor statistics. The high sensitivity detector, when it observes a signal, skews yields upwards, and its observation of a signal is a statistical phenomenon.

Higher fidelity neutron detection is desired, such as a beryllium probe activation detector. While we have begun fielding this diagnostic on MAIZE, additional calibrations are required for improved performance. Additional tools such as neutron-time-of-flight (nTOF) detectors, neutron spectroscopes, and more activation detectors can shed more light on the neutron distribution. With tools to probe the subject of energy partitioning, a mechanism for conversion of kinetic energy to neutron radiation can be better understood.

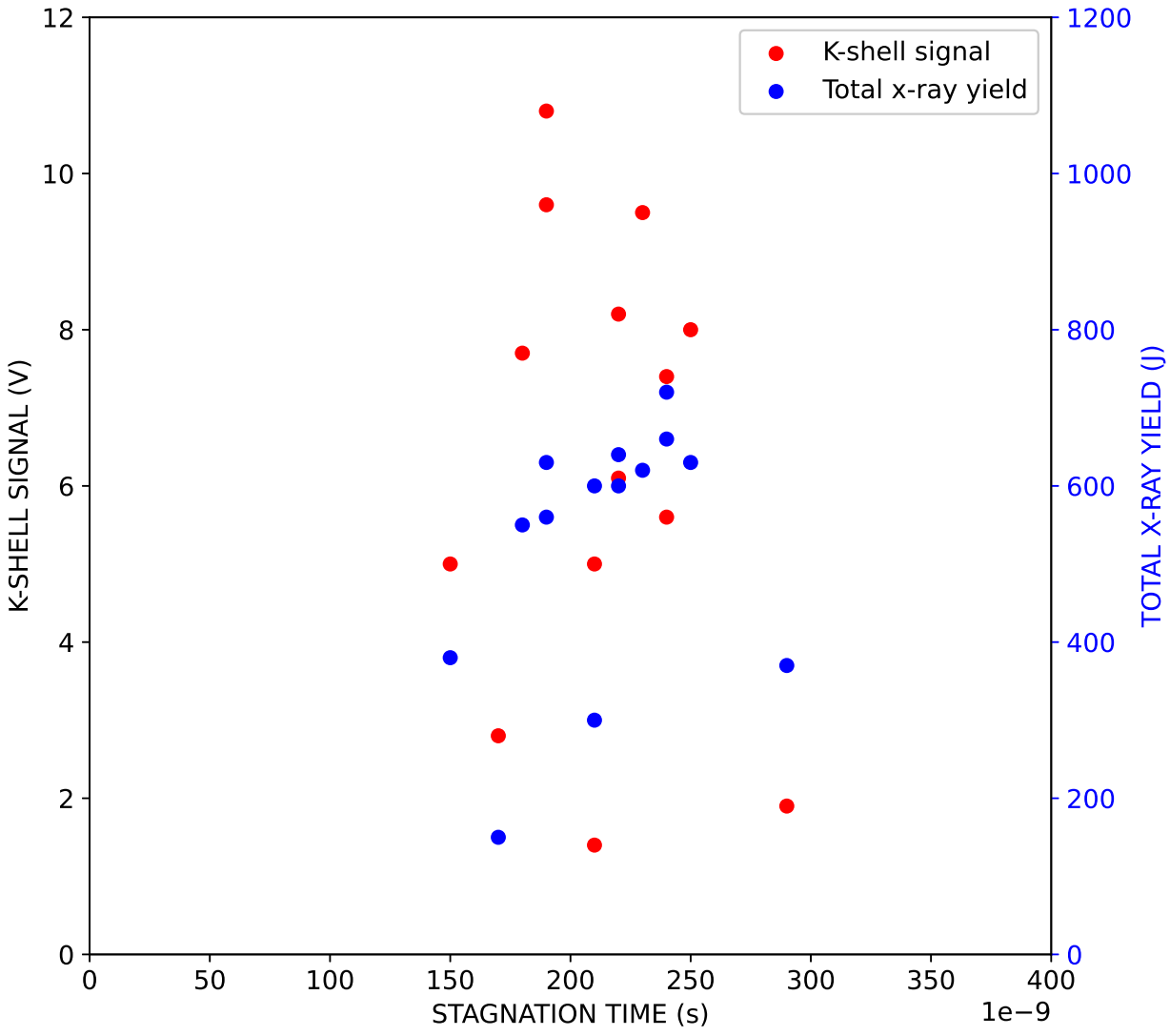

Figure 4.17: Plot of liner stagnation time versus K-shell signal and total x-ray yield to demonstrate the difference in liner dynamics that led to highest yields for each case. As seen, the highest K-shell signal were seen for low-intermediate liner masses with earlier stagnation times, while the highest total x-rays were observed for the intermediate-high liner masses with later stagnation times.

CHAPTER 5

Pre-Ionization Studies

5.1 Experimental Configuration

Having benchmarked the performance of the gas-puff z-pinch experiments with both outer and inner shells, each with argon and deuterium, we now turn to an examination of ostensible effects of an initial plasma distribution or pre-ionization on the z-pinch. This section focuses on the initial step of manufacturing and quantifying the pre-ionization distribution for each of the shells and for each of the gases, under optimum pinch conditions as determined in Chapter 4. As described in Chapter 1, the various pre-ionization mechanisms include electron beam, microwave, and ultraviolet irradiation. We developed an electron beam irradiation technique using a capacitor discharge, which creates a uniform plasma distribution in the gas-puff. The pre-ionization is timed to initiate after the gas-puff nozzles and fast-valves fire to create a well-collimated and azimuthally symmetric column of gas in the target region, but just prior to MAIZE discharging.

The pre-ionization with electron beam irradiation is carried out with a capacitor discharge through a velvet-tipped wire. A 240 nF capacitor is charged to 25 kV (for stored energy of 75 J) and discharged with a low-side spark-gap switch to output a positive voltage pulse. Note that the experiments of Chapter 4 made use of the logic circuit of Sec. 3.3.5, which could also potentially provide pre-ionization; the logic circuit was not used for the experiments presented here to avoid inadvertently complicating the pre-ionization distribution. This pulse is fed through into the vacuum chamber and to a thin copper wire that sits on a 3D printed tool 2.0 cm above the anode mesh, centered directly on the axis of the z-pinch. The copper wire is insulated in its entirety to prevent undesired arcing to miscellaneous metallic components that constitute the experimental region on MAIZE. The end of the wire is coated with velvet, which is a known electron source when pulsed with a sufficiently high voltage.

The pre-ionization distribution was imaged using the fast-framing camera, and characteristic images are presented in Fig. 5.1 for both the outer and inner shells. Experiments with similar setups involve using carbon bristles in various geometries above the gas-puff [26, 27]. We also

tested a ringed velvet-coated copper wire and determined a point source that sprayed electrons into the gas-puff target resulted in azimuthal symmetry and axial uniformity. The non-uniform plasma distribution of the ringed geometry is shown in Fig. 5.2. The pre-ionization pulse was diagnosed with a voltage and current monitor, which gave an estimate of the energy coupled into the initial plasma, as shown in Fig. 5.3. The integrated voltage and current product gives the energy output from the pre-ionizer. The oscillation in the energy is due to the inductivity of the circuit and the resistively coupled energy can be calculated at the zero-crossing of the current output from the pre-ionizer. Extrapolating these zero-crossings gives the energy coupled to the gas-puff when MAIZE is fired. MAIZE is selected to discharge 4.0 μs after the pre-ionization current pulse is initialized. With this delay selected, the pre-ionizer delivers approximately 6.5 J of energy to the gas-puff.

Assuming a neutral gas density distribution as determined in Sec. 4.1 and known ionization potentials for argon and deuterium, we can derive an average electron density. Note that a correction is made to account for the energy coupled to the gas that is not pinched by estimating the fraction of pre-ionization in the target region versus outside the target (i.e., between the anode mesh and the pre-ionization tool). These data are presented in detail in Sec. 5.2 and Sec. 5.3. Note that experimental confirmation of these calculations will be valuable in future studies (e.g., by fielding the interferometer developed in Sec. 3.4.1 during pre-ionization-only tests) as the coupling efficiency determined for the electron beam energy transferred to the gas-puff is currently only postulated as an upper bound.

5.2 Pre-Ionized vs Non-Pre-Ionized Argon Gas-Puff Z-Pinch Experiments

This section describes the pinch dynamics and energetics of argon gas-puff z-pinches with and without pre-ionization of the outer shell (Sec. 5.2.1) and the inner shell (Sec. 5.2.2). We select a constant 700 μs for the outer shell and a constant 500 μs for the inner shell as the time after the fast-valve of the outer-shell fires to discharge MAIZE, which is charged to ± 60 kV for each shot. We select a constant 4.0 μs as the time after the pre-ionizer pulser is fired for MAIZE to fire, at which point 6.5 J of pre-ionizing electrical energy is coupled to the gas. The electron distribution for a given neutral gas density distribution can be estimated with the number density distribution of argon in the geometry of the outer or inner shell.

5.2.1 Outer-Shell-Only Gas-Puff Z-Pinch Experiments

Outer shell argon gas-puff z-pinch experiments with and without pre-ionization were carried out with a plenum pressure of -13.4 psi. Referring to Fig. 4.3, this relates to a liner number density of

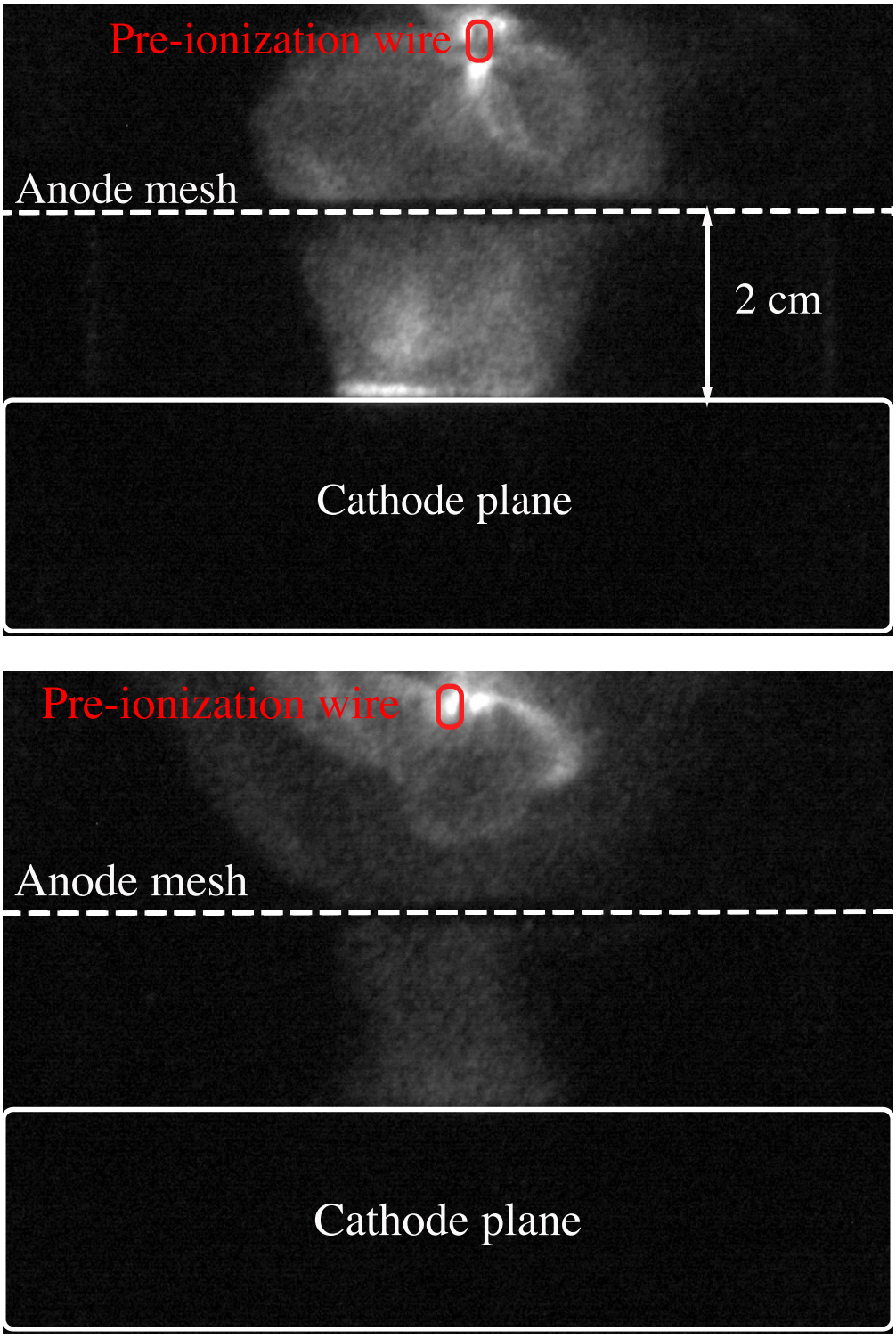

Figure 5.1: Characteristic pre-ionization distribution as imaged by the fast framing camera for the outer-shell (top) and inner-shell (bottom). A velvet-tipped thin copper wire sitting above the anode mesh created the initial plasma when pulsed with a 25 kV discharge. These images provide a first-order estimate of the electron distribution during the start of the MAIZE discharge.

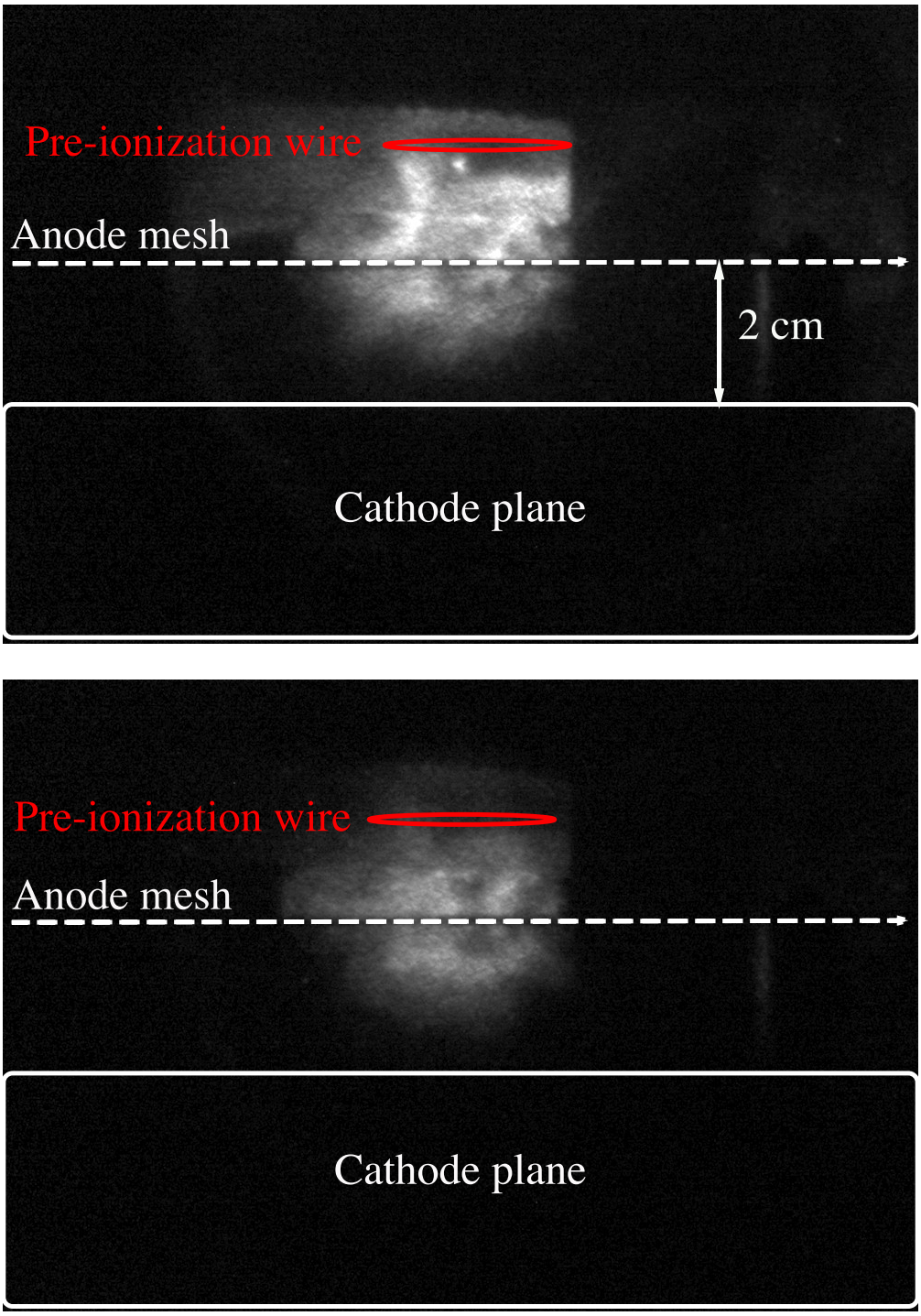

Figure 5.2: Undesirable asymmetries in the pre-ionization distribution as imaged by the fast framing camera for the outer-shell (top) and inner-shell (bottom). A velvet-tipped copper wire folded into a ring sitting above the anode mesh created the initial plasma when pulsed with a 25 kV discharge.

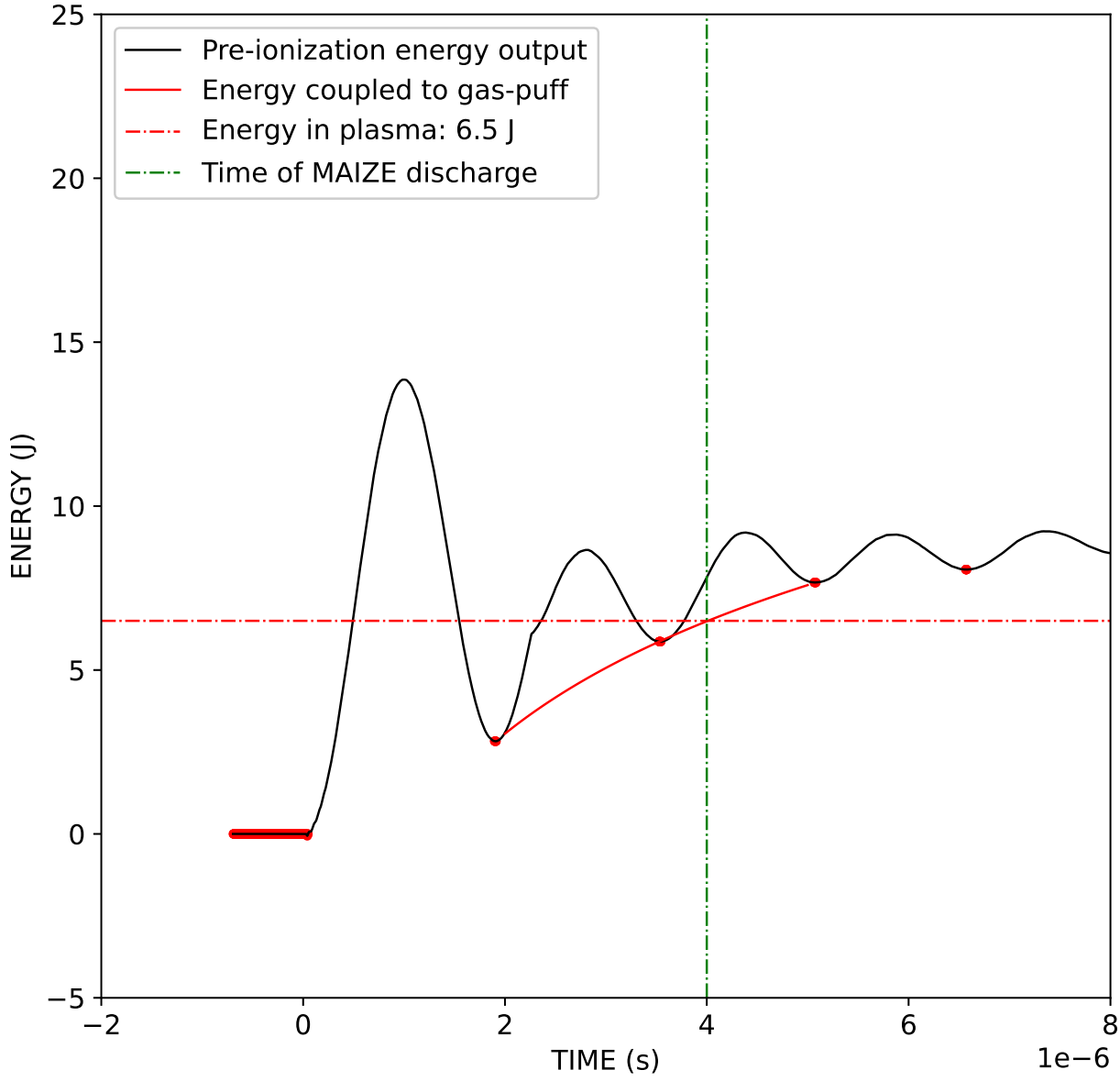

Figure 5.3: Characteristic energy output from the capacitor discharge of the pre-ionization circuit as calculated by integrating the current and voltage product. The oscillation is due to the current dynamics of an underdamped RLC circuit, whereby energy is shuttled between the plasma and the capacitor. The resistive energy coupled to the gas-puff can be calculated when the current is zero and extrapolated to when MAIZE is fired. The time of the MAIZE discharge is a constant 4.0 μs after the discharge of the pre-ionization pulser, when 6.5 J of energy has been coupled to the gas-puff.

0.015×10^{18} cm^{-3} (or a liner mass density of 1.0×10^{6} g·cm^{-3}). This provides an electron number density estimate of 9.0×10^{16} cm^{-3}, which is assumed to be uniformly distributed throughout the cylindrical shell geometry of the outer shell. Results for the pre-ionized shot (shot 2512) are contrasted with those form the non-pre-ionized shot (shot 2512) in Fig. 5.4 (top and bottom, respectively).

5.2.2 Inner-Shell-Only Gas-Puff Z-Pinch Experiments

Inner shell argon gas-puff z-pinch experiments with and without pre-ionization were carried out with a plenum pressure of -4.0 psi. Referring to Fig. 4.3, this relates to liner number density of 0.24×10^{18} cm^{-3} (or liner mass density of 10×10^{6} g·cm^{-3}). This provides an electron number density estimate of 7.2×10^{17} cm^{-3}, which is assumed to be uniformly distributed throughout the cylindrical shell geometry of the inner-shell. Results for the pre-ionized shot (shot 2513) is contrasted with those from the non-pre-ionized shot (shot 2514) in Fig. 5.5 (top and bottom, respectively).

5.3 Pre-Ionized vs Non-Pre-Ionized Deuterium Gas-Puff Z-Pinch Experiments

This section describes the pinch dynamics and energetics of deuterium gas-puff z-pinches with and without pre-ionization for the outer shell (Sec. 5.3.1) and the inner shell (Sec. 5.3.2). We select a constant 500 μs for the outer shell and a constant 300 μs for the inner shell as the time after the fast-valve of the outer-shell fires to discharge MAIZE, which is charged to ± 60 kV for each shot. We select a constant 4.0 μs as the time after the pre-ionizer pulser is fired for MAIZE to discharge, at which point 6.5 J of pre-ionizing electrical energy is coupled to the gas. The electron distribution for a given neutral gas density distribution can be estimated with the number density distribution of deuterium in the geometry of the outer or inner shell.

5.3.1 Outer-Shell-Only Gas-Puff Z-Pinch Experiments

Outer shell deuterium gas-puff z-pinch experiments with and without pre-ionization were carried out with a plenum pressure of -10.0 psi. Referring to Fig. 4.3, this relates to liner number density of 0.11×10^{18} cm^{-3} (or liner mass density of 0.7×10^{6} g·cm^{-3}). The deuterium is completely ionized to give an electron number density of 0.11×10^{18} cm^{-3}, which is assumed to be uniformly distributed throughout the cylindrical shell geometry of the outer shell. Results for the pre-ionized shot (shot 2785) are contrasted with those from the non-pre-ionized shot (shot 2781) in Fig. 5.6 (top

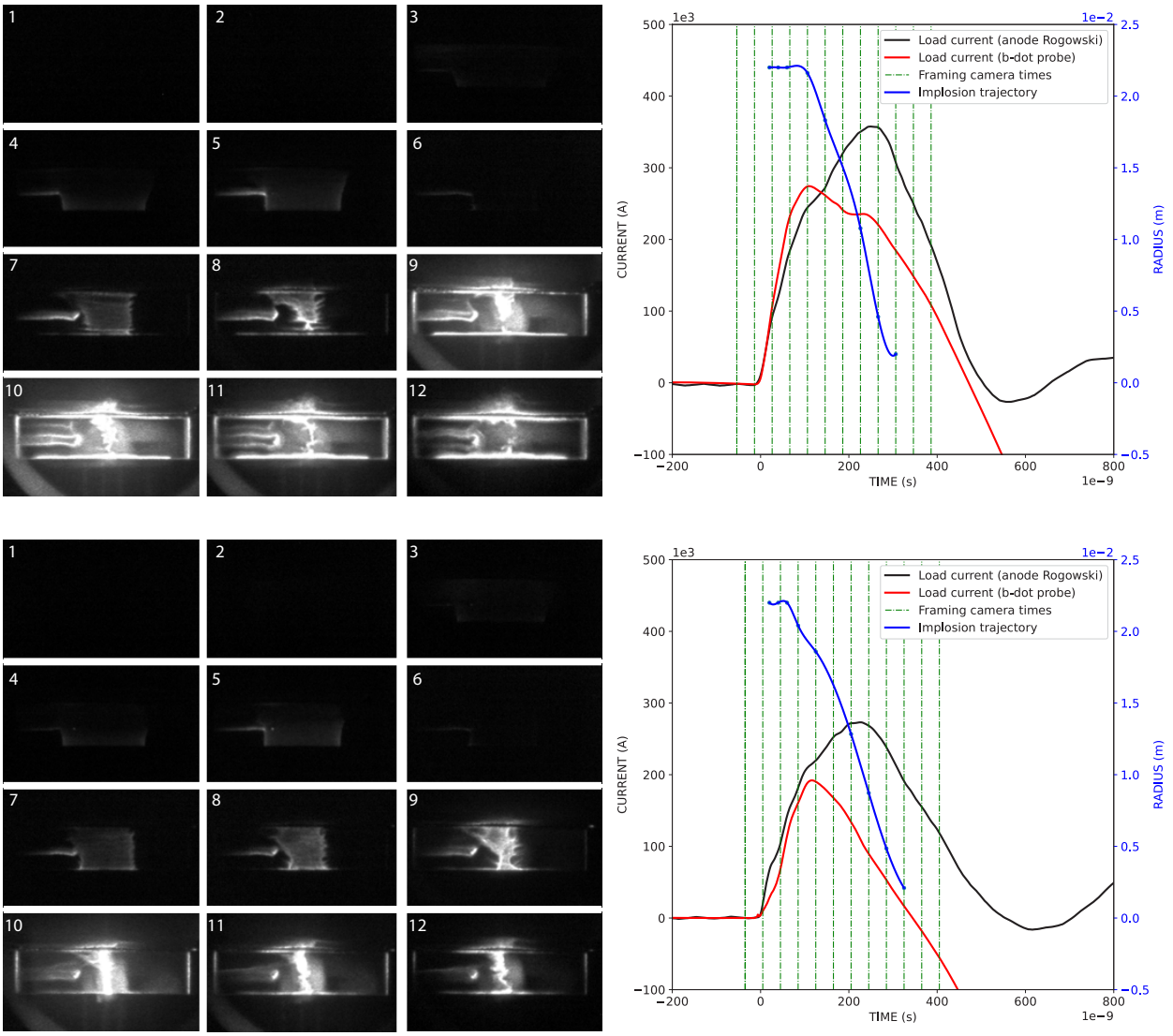

Figure 5.4: Summary of results for an argon outer-shell-only mass density of 14×10^{-6} g·cm^{-3} with (top) and without (bottom) pre-ionization. The sequence of images on the top and bottom left show the fast-framing camera images of the implosion. The plots on the top and bottom right show the current pulse as measured with an anode Rogowski and a B-dot probe fielded at small radius, timing of the fast-framing camera images, and implosion trajectory.

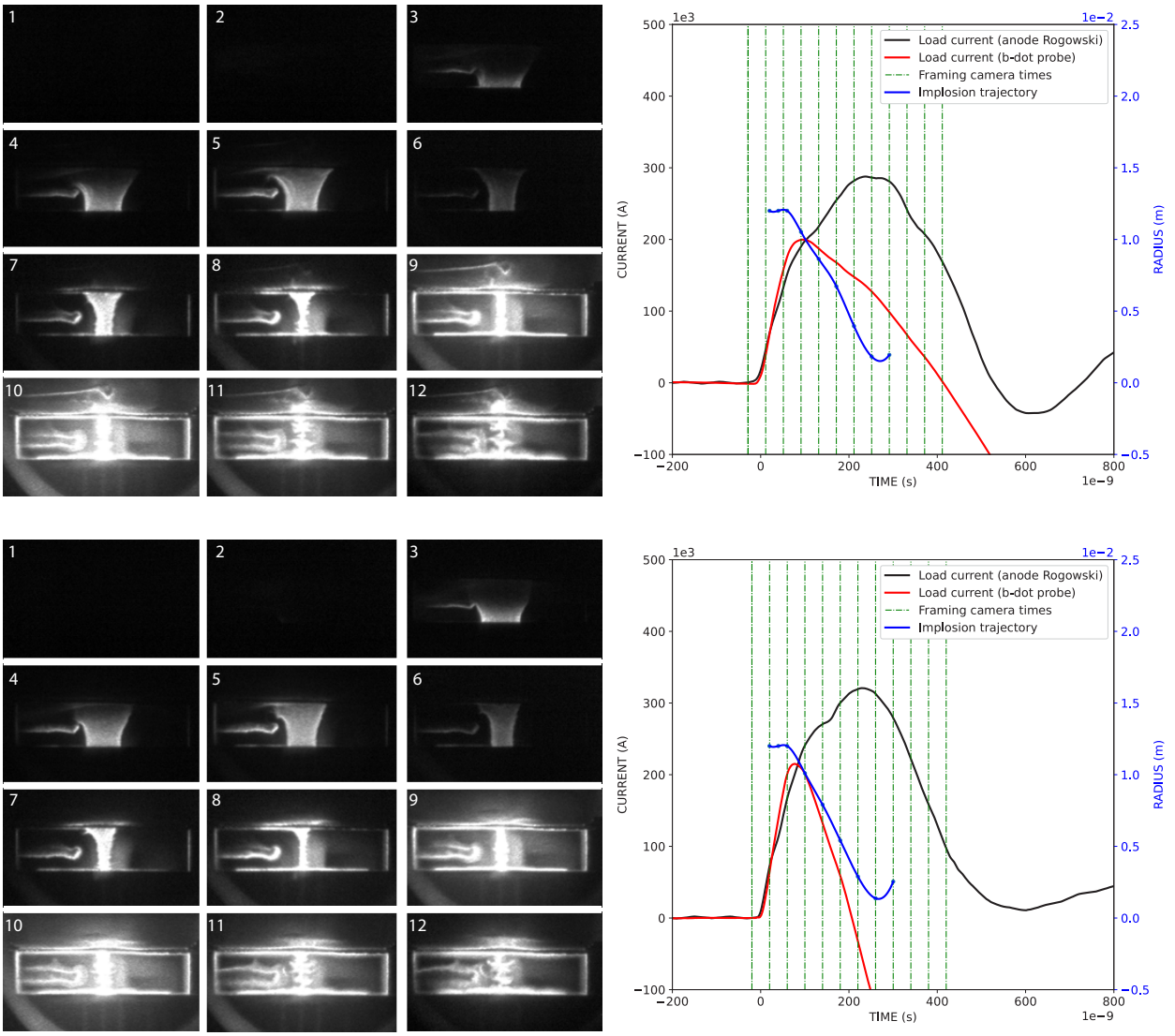

Figure 5.5: Summary of results for an argon inner-shell-only mass density of 14×10^{-6} g·cm^{-3} with (top) and without (bottom) pre-ionization. The sequence of images on the top and bottom left show the fast-framing camera images of the implosion. The plots on the top and bottom right show the current pulse as measured with an anode Rogowski and a B-dot probe fielded at small radius, timing of the fast-framing camera images, and implosion trajectory.

and bottom, respectively). Shot 2785 results in a neutron yield of 2.3×10^7 neutrons as measured on-axis and 2.9×10^7 neutrons as measured off-axis. Shot 2781 results in a neutron yield of 1.5×10^6 neutrons as measured on-axis and neutrons below the detector threshold as measured off-axis.

5.3.2 Inner-Shell Gas-Puff Z-Pinch Experiments

Inner shell deuterium gas-puff z-pinch experiments with and without pre-ionization were carried out with a plenum pressure of -4.0 psi. Referring to Fig. 4.3, this relates to liner number density of 0.24×10^{18} cm^{-3} (or liner mass density of 14×10^6 g·cm^{-3}). The deuterium is completely ionized to give an electron number density of 0.24×10^{18} cm^{-3}, which is assumed to be uniformly distributed throughout the cylindrical shell geometry of the inner shell. Results for the pre-ionized shot (shot 2798) are contrasted with those from the non-pre-ionized shot (shot 2796) in Fig. 5.7 (top and bottom, respectively). Shot 2798 results in a neutron yield of 9.3×10^6 neutrons as measured on-axis and neutrons below the detector threshold as measured off-axis. Shot 2796 results in a neutron yield of 1.3×10^8 neutrons as measured on-axis and 1.5×10^6 neutrons as measured off-axis.

5.4 Discussion and Summary

5.4.1 Current Delivery

The MAIZE current pulse was diagnosed with an anode Rogowski coil and with a B-dot probe at small radius. The B-dot was fielded at 1.0 cm from the center of the pinch for the argon shots and 2.0 cm from the center of the pinch for the deuterium shots. It was used in order to quantify the current being delivered to the pinch and to quantify possible losses in the transmission line between the anode Rogowski and the pinch. The results from these diagnostics are summarized in Table 5.1.

The data presented above shows that current delivered to the pinch for argon in the outer-shell and inner-shell is largely insensitive to the 6.5 J of pre-ionization. The amplitude of the current as measured by the B-dot is smaller than that measured by the anode Rogowski, which suggests imperfect delivery of current to small radius. Furthermore, the rise-time of the current as measured by the B-dot probe is smaller than that measured by the anode Rogowski. This points to current being carried at large radius by diffuse plasma and not by the pinch at later stages of the implosion. However, the current reversal time for both shells with pre-ionization is smaller than without pre-ionization, which suggests that pre-ionization improved the ability of the pinch to carry current.

Current delivery with deuterium pinches, on the other hand, was sensitive to pre-ionization.

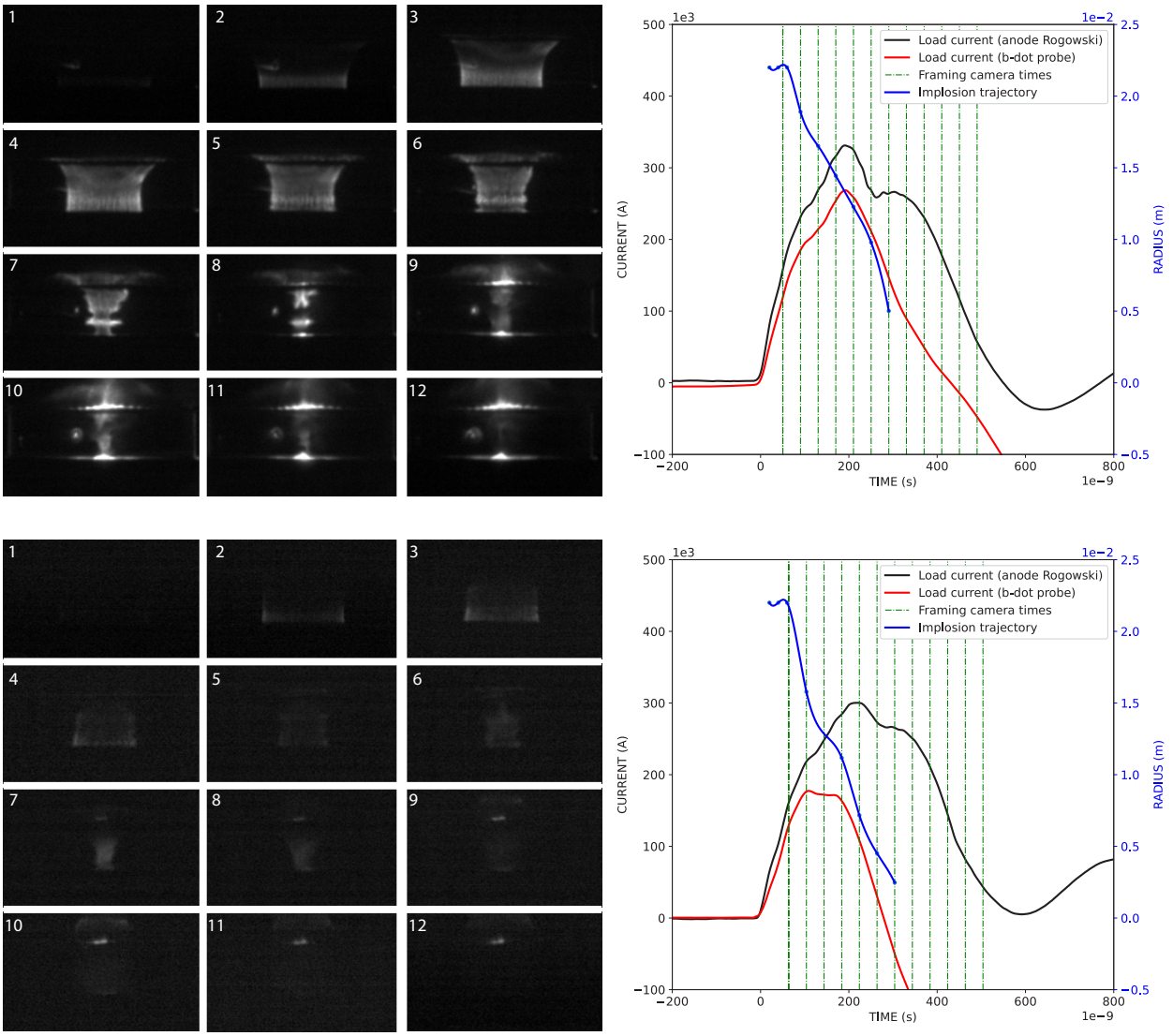

Figure 5.6: Summary of results for a deuterium outer-shell mass density of 14×10^{-6} g·cm^{-3} with (top) and without (bottom) pre-ionization. The sequence of images on the top and bottom left show the fast-framing camera images of the implosion. The plots on the top and bottom right show the current pulse as measured with an anode Rogowski and a B-dot probe fielded at small radius, timing of the fast-framing camera images, and implosion trajectory.

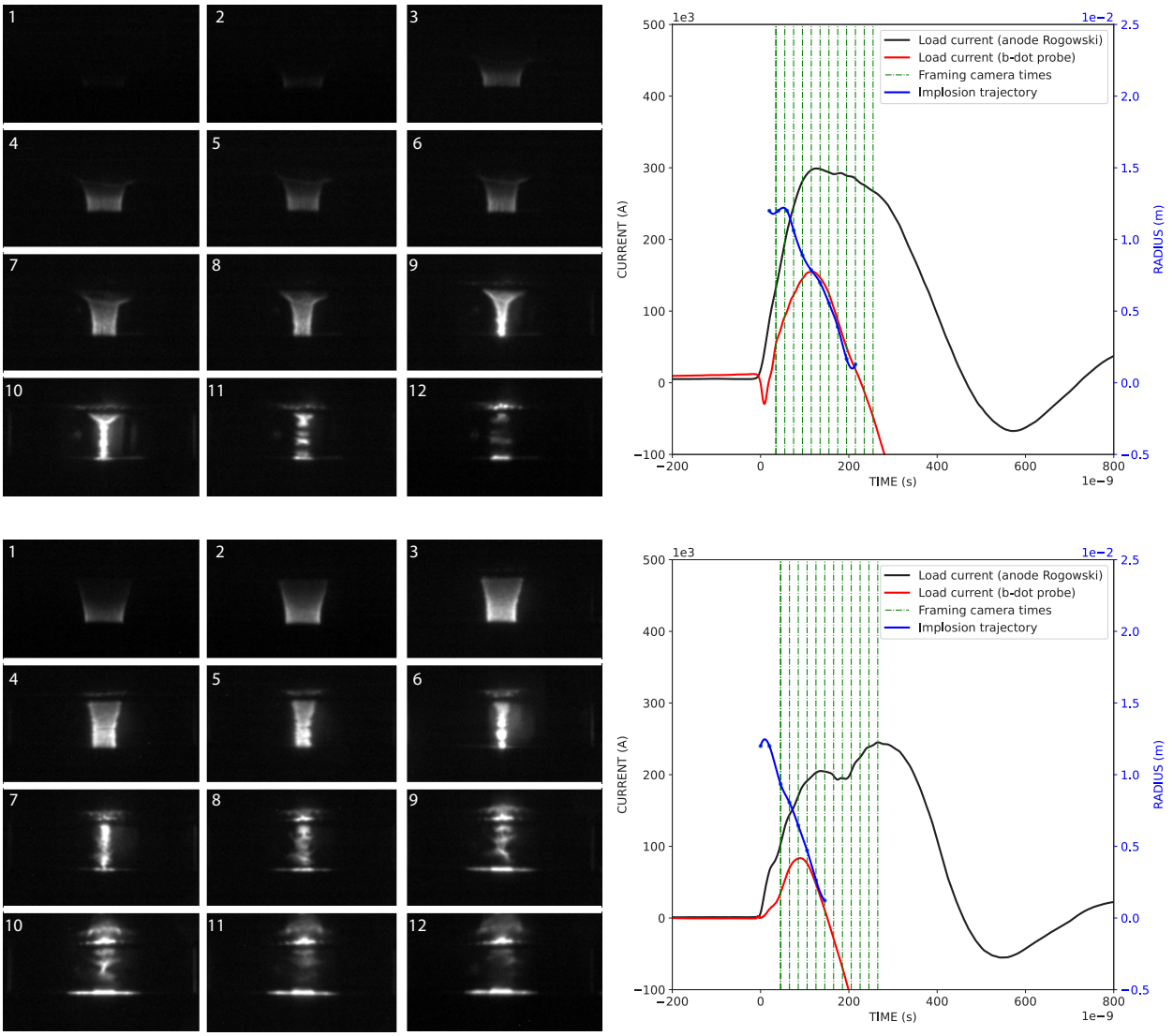

Figure 5.7: Summary of results for a deuterium inner-shell mass density of 14×10^{-6} g·cm^{-3} with (top) and without (bottom) pre-ionization. The sequence of images on the top and bottom left show the fast-framing camera images of the implosion. The plots on the top and bottom right show the current pulse as measured with an anode Rogowski and a B-dot probe fielded at small radius, timing of the fast-framing camera images, and implosion trajectory.

While the outer-shell and inner-shell both had imperfect current delivered to the pinch as diagnosed by the mismatch in current amplitudes with each diagnostic, there was a difference between the pre-ionized and non-pre-ionized cases. The outer-shell saw increased current delivered to the pinch with, pre-ionization whereas the inner-shell saw decreased current delivered to the pinch with pre-ionization. Additionally, the B-dot measurement of the current in the outer-shell experiment has a rise-time identical to that measured by the anode Rogowski suggesting that current is being carried by the pinch later in time. The opposite is true with the inner-shell: the anode Rogowski sees an inductive dip followed by current amplification, which is consistent with a rapidly exploding pinch, following stagnation.

Note that the B-dot fielded is a simple wire loop and not a differential B-dot due to the limited space available to field the diagnostic at such a small radius. This means that systemic bias in the measurements are not addressed. A differential B-dot with a small footprint can be fielded to better account for this possible biasing of the data and to better diagnose the current delivered to the pinch. Higher fidelity current measurements with a Faraday rotation or Zeeman splitting diagnostics can improve an understanding of current delivery to the pinch and effects of pre-ionization therein.

5.4.2 Neutron Yield Efficiency

Neutron yield with deuterium pinches was also sensitive to pre-ionization. The results from these experiments are summarized in Table 5.2. The outer-shell in particular experiences the most dramatic change with a neutron yield from on the order of 10^7 neutrons with pre-ionization to a neutron yield of on the order of 10^6 without pre-ionization. Note that the outer-shell was not a prolific neutron source to begin with. The neutron yields with the inner-shell are oppositely affected, with neutron yields of on the order of 10^6 with pre-ionization and neutron yields on the order of 10^8 without pre-ionization. In summary, the performance of the outer-shell deuterium pinch is improved by pre-ionization, whereas that of the inner-shell deuterium pinch is much deteriorated. We emphasize here that this sensitivity to pre-ionization is only tested with a particular pre-ionization distribution; it cannot be concluded that all small-radius deuterium pinches are affected detrimentally by pre-ionization. Nor can it be concluded that all large-radius pinches are improved. Note that while summary results from characteristic shots are presented in Sec. 5.2 and Sec. 5.3, the behaviors discussed were repeatedly observed over several shots for each parameter tested.

Table 5.1: Summary of Pre-Ionization Effects on Current Distribution

Shot No.	Gas; Shell	PI	Pressure (psig)	Mass Density ($g \cdot cm^{-3}$)	Rog Peak Current ($\pm 5 \times 10^3$A)	Rog Rise Time ($\pm 5 \times 10^{-9}$ s)	B-dot Peak Current ($\pm 25 \times 10^3$A)	B-Dot Rise Time ($\pm 5 \times 10^{-9}$ s)
2512	Argon; Outer	Y	-13.4	1.0×10^{-6}	360×10^3	260×10^{-9}	270×10^6	110×10^{-9}
2511	Argon; Outer	N	-13.4	1.0×10^{-6}	270×10^3	230×10^{-9}	190×10^3	110×10^{-9}
2513	Argon; Inner	Y	-4.0	15×10^{-6}	290×10^3	240×10^{-9}	200×10^3	90×10^{-9}
2514	Argon; Inner	N	-4.0	15×10^{-6}	320×10^3	230×10^{-9}	210×10^3	80×10^{-9}
2785	D2; Outer	Y	-10.0	0.7×10^{-6}	330×10^3	190×10^{-9}	270×10^3	190×10^{-9}
2781	D2; Outer	N	-10.0	0.7×10^{-6}	300×10^3	220×10^{-9}	180×10^3	110×10^{-9}
2798	D2; Inner	Y	-2.0	12×10^{-6}	300×10^3	130×10^{-9}	150×10^3	110×10^{-9}
2796	D2; Inner	N	-2.0	12×10^{-6}	200×10^3	140×10^{-9}	80×10^3	90×10^{-9}

Table 5.2: Summary of Pre-Ionization Effects on Neutron Yield Efficiency

Shot No.	Gas; Shell	PI	Pressure (psig)	Mass Density ($\mathrm{g \cdot cm^{-3}}$)	Rog Peak Current ($\pm 5 \times 10^3$A)	Rog Rise Time ($\pm 5 \times 10^{-9}$ s)	Neutron Yield (On-Axis)	Neutron Yield (Off-Axis)
2785	D2; Outer	Y	-10.0	0.7×10^{-6}	330×10^3	190×10^{-9}	2.3×10^7	2.9×10^7
2781	D2; Outer	N	-10.0	0.7×10^{-6}	300×10^3	220×10^{-9}	1.5×10^6	0
2798	D2; Inner	Y	-2.0	12×10^{-6}	300×10^3	130×10^{-9}	9.3×10^6	0
2796	D2; Inner	N	-2.0	12×10^{-6}	200×10^3	140×10^{-9}	1.3×10^8	1.5×10^6

CHAPTER 6

Refining the Pre-Ionization Paradox

6.1 Summary

This dissertation presents the development of a gas-puff z-pinch experimental platform for the 1-MA, 200-ns MAIZE linear transformer driver, experimental studies benchmarking the behavior of this experiment, and effects of pre-ionization on the performance of the gas-puff z-pinch. The dynamics of the pinch were modeled with simple zero-dimensional codes to confirm the feasibility of fielding such an experiment on MAIZE. The experiment hardware was then developed and integrated. It can create a z-pinch target consisting of two hollow shells (an outer shell with inner radius of 2.0 cm and outer radius of 2.2 cm, and an inner shell with inner radius of 0.9 cm and outer radius of 1.0 cm). A central jet can be added to the system in the future. The jet and shells can be fielded together or individually, and each can also be uniquely pressurized with a unique gas species. Furthermore, the experiment is non-destructive on a shot-to-shot basis, and a high repetition rate can be achieved for large parameter scans and to acquire statistically significant data. With this platform, up to 30 shots per day has now been demonstrated; the shot rate can exceed 50 shots a day if desired. The development of the gas-puff platform in addition to the components and diagnostics supporting the platform are presented in Chapter 3.

The experimental hardware, which consists of a set of nozzles and fast-valves, were then experimentally tested, as described in Chapter 4. The hardware was first benchmarked by using a newly developed 2D interferometer. This process quantified the time evolution of the density distribution of the gas in the z-pinch target with respect to the pressure of the stored gas in the valves. The results are presented in Sec. 4.1. A range of density distributions, as created with both the outer-shell and inner-shell, each with argon and deuterium gas, was also tested via full z-pinch implosions on MAIZE to study the pinch physics and to determine the optimal conditions with respect to the various parameters under user control. The outer-shell-only experiments are presented in Sec. 4.2.1 for argon and in Sec. 4.2.2 for deuterium. The inner-shell-only experiments are presented in Sec. 4.3.1 for argon and in Sec. 4.3.2 for deuterium. It was determined that the inner-shell is a more prolific

x-ray source, with peak yields of up to 720 J, as opposed to 400 J with the outer-shell. The highest total x-ray yields were obtained from shots where the stagnation occurred after peak current, when the current had dropped to 90% of it's peak value. By contrast, the highest K-shell signals were obtained from shots where the stagnation occurred just prior to peak current. The inner-shell is also a more abundant neutron source (when using deuterium) with peak yields of $\sim 10^8$ neutrons per shot, as opposed to the outer-shell, which had peak yields of $\sim 10^7$ neutrons per shot. The highest neutron yields were obtained from shots where the stagnation occurred just prior to peak current. These short stagnation times were inaccessible to the outer-shell. Nevertheless, when used in conjunction with the inner-shell, the outer shell was useful in studies of shell-on-shell stabilization of the MRT instability, as was demonstrated in Sec. 4.4.

With an understanding of the performance of the newly built gas-puff z-pinch platform, we tested the effects of pre-ionization by electron beam irradiation of the gas, as presented in Chapter 5. The experimental configuration is presented in Sec. 5.1, where a thin, velvet-tipped copper wire is employed to generate the pre-ionization when pulsed with a 25 kV, 75 J pulse. The pulser coupled 6.5 J of energy to the gas-puff, which is sufficient to partially ionize argon and to fully ionize deuterium. Estimates of the electron distribution and its effects on the z-pinch is provided for argon outer-shell experiments in Sec. 5.2.1 and argon inner-shell experiments in Sec. 5.2.2. While the pinch dynamics were largely unchanged by the pre-ionization for both argon shells, it was observed that pre-ionization improved late-time current coupling to the pinch. Estimates of the electron distribution and its effects on the z-pinch is provided for deuterium outer-shell experiments in Sec. 5.3.1 and deuterium inner-shell experiments in Sec. 5.3.2. Here, the outer-shell responded favorably to pre-ionization, where the current coupled to the pinch increased at both early and late times. The neutron yield increased from $\sim 10^6$ without pre-ionization to $\sim 10^7$ with pre-ionization. The inner-shell, on the other hand, degraded with pre-ionization, where less current was coupled to the pinch overall and neutron yields decreased from $\sim 10^8$ to $\sim 10^7$.

6.2 Future Work

Several upgrades to the gas-puff z-pinch platform on the MAIZE linear transformer driver can be implemented to improve user understanding of its performance better. All gas lines connecting the gas manifold to the various valves and to the plena of the gas-puff nozzle and fast-valve assembly should be upgraded to aluminum or copper. Making just such a replacement for the lengthy lines connecting the gas manifold to the plena improved reproducibility as discussed in Sec. 4.5.2. Doing so for the minor sections connecting components within the gas manifold as well as from the gas manifold to the vacuum pump should ostensibly result in further improvements. Similarly, better vacuum in the gas lines may be achieved with installation of a turbo pump and by baking out the

lines. It is also important to better understand the relationship between the valve driver voltage for each of the shells and the gas density distribution formed. This will allow the drivers to be pulsed with as low voltage as necessary that ensures a desired distribution, ostensibly improving the lifetime of the fast-valves.

Interferometry can be fielded under a wider range of circumstances to better understand the nozzle and fast-valve behavior. In particular, it can be fielded to better fill out the lines of best fit in Fig. 4.3 and do so with other gases. These can be benchmarked against independent density diagnostics such as planar-laser-induced-fluorescence to ensure self-consistency between these techniques. Interferometry can also be fielded to quantify the initial plasma distribution from the pre-ionization process. This will provide better quantified initial conditions, which can be directly input into computer codes. Improved implementation of other existing diagnostics can yield more valuable information on the physics of the z-pinch. For instance, bubble detectors and the beryllium activation probe can be fielded over a range of polar angles to better quantify the anisotropy of the neutron yield. Multiple differential B-dot probes can be fielded at varying radii close to the target to understand the details of the current delivered to the target. Additional higher-fidelity current diagnostics such as Faraday rotation or Zeeman splitting can also be fielded to better understand the details of the current delivery.

Benchmarking experiments should be repeated after MAIZE refurbishments where current delivered to the target is improved. This may improve yield efficiencies. It may also allow the outer-shell experiments to be carried out in the more efficient regime when stagnation takes place closer to the peak of the current pulse. This will allow interesting phenomena more readily observable with the outer-shell-only experiments (i.e., MRT instabilities) to be better studied and quantified. Benchmarking experiments should also be carried out with additional gases to examine their K-shell signature and the mechanisms for producing these. With a Thomson scattering diagnostic, these results could also better shed light on the puzzle of how energy is partitioned in the gas-puff z-pinch implosion.

More tests need to be carried out to seed the pre-ionization plasma in a reproducible and symmetric fashion. Lasers could be used to ionize a region of the gas-puff. This technique could also allow for deliberate seeding of azimuthal non-uniformities to test their effects on the implosion dynamics. Furthermore, it would also protect the experiment from noise, which is a notorious feature the pre-ionizer pulser. It is evident from this section that the mysteries of the z-pinch abound. Any combination of the various experimental and diagnostics elements outlined in this dissertation can be fielded and improved upon to pursue a desired query in the z-pinch process.

6.3 Conclusion

Contrasting the results presented in this dissertation with those obtained by previous studies from the literature, as summarized in Chapter 1, confirms the complexities in the study of pre-ionization on the gas-puff z-pinch. It is important to note that comparing and contrasting between studies is an intricate task, due to the nuanced differences in experimental setups between institutions. This is to say that certain results obtained with a certain experiment can disagree with or even contradict results obtained with a different experiment. This dissertation presents a uniform experimental platform as two parameters are changed in the pre-ionization studies: the liner radius and the gas species. As such, these results can then presumably respond to the pre-ionization paradox presented in Chapter 1 regarding the incompatible, sometimes irreconcilable, effects of pre-ionization on the behavior of the gas-puff z-pinch. In fact, depending on the details of the configuration, this dissertation presented results where pre-ionization either improved performance, degraded performance, or had little to no effect on performance. Therefore the central thesis presented in this dissertation is that it is no longer sufficient to treat the effects of pre-ionization on the z-pinch as a binary result; it is not enough to claim that pre-ionization is "good" or "bad". Instead, the discourse needs to be more nuanced: a particular pre-ionization distribution has a particular effect on a particular behavior of a particular gas species. The differing results at peer institutions differed precisely *because* pre-ionization has differing effects on differing setups. The importance of understanding this aspect of the gas-puff z-pinch cannot be overstated— it can better validate computer codes, which can then have greater predictive capabilities; it can result in better optimized pinch conditions for the various applications of the z-pinch; and ultimately, it can improve human understanding of the universe, if for nothing else than to satisfy our curiosity.

APPENDIX A

Optimization of MAIZE Switch Diagnostics

As discussed in Sec. 3, the MAIZE LTD consists of the parallel connection of fast capacitors and switches around the outer perimeter of a metallic cylindrical cavity. These capacitors and switches are grouped together in units called "bricks". Each brick consists of an upper and lower capacitor, connected in series with each other through the breakdown (closure) of a pressurized spark-gap switch. MAIZE consists of 40 such bricks. When the bricks are charged to $\pm$100 kV and then discharged synchronously, MAIZE generates a 1 MA current pulse with a rise-time of 200 ns into a matched load impedance.

The capacitors in a brick are rapidly discharged when the switch is closed, driving a current pulse into the experiment of interest. The spark-gap switch is closed by applying a high-voltage pulse to the trigger electrode, which is positioned between the positively charged anode and the negatively charged cathode. All of the electrodes are housed within the switch's pressurized, dielectric body. The applied voltage pulse ionizes the gas, which 'closes' the switch and allows the capacitors to discharge. The breakdown of the gas also results in the emission of light, which can be monitored as a proxy for switch performance since the light emitted is temporally correlated with the switch closing.

Monitoring switches by their output light provides information about when the switches first close and thus when the capacitors first begin to discharge. Knowing when each switch closes is crucial for producing the desired current pulse and thus the desired experimental conditions [62]. For example, some experiments require that all the switches close simultaneously, while other experiments require that the switches close at varied, yet predetermined times in order to customize the current pulse delivered to the load [63].

The diagnostic system presented herein is set up such that light from a switch is collected by an optical fiber, which is coupled to a photomultiplier tube (PMT). The PMT converts collected light into a voltage signal, which is monitored by an oscilloscope channel. Monitoring each switch with a dedicated fiber-PMT-oscilloscope channel requires 40 such channels on MAIZE, which was problematic for our laboratory, as 40 PMT-oscilloscope channels were not available. This appendix

establishes a framework for optimizing a fiber-based switch diagnostics scheme for limited PMT-oscilloscope channels. This is done by assigning each switch to a unique combination of PMTs. A pre-firing (or late-firing) switch can then be identified by the unique combination of PMT output pulses.

A.1 Operating Theory Based on Boolean Logic

Optimizing switch diagnostics to require fewer PMTs and oscilloscope channels can be accomplished by implementing a logic circuit after light from the switches is collected. In particular, a light circuit can be set up using a network of light-collecting fiber optic cables such that each PMT functions as a binary digit or bit. In this approach, a given PMT is either in an 'on' state (collecting light) or in an 'off' state (not collecting light) at each point in time. Note that a given PMT is in an 'on' state if any one of the switches coupled to the PMT is emitting light, while the PMT is in an 'off' state only if all of the switches coupled to the PMT are not emitting light.

With N PMTs functioning as bits, one can distinctly represent

$$2^N = X + 1 \tag{A.1}$$

characters, where X is the number of switches. Given X switches, solving for N provides the minimum number of PMTs required to represent each switch independently. This is shown by

$$N = \lceil \log_2 (X + 1) \rceil \tag{A.2}$$

where $\lceil \rceil$ is a ceiling function that rounds up its argument, $\log_2 (X + 1)$, to the next whole number. With $X = 40$ switches on MAIZE, the fewest number of PMTs needed to uniquely identify a pre-firing or late-firing switch is $N = 6$.

This diagnostic technique requires coupling each switch to a unique *combination* of PMTs (as opposed to a unique *permutation* of PMTs). A combination of PMTs is a selection of a subset of PMTs from the total, such that the order of selection does not matter— selecting PMT "1" and "2" is the same as selecting PMT "2" and "1". A permutation of PMTs is a selection where the order does matter— selecting PMT "1" and "2" is *not* the same as selecting PMT "2" and "1".

With a unique combination of PMTs coupled to each switch, the firing of a single switch can then be identified by the combination of PMTs that are turned on. The available combinations are determined using binomial coefficients,

$$\binom{N}{k} = \frac{N!}{k!(N-k)!} \tag{A.3}$$

which give the number of ways to choose a subset of k elements from a set of N elements. Each switch is assigned to one of these combinations. Figure A.1 provides an example of what such a circuit would look like in order to monitor ten switches. Note that there is one way to choose 0 elements from a set: $\binom{N}{0} = 1$, which corresponds to assigning a switch to zero PMTs. However, this assignment is not used since it does not actually monitor any switches. This offset in the number of available, practical assignments is accounted for by the '+1' on the right hand side of Eqn. A.1.

On MAIZE (having calculated that we need a minimum of six PMTs to monitor 40 switches) there are $\binom{N}{k} = \binom{6}{1} = 6$ ways to choose one PMT, which implies that each of the first six switches get assigned to each of the six PMTs. There are $\binom{N}{k} = \binom{6}{2} = 15$ ways to choose two PMTs, which corresponds to a further 15 switches getting assigned, albeit to two PMTs instead of one. The remaining 19 switches are assigned to three PMTs by choosing three PMTs from the set of six [i.e., $\binom{N}{k} = \binom{6}{3} = 20 > 19$]. In this manner, a minimum of six PMTs allows diagnosis of 40 individual switches. Note that, while only six PMTs are needed, the system implemented on MAIZE uses seven PMTs, since seven PMTs and oscilloscope channels were already available (see Sec. A.2).

Note that other switch diagnostic schemes could be implemented. For instance, the output light from each switch could be monitored by an inexpensive photodiode, converting the light signal into a digital electrical signal ('0' for no light; '1' for light). The digital signal from each photodiode could then be fed into one of the inputs of a resistor ladder, so that the digital voltage from the first photodiode gets divided by 1, the second by 2, the third by 4, and so on. The total resistor ladder output voltage (the sum of all the scaled photodiode voltages) then uniquely identifies the combination of firing switches. Analyzing the amplitude of the summed signal would then allow pre-firing or late-firing switches to be identified. Mathematically, a resistor ladder of arbitrary length could be constructed such that any number of switches could be monitored using a single ladder-oscilloscope channel. In practice, however, this technique is limited by noise levels on the oscilloscope. Nevertheless, each oscilloscope channel should be able to resolve eight switches, which means that the number of oscilloscope channels required to monitor all 40 switches on MAIZE could be reduced to five. Another benefit of the resistor ladder technique is that there is only one fiber per switch. For these reasons, the resistor ladder solution could be quite useful for smaller facilities like MAIZE. However, we note that the number of oscilloscope channels required to monitor a given number of switches grows linearly with the number of switches to be monitored, which is not as favorable as the logarithmic scaling of the Boolean technique demonstrated here. For example, to monitor 100,000 switches (see Sec. A.4), a resistor ladder solution might require 12,500 oscilloscope channels, while the Boolean technique demonstrated here could require as few as 17 oscilloscope channels.

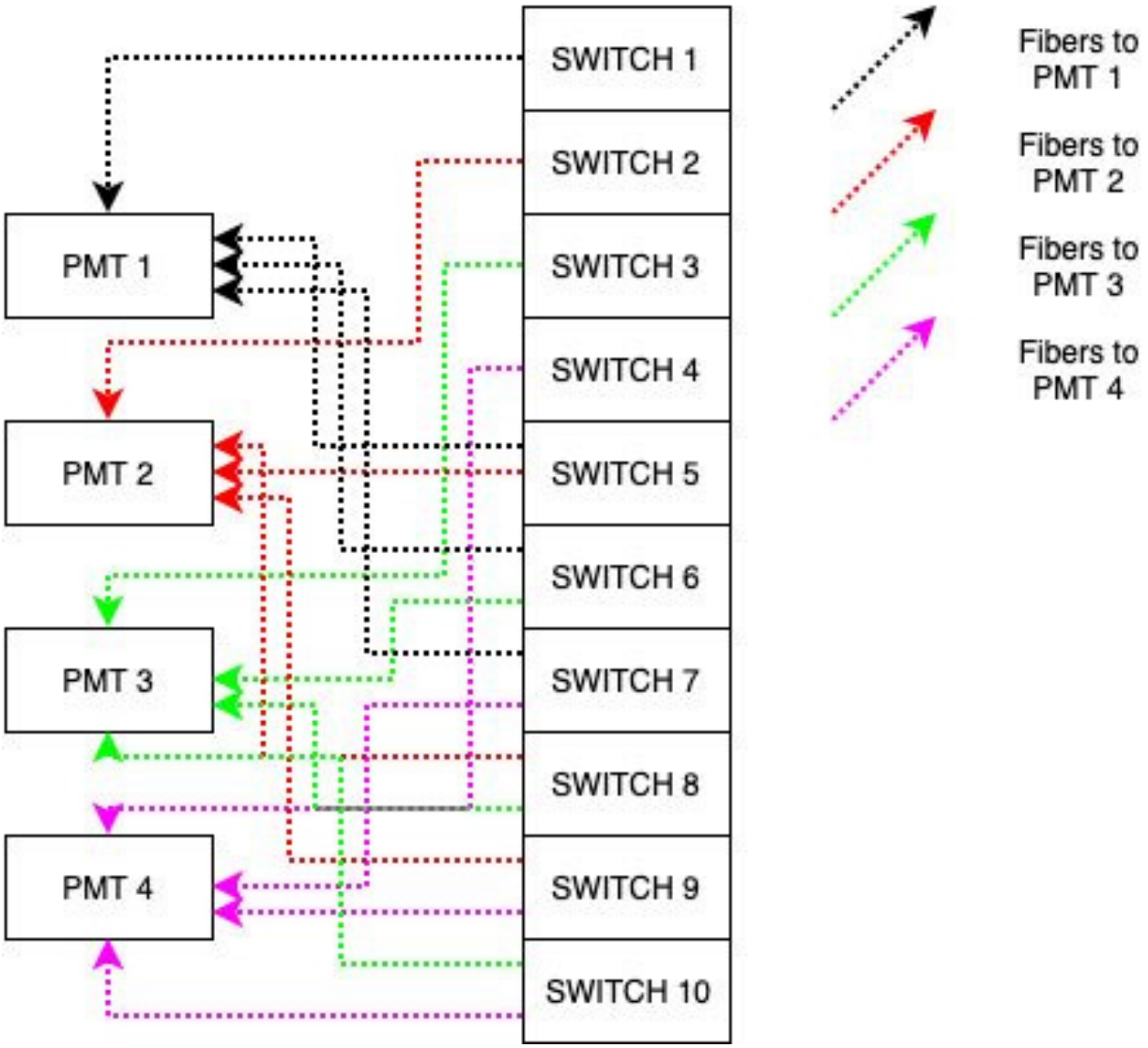

Figure A.1: An example of how four PMT-oscilloscope channels can be used to monitor 10 switches.

Table A.1: PMT Assignments on MAIZE

SWITCH	PMT(s)	SWITCH	PMT(s)
1	1	21	3,6
2	2	22	3,7
3	3	23	4,5
4	4	24	4,6
5	5	25	4,7
6	6	26	5,6
7	7	27	5,7
8	1,2	28	6,7
9	1,3	29	1,2,3
10	1,4	30	1,2,4
11	1,5	31	1,2,5
12	1,6	32	1,2,6
13	1,7	33	1,3,4
14	2,3	34	1,3,7
15	2,4	35	2,3,5
16	2,5	36	4,5,6
17	2,6	37	4,5,7
18	2,7	38	3,6,7
19	3,4	39	4,6,7
20	3,5	40	5,6,7

A.2 Implementation on the MAIZE Facility

Coupling 40 spark-gap switches on MAIZE to unique combinations of PMTs allows for their monitoring using exponentially fewer PMT-oscilloscope channels than monitoring each switch with its own, dedicated PMT-oscilloscope channel. While 40 switches can be monitored with only 6 PMTs (as calculated in Sec. A.1), the system on MAIZE was implemented with seven PMTs because we already had seven PMT-oscilloscope channels available. As such, we assigned $\binom{N}{k} = \binom{7}{1} = 7$ switches to one PMT; $\binom{N}{k} = \binom{7}{2} = 21$ switches to 21 different combinations of two PMTs; and the remaining 12 switches to 12 combinations of three PMTs [i.e., $\binom{N}{k} = \binom{7}{3} = 35 > 12$]. Table A.1 shows the PMT assignments for the 40 switches on MAIZE. Note that the total number of fibers is dependent on the number of switches in the LTD, the number of PMTs used to monitor the switches, and how the PMTs are assigned to the switches. This number can grow rapidly, and meticulous cable management becomes a necessity. Additional analysis of this issue is presented in Sec. A.4.

We used roughly 18 m of 1-mm-diameter step-indexed multimode fiber optic cable to couple each switch to its respective combination of PMTs. The fibers were attached to the switches using

3D-printed fiber holders, where each holder had an elongated support structure, which was fitted into a feedthrough port in the spark-gap switch's dielectric housing. These holders also provide fiber strain relief, which reduces the chances of a fiber breaking. This is useful because the setup does not detect damaged fibers. For switches that are assigned to multiple PMTs, we used a dedicated fiber for each switch-PMT connection. This means that each switch had one, two, or three fibers residing in its feedthrough port, which required running 85 fibers in total from the MAIZE LTD cavity to the PMT box in the MAIZE screen room. The PMTs were housed within a light-tight Faraday cage to minimize electromagnetic interference from potential noise sources.

The system is triggered by the first switch that fires. This is done so that the oscilloscopes can be set to record waveforms with nanosecond resolution while also continually monitoring for pre-firing switches during the charging of the LTD, which can take several tens of seconds. To enable this triggering scheme, we split the output of each of the seven PMTs into two lines (see Fig. A.2). One of the lines connects to the input of an oscilloscope channel, while the other line connects to one of the inputs of an eight-channel adder (of which we only used seven channels). We used a 1N4148 diode between the PMT outputs and the adder inputs to isolate the PMT outputs from each other (i.e., without the diodes, the PMT outputs are shorted together in the adder circuit). The 1N4148 diode was selected because of its sufficiently low forward bias voltage (allowing signals to propagate relatively unimpeded in the forward direction) and because of its sufficiently large backwards bias voltage (isolating the PMT outputs from each other). We then split the adder output into two trigger signals, one for each four-channel oscilloscope.

A.3 Results on the MAIZE Facility and Potential Future Improvements

The diagnostic configuration described in Sec. A.2 is now routinely used on MAIZE to identify both single pre-firing and single late-firing switches, while using only seven PMT-oscilloscope channels (see Fig. A.3). In Fig. A.3 (top), we present the case where all of the switches fire synchronously, thus all of the PMTs turn on at the same time, which indicates proper firing of the LTD. By contrast, in Fig. A.3 (bottom), we present the case where switch '27' pre-fires, which, in accordance with Table A.1, is indicated by PMTs '5' and '7' turning on before the others. For the results presented above, the switches were filled to 95 psig with "Ultra Zero Grade" dry air, the bricks were charged to $\pm$70 kV, and the load was a short-circuit metal rod.

While this diagnostic scheme works as intended for identifying single switches firing early or very late relative to the rest of the switches, our present implementation has trouble distinguishing which switches closed first when multiple switches pre-fire or late-fire at nearly the same time.

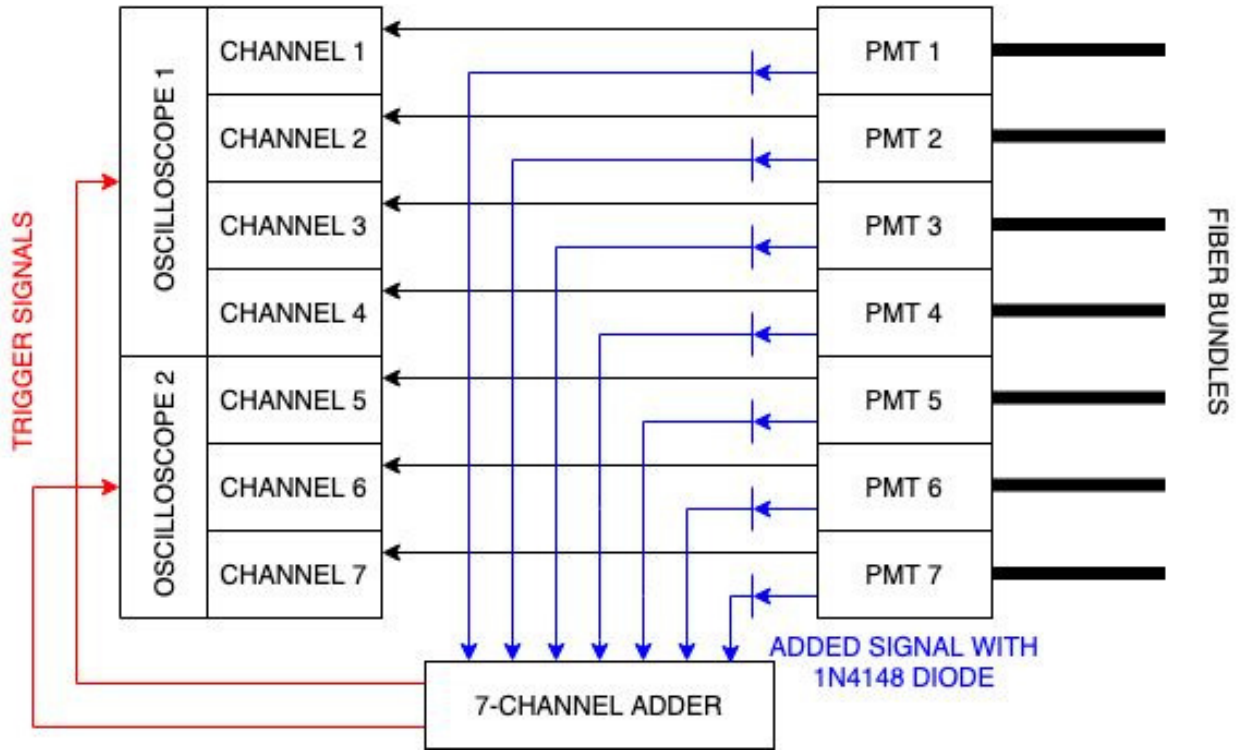

Figure A.2: A schematic of the experimental setup to monitor the 40 switches on MAIZE.

For example, switches '5' and '7' pre-firing at the same time would result in a graph similar to Fig. A.3 (bottom). Thus, time resolution is important, including both the oscilloscope sampling rate and the PMT detector response. With sufficient time resolution (sub-ns), identifying the first switch to pre-fire should still be possible, as it is very unlikely that multiple switches pre-fire at *exactly* the same time during a relatively long charging sequence (which occurs over many tens of seconds on MAIZE). Additionally, monitoring *calibrated* PMT output amplitudes should allow us to distinguish between a single switch pre-firing (lower PMT output amplitudes) and multiple switches pre-firing at the same time (higher PMT output amplitudes). This would also allow us to identify problematic non-firing switches. Such a diagnostic scheme could be simplified by digitizing the light output from the switches (e.g., using inexpensive photodiodes) instead of relying on calibrated PMTs. We also note that implementing the resistor ladder technique mentioned in Sec. A.1 could help to resolve issues with multiple switches pre-firing at the same time.

The fiber-based techniques described in this paper could give false-positive results for pre-firing switches if a significant amount of light is collected by the fibers from sources other than the switches (e.g., from oil arcs). These issues can be mitigated by shielding and collimating the fibers such that they collect light only from the switches. We intend to implement better shielding and collimation in future implementations on MAIZE. Another potential improvement for this diagnostic is the development of machine learning tools. These tools would be trained on known

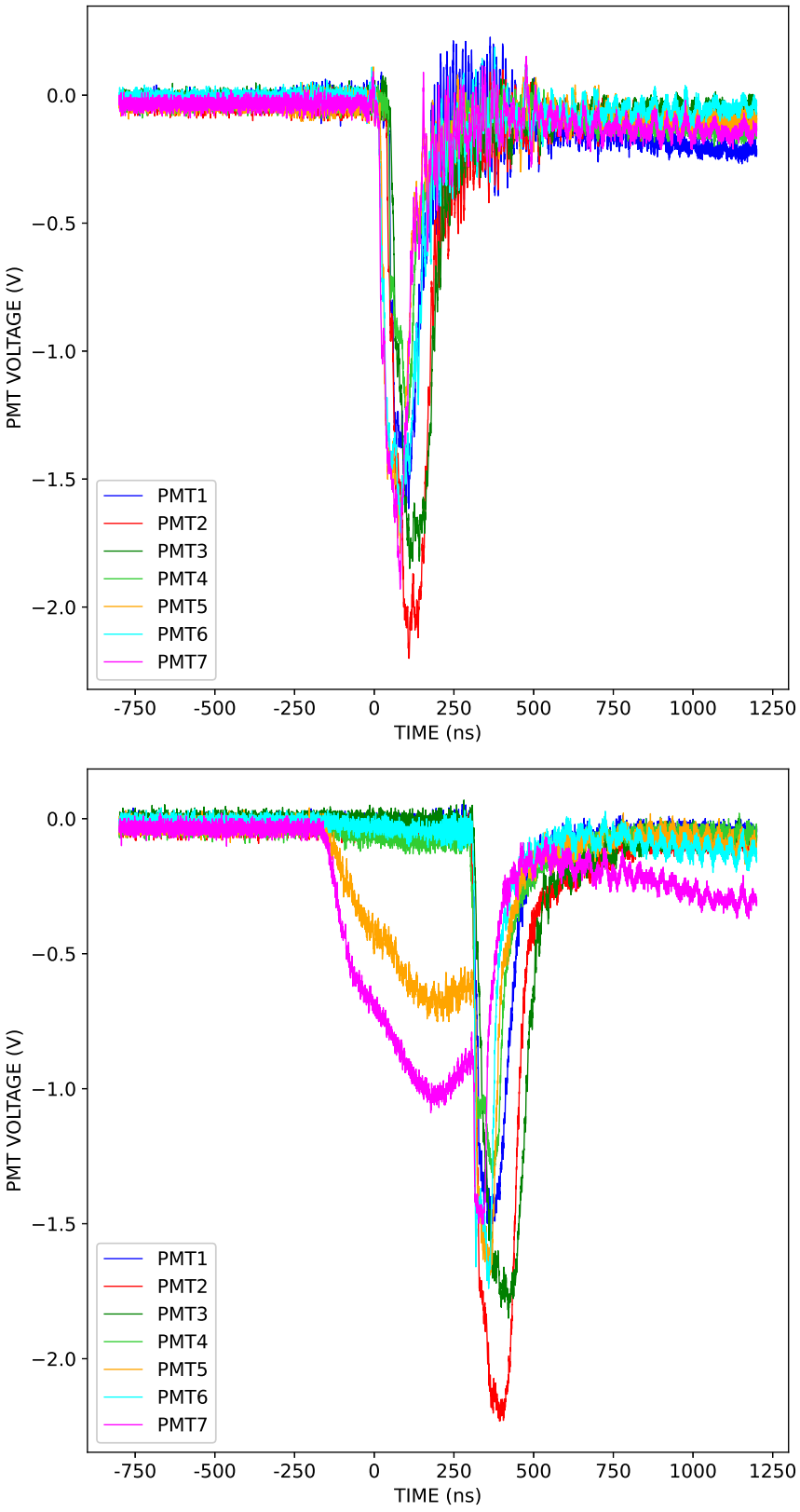

Figure A.3: Top: ideal functioning of MAIZE where all 40 switches fire at the same time. Bottom: a pre-fire in switch '27', as indicated by the early signal received by PMTs '5' and '7', which correspond to the combination of PMTs assigned to switch '27' (*cf.* Table A.1).

data sets and could be used to differentiate between single misfiring switches, multiple misfiring switches, and spurious signals (e.g., oil arcs). Such tools would be particularly useful for implementing this diagnostic on large-scale facilities, where tens of thousands of switches may need to be monitored.

A.4 Scaling Switch Monitoring Solutions to Large Pulsed Power Facilities

The diagnostic technique presented in this paper allows for monitoring of X switches by $< X$ PMT-oscilloscope channels. One trade-off in reducing the number of PMT-oscilloscope channels to $< X$ is that the total number of optical fibers that must be routed in the system grows to a number $> X$.

In Fig. A.4, we illustrate how the total number of required fibers scales with the number of switches monitored and the number of PMT-oscilloscope channels used. The straight diagonal blue line represents both the number of PMT-oscilloscope channels and the total number of fibers needed when every switch is monitored using an independent fiber-PMT-oscilloscope channel (a 1:1 monitoring scheme). By contrast, the red line is a plot of Eqn. A.2, which represents a system using the minimum number of PMT-oscilloscope channels. Note that the red line is the lower bound and the blue line is the upper bound for the overall solution space shaded in red, which represents the range in the number of PMT-oscilloscope channels that could be used to monitor a given number of switches, X. Each point in the lower shaded region (red) corresponds to a point in the upper shaded region (green). The green shaded region represents the range in the total number of optical fibers required to monitor X switches. Note that the upper bound for the green region (the green line) corresponds to the lower bound for the red region (the red line). Also note that, to our knowledge, there is no simple analytic function for calculating the fiber scaling represented by the green line. Thus, we wrote a simple computer algorithm to automate the fiber counting and generate the plot (see Sec. A.5).

In analyzing Fig. A.4, a useful heuristic is to recognize that the closer the system is to the red line, the closer it will be to the green line. Similarly, the further the system is from the red line, the further it will be from the green line, until the solutions in the upper and lower shaded regions ultimately converge on the 1:1 monitoring scheme represented by the straight diagonal blue line. This illustrates the trade-off whereby using fewer PMT-oscilloscope channels requires a greater total number of fibers to be routed in the system. For example, the minimum number of PMTs required to monitor the 40 switches on MAIZE is six, as calculated by Eqn. A.2. Using this solution would require a total of 93 fibers to be run into the LTD cavity. In Fig. A.4, for the case of $X = 40$

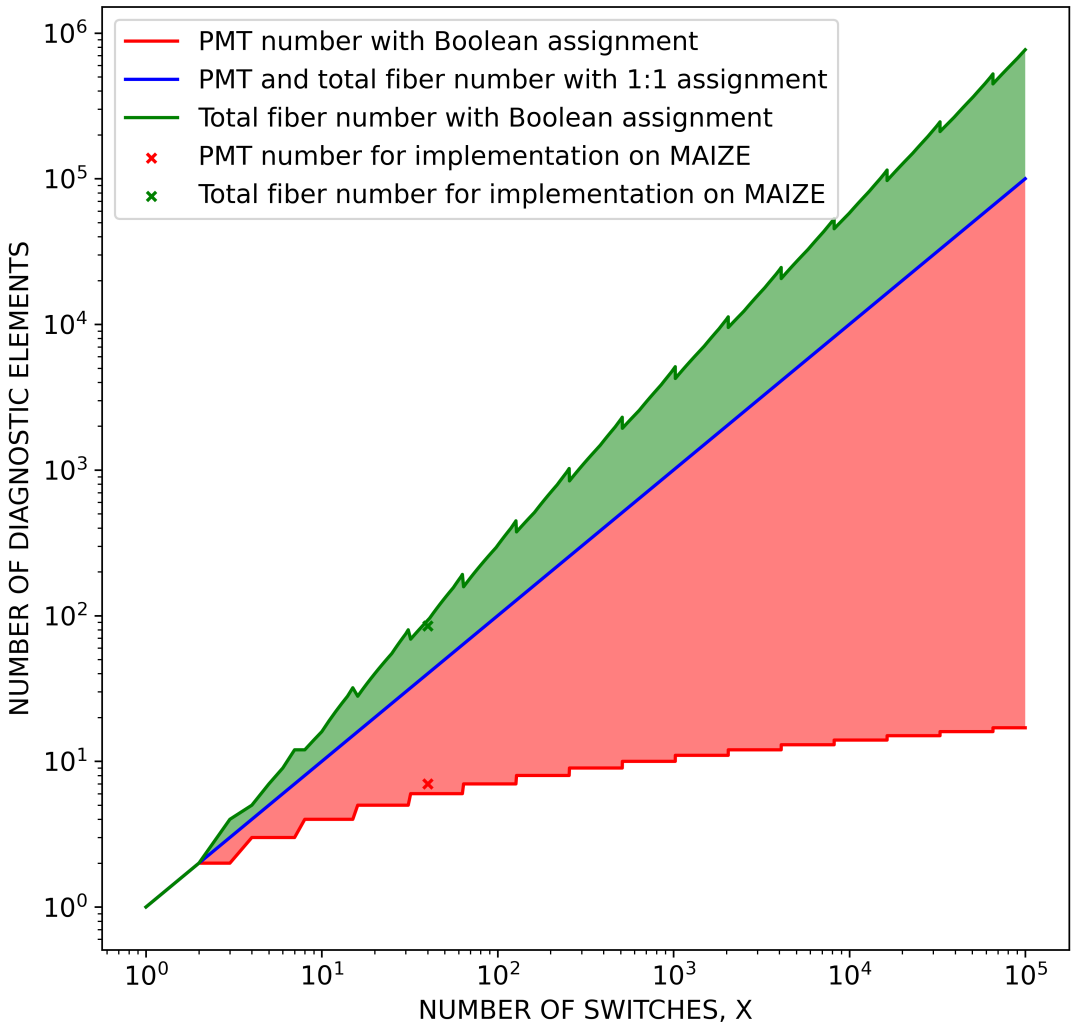

Figure A.4: The solution space for the number of PMT-oscilloscope channels needed and the total number of fibers needed as a function of the number of spark-gap switches to be monitored. The lower bound for the red shaded region (the red line) is given by Eq. 2, which represents the minimum number of PMT-oscilloscope channels needed for monitoring X switches. This solution requires the maximum number of fibers, which is indicated by the green line (the upper bound of the green shaded region). The red and green shaded regions represent intermediate solutions, where extra PMT-oscilloscope channels are employed in order to use fewer fibers. The red and green solution spaces converge on each other at the straight diagonal blue line, which represents a 1:1 monitoring scheme, where every switch is monitored by a dedicated fiber-PMT-oscilloscope channel (i.e., the number of fibers used equals the number of PMT-oscilloscope channels used, which equals the number of switches monitored).

switches, the points corresponding to six PMT-oscilloscope channels and 93 fibers lie on the red and green lines, respectively. In our implementation on MAIZE, however, we chose to use seven PMTs instead of six, which then required only 85 fibers total. In Fig. A.4, and again for the case of $X = 40$ switches, the points corresponding to seven PMT-oscilloscope channels and 85 fibers lie in the red and green shaded areas, respectively. If we continued adding more PMT-oscilloscope channels to the system, then the total number of fibers required would continue to decrease until the system eventually converged on the 1:1 scheme, where $X = 40$ switches requires 40 PMT-oscilloscope channels and 40 fibers in total. Indeed, researchers working at large pulsed power facilities might not necessarily want to use the minimum number of PMT-oscilloscope channels; instead, they may want to use more PMT-oscilloscope channels to gain the advantage of using fewer fiber optic cables. Finding a suitable compromise between the number of PMTs used and the number of fibers used depends on the goals of the facility and on the resources available at the facility.

The switch monitoring diagnostic presented here could be useful for next generation pulsed power facilities, where the number of switches to be monitored may be large. For example, some candidate architectures for replacing today's Z facility at Sandia National Laboratories include LTD-based designs with approximately 100,000 switches [64]. Referring to the solution space available for $X = 100{,}000$ switches in Fig. A.4, the diagnostic elements needed range from 17 PMT-oscilloscope channels and 768,001 fiber optic cables (with a Boolean scheme) to 100,000 PMT-oscilloscope channels and 100,000 fiber optic cables (with a 1:1 scheme). The diagnostic technique presented in this paper could significantly reduce the resources needed by finding a solution that uses a suitable number of PMT-oscilloscope channels along with a suitable number of fibers.

A.5 switch_diagnostics_counter.py

```
from numpy import ceil
from math import log
from scipy.special import binom
import matplotlib.pyplot as plt

x = range(1,pow(10,5),1)
y_1_1 = [i for i in x]
y_pmt = [ceil(log(i+1,2)) for i in x]

def tot_fibers(x):          # x is the number of switches
```

```
    n = ceil(log(x+1,2))  # n is the number of PMTs
    i = 0
    j = 0
    for y in range(1,int(n)+1,1):
        for z in range(1,int(binom(n,y))+1,1):
            if i > x-1:
                break
            i = i+1
            j = j + y
    return(j)

tots = [tot_fibers(A) for A in x]

font = {'size':12}
plt.rc('font', **font)
plt.loglog(x, y_pmt, 'r', label='PMT number with Boolean
 ↪  assignment')
plt.loglog(x, y_1_1, 'b', label='PMT and total fiber number
 ↪  with 1:1 assignment')
plt.loglog(x, tots, 'g', label='Total fiber number with Boolean
 ↪  assignment')
plt.fill_between(x, y_pmt, y_1_1, facecolor='r', alpha=0.5)
plt.fill_between(x, y_1_1, tots, facecolor='g', alpha=0.5)
plt.scatter(40, 7, s=18, marker='x', color='red', label='PMT
 ↪  number for implementation on MAIZE')
plt.scatter(40, 85, s=18, marker='x', color='green',
 ↪  label='Total fiber number for implementation on MAIZE')
plt.xlabel('NUMBER OF SWITCHES, X')
plt.ylabel('NUMBER OF DIAGNOSTIC ELEMENTS')
font = {'size':8}
plt.rc('font', **font)
plt.legend(loc=2)
plt.savefig('theoretical_plots.eps', dpi=600)

```

APPENDIX B

Thin-Shell Implosion Models

B.1 current_driven.py

```
import numpy as np
from numpy import pi, sin, floor, zeros
from scipy import integrate
import matplotlib.pyplot as plt

######## INNER SHELL EXPERIMENT

mu = 4*pi*pow(10,-7)
r_inner_2 = 0.01            # Shell Outer Radius (m)
r_inner_1 = 0.009           # Shell Inner Radius (m)
de_inner = 0.014            # Liner Density (kg/m**3)
t_peak = 200E-9             # Peak rise time (s)
w = pi/(2*t_peak)           # Frequency (1/s)
i_peak = 5.0E5              # Peak current (A)

m=de_inner*pi*(r_inner_2**2-r_inner_1**2)

def area(r):
    return 2*pi*r

def Inner_Shell_Implosion(t, R):
    dR_dt = zeros((2,1))
    dR_dt[0] = R[1]
```

```
24      dR_dt[1] = (area(R[0])/m) * (-mu/(8*pow(pi,2)*pow(R[0],2)))
        ↪  * pow(i_peak*sin(w*t),2)
25      return[dR_dt]
26
27  #set timestep size and length of time the ode solver will run
28  t_start = 0.0
29  t_final = 3*t_peak
30  delta_t = 1E-10
31  num_steps = int(floor((t_final - t_start)/delta_t) + 1)
32
33  sol_inner_shell_implosion =
    ↪  integrate.ode(Inner_Shell_Implosion).set_integrator(
    ↪  'dopri5', method='bdf')
34  sol_inner_shell_implosion.set_initial_value([r_inner_2, 0.0],
    ↪  t_start)
35
36  #set initial conditions
37  t_inner = zeros((num_steps, 1))
38  t_inner[0] = t_start
39  r_inner = zeros((num_steps, 1))
40  v_inner = zeros((num_steps, 1))
41  r_inner[0] = r_inner_2
42  v_inner[0] = 0.0
43
44  k = 1
45
46  while sol_inner_shell_implosion.successful() and k < num_steps:
47      sol_inner_shell_implosion.integrate
        ↪  (sol_inner_shell_implosion.t + delta_t)
48      t_inner[k] = sol_inner_shell_implosion.t
49      r_inner[k] = sol_inner_shell_implosion.y[0]
50      v_inner[k] = sol_inner_shell_implosion.y[1]
51      if r_inner[k] < 0.1*r_inner_2:
52          break
53      k += 1
54
```

```
55 ######## OUTER SHELL EXPERIMENT
56
57 mu = 4*pi*pow(10,-7)
58 r_outer_2 = 0.022           # Shell Outer Radius (m)
59 r_outer_1 = 0.020           # Shell Inner Radius (m)
60 de_outer = 0.00044          # Liner Density (kg/m**3)
61 t_peak = 200E-9             # Peak rise time (s)
62 w = pi/(2*t_peak)           # Frequency (1/s)
63 i_peak = 5.0E5              # Peak current (A)
64
65 m=de_outer*pi*(r_outer_2**2-r_outer_1**2)
66
67 def area(r):
68     return 2*pi*r
69
70 def Outer_Shell_Implosion(t, R):
71     dR_dt = zeros((2,1))
72     dR_dt[0] = R[1]
73     dR_dt[1] = (area(R[0])/m) * (-mu/(8*pow(pi,2)*pow(R[0],2)))
       ↪  * pow(i_peak*sin(w*t),2)
74     return[dR_dt]
75
76 #set timestep size and length of time the ode solver will run
77 t_start = 0.0
78 t_final = 3*t_peak
79 delta_t = 1E-10
80 num_steps = int(floor((t_final - t_start)/delta_t) + 1)
81
82 sol_outer_shell_implosion =
   ↪  integrate.ode(Outer_Shell_Implosion).set_integrator(
   ↪  'dopri5', method='bdf')
83 sol_outer_shell_implosion.set_initial_value([r_outer_2, 0.0],
   ↪  t_start)
84
85 #set initial conditions
86 t_outer = zeros((num_steps, 1))
```

```
t_outer[0] = t_start
r_outer = zeros((num_steps, 1))
v_outer = zeros((num_steps, 1))
r_outer[0] = r_outer_2
v_outer[0] = 0.0

k = 1

while sol_outer_shell_implosion.successful() and k < num_steps:
    sol_outer_shell_implosion.integrate
     ↪  (sol_outer_shell_implosion.t + delta_t)
    t_outer[k] = sol_outer_shell_implosion.t
    r_outer[k] = sol_outer_shell_implosion.y[0]
    v_outer[k] = sol_outer_shell_implosion.y[1]
    if r_outer[k] < 0.1*r_outer_2:
        break
    k += 1

#scale values
ts_inner = t_inner*1E9
rs_inner = r_inner[r_inner != 0.0]
ts_inner = ts_inner[:len(rs_inner)]
ts_outer = t_outer*1E9
rs_outer = r_outer[r_outer != 0.0]
ts_outer = ts_outer[:len(rs_outer)]
i_t = np.linspace(0, 1.5*t_peak, num_steps)
i = i_peak*sin(w*i_t)

##############
##############

font = {'size':12}
plt.rc('font', **font)

plt.rcParams["figure.figsize"] = (8,8)
xs2 = np.linspace(0, 2*t_peak, num_steps)
```

```
122 fig, ax1 = plt.subplots()
123 ts_inner = [i*1e-9 for i in ts_inner]
124 ts_outer = [i*1e-9 for i in ts_outer]
125 plot_1 = ax1.plot(ts_inner, rs_inner, 'k', label='Inner Shell
    ↪ Liner', linestyle = 'dashdot')
126 plot_2 = ax1.plot(ts_outer, rs_outer, 'k', label='Outer Shell
    ↪ Liner')
127 ax1.ticklabel_format(axis='y', style='sci', scilimits=(-2,-2))
128 ax1.ticklabel_format(axis='x', style='sci', scilimits=(-9,-9))
129 ax1.set_ylim([0,0.025])
130 ax1.set_xlabel('TIME (s)')
131 ax1.set_ylabel('LINER RADIUS (m)', color='k')
132 ax1.tick_params('y', colors='k')
133 ax1.tick_params('x', colors='k')
134 ax2 = ax1.twinx()
135 plot_3 = ax2.plot(i_t, i, 'b', label='Current')
136 plots = plot_1 + plot_2 + plot_3
137 labels = [i.get_label() for i in plots]
138 ax1.legend(plots, labels)
139 ax2.ticklabel_format(axis='y', style='sci', scilimits=(3,3))
140 ax2.set_ylabel('CURRENT (A)', color='b')
141 ax2.set_ylim([0,1e6])
142 ax2.tick_params('y', colors='b')
143 plt.xlim([0,250e-9])
144 plt.savefig('current_driven_thin-shell_model.eps', dpi = 600,
    ↪ bbox_inches='tight')
145 plt.show()
146
```

B.2 voltage_driven.py

```
1
2 import numpy as np
3 from numpy import pi, log
4 from scipy import integrate
5 import matplotlib.pyplot as plt
```

```
6
7  ######## INNER SHELL EXPERIMENT
8
9  mu = 4*pi*pow(10,-7)
10 C = 0.8e-6                  # Capacitance (Farads)
11 L_0 = 15e-9                 # Inductance (Henries)
12 vc = 2*(60*pow(10,3))       # Voltage (Volts)
13 r_outer = 0.010             # Shell Outer Radius (m)
14 r_inner = 0.009             # Shell Inner Radius (m)
15 r_rc = 0.052                # Return Current Radius (m)
16 de_outer = 0.014            # Liner Density (kg/m**3)
17 h = 0.020                   # Height (m)
18 t_peak = 200E-9             # Peak rise time (s)
19 w = pi/(2*t_peak)           # Frequency (1/s)
20 Rloss = 0.2                 # Resistance (Ohms)
21
22 m=de_outer*pi*h*(r_outer**2-r_inner**2)
23
24 def f(t,y):
25     r,v,I,phi = y
26     dydt = np.zeros((2,1))
27     dydt[0] = v
28     dydt[1] = -(mu*h*pow(I,2))/(4*pi*m*r)
29     Lvac = (mu*h/(2*pi))*(log(r_rc/r))
30     Lvac_dot = -(mu*h/(2*pi))*v/r
31     dIdt = (phi-I*(Lvac_dot))/(L_0+ Lvac)
32     dphidt = (-I-phi/Rloss)/C
33     return[dydt[0], dydt[1], dIdt, dphidt]
34
35 sol = integrate.ode(f).set_integrator('dopri5', method='bdf')
36
37 #set timestep size and length of time the ode solver will run
38 t_start = 0.0
39 t_final = 3*t_peak
40 delta_t = 1E-10
41 num_steps = int(np.floor((t_final - t_start)/delta_t) + 1)
```

```
42
43 #set initial conditions
44 i_0 = 0
45 v_0 = 0
46 sol.set_initial_value([r_outer, v_0, i_0, vc])
47
48 t = [t_start]
49 i = [i_0]
50 r_out = [r_outer]
51 v_out = [v_0]
52 voltage = [vc]
53
54 k = 1
55
56 while sol.successful() and k < num_steps:
57     sol.integrate(sol.t + delta_t)
58     t.append(sol.t)
59     r_out.append(sol.y[0])
60     v_out.append(sol.y[1])
61     i.append(sol.y[2])
62     voltage.append(sol.y[3])
63     k += 1
64     if sol.y[0] < r_outer/10:
65         break
66
67 #scale values
68 ts_inner = [x*1e9 for x in t]
69 rs_inner = [x for x in r_out]
70 i_s_inner = [x for x in i]
71 voltage_s_inner = [x/1e6 for x in voltage]
72
73 ######## OUTER SHELL EXPERIMENT
74
75 mu = 4*pi*pow(10,-7)
76 C = 0.8e-6                  # Capacitance (Farads)
77 L_0 = 15e-9                 # Inductance (Henries)
```

```
78  vc = 2*(60*pow(10,3))       # Voltage (Volts)
79  r_outer = 0.022             # Shell Outer Radius (m)
80  r_inner = 0.020             # Shell Inner Radius (m)
81  r_rc = 0.052                # Return Current Radius (m)
82  de_outer = 0.00044          # Liner Density (kg/m**3)
83  h = 0.020                   # Height (m)
84  t_peak = 200E-9             # Peak rise time (s)
85  w = pi/(2*t_peak)           # Frequency (1/s)
86  Rloss = 0.2                 # Resistance (Ohms)
87
88  m=de_outer*pi*h*(r_outer**2-r_inner**2)
89
90  def f(t,y):
91      r,v,I,phi = y
92      dydt = np.zeros((2,1))
93      dydt[0] = v
94      dydt[1] = -(mu*h*pow(I,2))/(4*pi*m*r)
95      Lvac = (mu*h/(2*pi))*(log(r_rc/r))
96      Lvac_dot = -(mu*h/(2*pi))*v/r
97      dIdt = (phi-I*(Lvac_dot))/(L_0+ Lvac)
98      dphidt = (-I-phi/Rloss)/C
99      return[dydt[0], dydt[1], dIdt, dphidt]
100
101 sol = integrate.ode(f).set_integrator('dopri5', method='bdf')
102
103 #set timestep size and length of time the ode solver will run
104 t_start = 0.0
105 t_final = 3*t_peak
106 delta_t = 1E-10
107 num_steps = int(np.floor((t_final - t_start)/delta_t) + 1)
108
109 #set initial conditions
110 i_0 = 0
111 v_0 = 0
112 sol.set_initial_value([r_outer, v_0, i_0, vc])
113
```

```
114 t = [t_start]
115 i = [i_0]
116 r_out = [r_outer]
117 v_out = [v_0]
118 voltage = [vc]
119
120 k = 1
121
122 while sol.successful() and k < num_steps:
123     sol.integrate(sol.t + delta_t)
124     t.append(sol.t)
125     r_out.append(sol.y[0])
126     v_out.append(sol.y[1])
127     i.append(sol.y[2])
128     voltage.append(sol.y[3])
129     k += 1
130     if sol.y[0] < r_outer/10:
131         break
132
133 #scale values
134 ts_outer = [x*1e9 for x in t]
135 rs_outer = [x for x in r_out]
136 i_s_outer = [x for x in i]
137 voltage_s_outer = [x/1e6 for x in voltage]
138
139 ##############
140 ##############
141
142 font = {'size':12}
143 plt.rc('font', **font)
144
145 plt.rcParams["figure.figsize"] = (8,8)
146 xs2 = np.linspace(0, 2*t_peak, num_steps)
147 fig, ax1 = plt.subplots()
148 ts_inner = [i*1e-9 for i in ts_inner]
149 ts_outer = [i*1e-9 for i in ts_outer]
```

```
150 plot_1 = ax1.plot(ts_inner, rs_inner, 'k', label='Inner Shell
    ↪ Liner', linestyle = 'dashdot')
151 plot_2 = ax1.plot(ts_outer, rs_outer, 'k', label='Outer Shell
    ↪ Liner')
152 ax1.ticklabel_format(axis='y', style='sci', scilimits=(-2,-2))
153 ax1.ticklabel_format(axis='x', style='sci', scilimits=(-9,-9))
154 ax1.set_ylim([0,0.025])
155 ax1.set_xlabel('TIME (s)')
156 ax1.set_ylabel('LINER RADIUS (m)', color='k')
157 ax1.tick_params('y', colors='k')
158 ax1.tick_params('x', colors='k')
159 ax2 = ax1.twinx()
160 plot_3 = ax2.plot(ts_inner, i_s_inner, 'b', label='Inner Shell
    ↪ Current', linestyle = 'dashdot')
161 plot_4 = ax2.plot(ts_outer, i_s_outer, 'b', label='Outer Shell
    ↪ Current')
162 plots = plot_1 + plot_2 + plot_3 + plot_4
163 labels = [i.get_label() for i in plots]
164 ax1.legend(plots, labels)
165 ax2.ticklabel_format(axis='y', style='sci', scilimits=(3,3))
166 ax2.set_ylabel('CURRENT (A)', color='b')
167 ax2.set_ylim([0,1e6])
168 ax2.tick_params('y', colors='b')
169 plt.xlim([0,250e-9])
170 plt.savefig('voltage_driven_thin-shell_model.eps', dpi = 600,
    ↪ bbox_inches='tight')
171 plt.show()
172
```

APPENDIX C

Transmission Line Inductance

C.1 Coaxial Transmission Line Inductance Theory

High-power magnetically insulated transmission lines (MITLs) like those found on MAIZE, which are primarily radial but include some axial translation, have a minimum inductance when they have a curved profile, which can be approximated by a straight cone for ease of manufacturing. A conical transmission line can be thought of as an integral of infinitesimally short coaxial transmission lines. The inductance of a coaxial transmission line is given by

$$L = \frac{\mu_0 h}{2\pi} \ln\left(\frac{r_{\text{out}}}{r_{\text{in}}}\right) \tag{C.1}$$

where r_{out} and r_{in} are the outer and inner radii of the coaxial line, respectively. The infinitesimal inductance of an infinitesimally short coaxial line is given by

$$dL = \frac{\mu_0}{2\pi} \ln\left(\frac{r_{\text{out}}}{r_{\text{in}}}\right) dh \tag{C.2}$$

where dh is the infinitesimally short length (or height) of the coaxial transmission line at position (or height) h. Numerically integrating Eq. C.2 for a given geometry, where r_{out} and r_{in} are defined for a given h gives the total inductance of the transmission line.

C.2 co-axial_t-line_inductance.py

```
1 import numpy as np
2 import matplotlib.pyplot as plt
3 from numpy import pi, log
4
5 mu_0 = 4E-7*pi
```

```
C = mu_0/(2*pi)

domain = np.arange(0,330001,1)
domain = [-i/1000 for i in domain]
domain = domain[::-1]
ranger = np.arange(0,102688,1)
ranger = [i/1000 for i in ranger]

# Define the 2-stage A-K gap

def ranger_pre_A(x):
    return (0.697459*x)+114.302

def domainer_pre_A(y):
    return (y-114.302)/0.697459

def ranger_A(x):
    return (1.07674*x)+159.16

def domainer_A(y):
    return (y-159.16)/1.07674

def ranger_pre_K(x):
    return (0.697443*x)+97.596

def domainer_pre_K(y):
    return (y-97.596)/0.697443

def ranger_K(x):
    return (1.07675*x)+139.022

def domainer_K(y):
    return (y-139.022)/1.07675

pre_A_domain = domain[0:330000-144240]
pre_A_ranger = [ranger[13701] for i in pre_A_domain]
```

```
42
43 pre_K_domain = domain[0:330000-139934]
44 pre_K_ranger = [ranger[0] for i in pre_K_domain]
45
46 K_ranger_1 = ranger[0:13701]
47 K_domain_1 = [domainer_pre_K(i) for i in K_ranger_1]
48
49 K_ranger_2 = ranger[13701:21415]
50 K_domain_2 = [domainer_pre_K(i) for i in K_ranger_2]
51
52 A_ranger_2 = ranger[13701:21415]
53 A_domain_2 = [domainer_pre_A(i) for i in A_ranger_2]
54
55 K_ranger_3 = ranger[21415:31814]
56 K_domain_3 = [domainer_K(i) for i in K_ranger_3]
57
58 A_ranger_3 = ranger[21415:31814]
59 A_domain_3 = [domainer_pre_A(i) for i in A_ranger_3]
60
61 A_ranger_4 = ranger[31814:102688]
62 A_domain_4 = [domainer_A(i) for i in A_ranger_4]
63
64 K_ranger_4 = ranger[31814:102688]
65 K_domain_4 = [domainer_K(i) for i in K_ranger_4]
66
67 ##############
68
69 # Define the inductance function
70
71 def dL(r_o, r_i, dz):
72     return C*log(r_o/r_i)*dz
73
74 i = 1
75 L = 0
76
77 while i < 13701:
```

```
78      L = L + dL(-0.33, K_domain_1[i]*pow(10,-3),
        ↪  (K_ranger_1[i]-K_ranger_1[i-1])*pow(10,-3))
79      i = i + 1
80
81  i = 1
82
83  while i < 7714:
84      L = L + dL(A_domain_2[i]*pow(10,-3),
        ↪  K_domain_2[i]*pow(10,-3),
        ↪  (K_ranger_2[i]-K_ranger_2[i-1])*pow(10,-3))
85      i = i + 1
86
87  i = 1
88
89  while i < 10399:
90      L = L + dL(A_domain_3[i]*pow(10,-3),
        ↪  K_domain_3[i]*pow(10,-3),
        ↪  (K_ranger_3[i]-K_ranger_3[i-1])*pow(10,-3))
91      i = i + 1
92
93  i = 1
94
95  while i < 70874:
96      L = L + dL(A_domain_4[i]*pow(10,-3),
        ↪  K_domain_4[i]*pow(10,-3),
        ↪  (K_ranger_4[i]-K_ranger_4[i-1])*pow(10,-3))
97      i = i + 1
98
99  ##############
100
101 font = {'size':12}
102 plt.rc('font', **font)
103 #plt.rcParams["figure.figsize"] = (8,8)
104 fig, ax1 = plt.subplots()
105 ax1.set_xlim([-340, 0])
106 ax1.set_ylim([-50, 150])
```

```
107 ax1.set_aspect('equal')
108 ax1.set_xlabel('R (mm)')
109 ax1.set_ylabel('Z (mm)')
110 plot_1 = ax1.plot(pre_A_domain, pre_A_ranger, label='Anode',
    ↪ color='b')
111 plot_2 = ax1.plot(pre_K_domain, pre_K_ranger, label='Cathode',
    ↪ color='r')
112 plot_3 = ax1.plot(K_domain_1, K_ranger_1, color='r')
113 plot_4 = ax1.plot(K_domain_2, K_ranger_2, color='r')
114 plot_5 = ax1.plot(A_domain_2, A_ranger_2, color='b')
115 plot_6 = ax1.plot(K_domain_3, K_ranger_3, color='r')
116 plot_7 = ax1.plot(A_domain_3, A_ranger_3, color='b')
117 plot_8 = ax1.plot(A_domain_4, A_ranger_4, color='b')
118 plot_9 = ax1.plot(K_domain_4, K_ranger_4, color='r')
119 plots = plot_1 + plot_2 + plot_3 + plot_4 + plot_5 + plot_6 +
    ↪ plot_7 + plot_8
120 labels = [i.get_label() for i in plots]
121 ax1.legend(plots, labels)
122 plt.savefig('MITL_Inductance.eps', dpi=600,
    ↪ bbox_inches='tight')
123
```

APPENDIX D

Interferometry Analysis

D.1 Interferometry Analysis Theory

Interference patterns carry density information of the medium in which the interfering light propagates, which can be retrieved by analysis. A brief workflow of how to retrieve this density information from the light intensity value per pixel in an image of the interference pattern is outlined here. An image is obtained of two interference patterns, one with no gas flowing and another with gas flowing in the target region. The interferometer should be oriented such that the direction of gas flow from the hardware is perpendicular to the fringes in the interference pattern. We can now refer to the interference fringes as oriented parallel to the rows and perpendicular to the columns of the pixel array that constitutes the image.

For each of the two images, a Fast Fourier Transform (FFT) is taken along each column to determine the principle frequency of the fringes. The FFT is cleaned up such that all frequencies less than a quarter of the principle (shot noise) and greater than double the principle are set to zero. The principle is shifted to zero and an inverse FFT taken to give a complex array, which is of the same orientation and dimension as the original array of pixels of the interference pattern. The phase at each pixel is calculated as the inverse arctangent of the ratio of the imaginary to real components of each array element. The phase difference for each array element is obtained by subtracting the array of the image with no gas flow from the image with gas flow. A column in this array of phase differences where there is no gas flow in the equivalent column in the original image is set to have a phase difference of zero. Each subsequent element along the row of each column is then tested to see if there a change in the phase difference greater than 2π (or less than -2π) between neighboring elements. If so, 2π is subtracted from (or added to) the neighboring element. The array of net phase can be multiplied by a constant, which is a function of the laser light properties and gas being probed to give an areal density (a 3D density line-integrated along the line-of-sight). The areal density can be inverse-Abel transformed by an *a priori* assumption of azimuthal symmetry in the target region being probed to give a 3D distribution of the gas-puff. A

sequence of characteristic images showing the raw interference pattern, net phase, areal density, and number density for an argon outer-shell are shown in Fig. D.1. A computer algorithm was developed to automate much of this process (see Sec. D.2).

D.2 interferometry_analysis.py

```
from PIL import Image as image
from PIL import ImageOps as imageops
import numpy as np
from scipy.fftpack import fftfreq, fft, ifft
import abel
import pandas as pd
from scipy.integrate import cumtrapz
from time import perf_counter

def image_upload(campaign, before_image_no, shot_image_no):
    im_before_raw = image.open(campaign + '/' +
    ↪  str(before_image_no) + '.tif')
    im_before_raw = imageops.grayscale(im_before_raw)
    im_puff_raw = image.open(campaign + '/' +
    ↪  str(shot_image_no) + '.tif')
    im_puff_raw = imageops.grayscale(im_puff_raw)
    return im_before_raw, im_puff_raw

def crop_image(campaign, before_image_no, shot_image_no):
    im_before_raw, im_puff_raw = image_upload(campaign,
    ↪  before_image_no, shot_image_no)
    im_before_crop = im_before_raw.crop((x1,y1,x2,y2))
    ar_before = np.fliplr(np.array(im_before_crop))
    im_puff_crop = im_puff_raw.crop((x1,y1,x2,y2))
    ar_puff = np.fliplr(np.array(im_puff_crop))
    return ar_before, ar_puff

def do_fourier_trans(ar):
    four_trans = []
    for i in range(0,x2-x1):
```

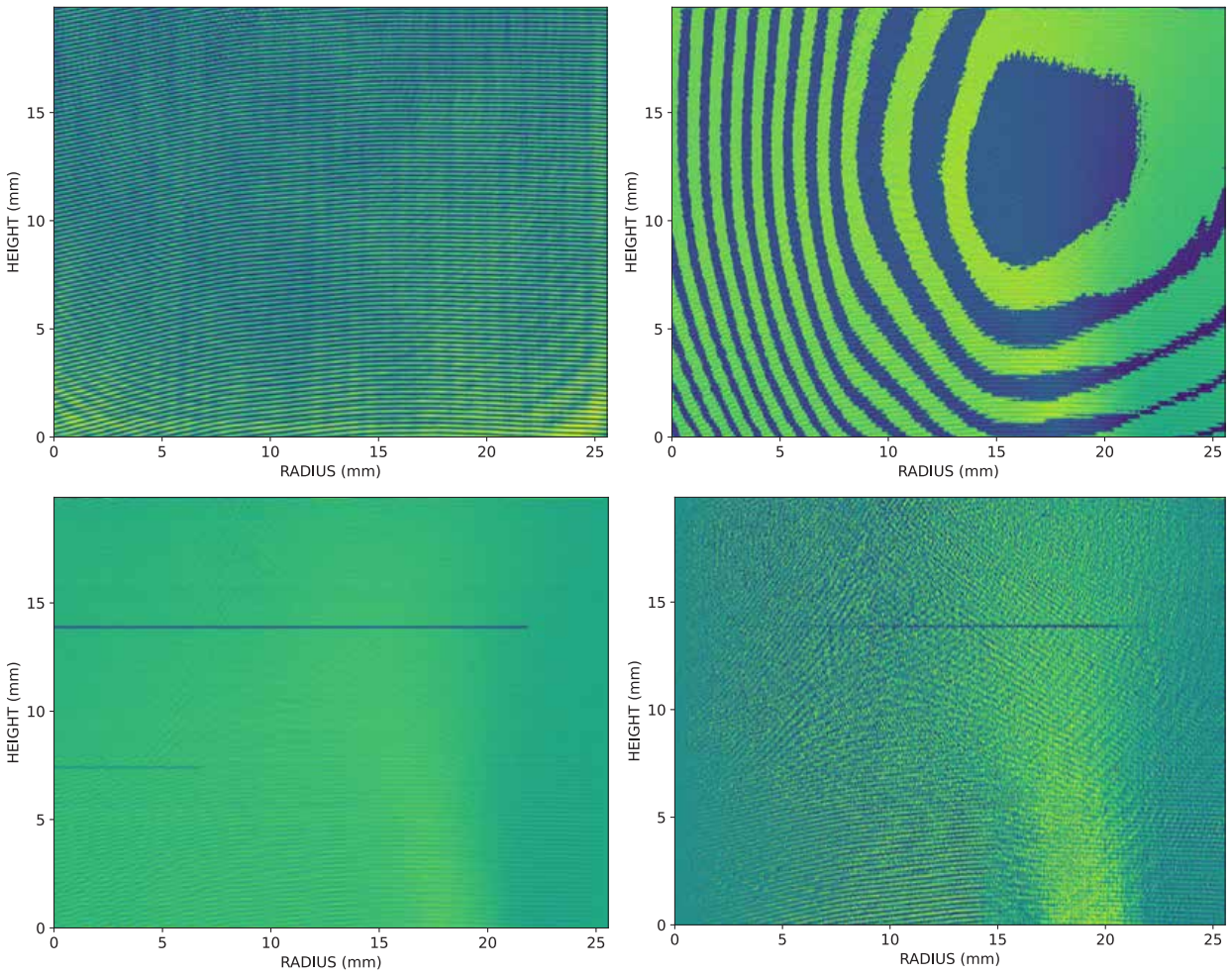

Figure D.1: The sequence of steps that are taken for interferometry analysis starting from the raw interference pattern (top-left) to the number density distribution (bottom-right). A raw interference pattern is acquired with gas flow in the target region and compared without gas flow to acquire a net phase image (top-right). A correction is made for neighboring pixels with a phase difference of greater or less than 2π and the entire array multiplied by a scalar to get an areal density (bottom-left). This is inverse-Abel inverted to get the three dimensional density distribution (bottom-right).

```
28          four_trans.append(fft(ar[:,i]))
29          four_trans[i][0] = 0
30      return four_trans
31
32  def four_trans(campaign, before_image_no, shot_image_no):
33      ar_before, ar_puff = crop_image(campaign, before_image_no,
        ↪  shot_image_no)
34      four_before = do_fourier_trans(ar_before)
35      four_puff = do_fourier_trans(ar_puff)
36      return four_before, four_puff
37
38  def do_process_params(lst):
39      power = np.abs(lst[0])**2
40      pos_mask = np.where(freqs >= 0)
41      pos_freqs = freqs[pos_mask]
42      max_idx = power[pos_mask].argmax()
43      max_freq = pos_freqs[max_idx]
44      return max_freq, max_idx
45
46  def process_signal(campaign, before_image_no, shot_image_no):
47      four_before, four_puff = four_trans(campaign,
        ↪  before_image_no, shot_image_no)
48      max_freq_before, max_idx_before =
        ↪  do_process_params(four_before)
49      max_freq_puff, max_idx_puff = do_process_params(four_puff)
50      processed_four_before, processed_four_puff =
        ↪  four_trans(campaign, before_image_no, shot_image_no)
51      for i in range(0,x2-x1):
52          processed_four_before[i][(freqs<max_freq_before/4)] = 0
53          processed_four_before[i][(freqs>max_freq_puff*1.9)] = 0
54          processed_four_before_left =
            ↪  processed_four_before[i][0:max_idx_before]
55          processed_four_before_right =
            ↪  processed_four_before[i][max_idx_before:y2-y1]
```

```
56          processed_four_before[i] =
             ↪  np.concatenate((processed_four_before_right,
             ↪  processed_four_before_left))
57          processed_four_puff[i][(freqs<max_freq_before/4)] = 0
58          processed_four_puff[i][(freqs>max_freq_puff*1.9)] = 0
59          processed_four_puff_left =
             ↪  processed_four_puff[i][0:max_idx_puff]
60          processed_four_puff_right =
             ↪  processed_four_puff[i][max_idx_puff:y2-y1]
61          processed_four_puff[i] =
             ↪  np.concatenate((processed_four_puff_right,
             ↪  processed_four_puff_left))
62      return processed_four_before, processed_four_puff
63
64  def do_ifour_trans(lst):
65      ifour_trans = []
66      for i in range(0,x2-x1):
67          ifour_trans.append(ifft(lst[i]))
68      return ifour_trans
69
70  def ifour_trans(campaign, before_image_no, shot_image_no):
71      processed_four_before, processed_four_puff =
         ↪  process_signal(campaign, before_image_no,
         ↪  shot_image_no)
72      ifour_before = do_ifour_trans(processed_four_before)
73      ifour_before = np.stack(ifour_before)
74      ifour_before = ifour_before.transpose()
75      ifour_puff = do_ifour_trans(processed_four_puff)
76      ifour_puff = np.stack(ifour_puff)
77      ifour_puff = ifour_puff.transpose()
78      return ifour_before, ifour_puff
79
80  def do_angles(ar):
81      phase = np.zeros((y2-y1,x2-x1))
82      phase = np.angle(ar)
83      return phase
```

```
84
85  def get_angles(campaign, before_image_no, shot_image_no):
86      ifour_before, ifour_puff = ifour_trans(campaign,
        ↪  before_image_no, shot_image_no)
87      phase_before = do_angles(ifour_before)
88      phase_puff = do_angles(ifour_puff)
89      return phase_before, phase_puff
90
91  def get_net_phase(campaign, before_image_no, shot_image_no):
92      phase_before, phase_puff = get_angles(campaign,
        ↪  before_image_no, shot_image_no)
93      net_phase = phase_puff - phase_before
94      #net_phase = phase_before - phase_puff
95      #net_phase[:,x2-x1-1] = 0
96      return net_phase
97
98  def do_smooth_y(ar):
99      delta = np.zeros((y2-y1,x2-x1))
100     steps = np.zeros((y2-y1,x2-x1))
101     clean = np.zeros((y2-y1,x2-x1))
102     for i in range(0,x2-x1):
103         for j in range(1,y2-y1):
104             delta[j][i] = ar[:,i][j]-ar[:,i][j-1]
105         for k in range(0,y2-y1):
106             if abs(delta[k][i]) > 0.8*2*np.pi:
107                 steps[k:,i] = steps[k:,i] -
                    ↪  (np.sign(delta[k][i])*2*np.pi)
108     clean = ar + steps
109     return clean
110
111 def do_smooth_x(ar):
112     delta = np.zeros((y2-y1,x2-x1))
113     steps = np.zeros((y2-y1,x2-x1))
114     clean = np.zeros((y2-y1,x2-x1))
115     for i in range(0,y2-y1):
116         for j in range(1,x2-x1):
```

```
117             delta[i][j] = ar[i][j]-ar[i][j-1]
118         for k in range(0,x2-x1):
119             if abs(delta[i][k]) > 0.8*2*np.pi:
120                 steps[i][k:] = steps[i][k:] -
                    ↪  (np.sign(delta[i][k])*2*np.pi)
121     clean = ar + steps
122     return clean
123
124 def clean_up_x(ar):
125     for i in range(0,y2-y1):
126         for j in range(1,x2-x1):
127             if ar[i][j] - ar[i][j-1] < -0.8*2*np.pi:
128                 ar[i][j] = ar[i][j] + (2*np.pi)
129             if ar[i][j] - ar[i][j-1] > 0.8*2*np.pi:
130                 ar[i][j] = ar[i][j] - (2*np.pi)
131     return ar
132
133 def clean_up_y(ar):
134     for i in range(0,x2-x1):
135         for j in range(1,y2-y1):
136             if ar[j][i] - ar[j-1][i] < -0.8*2*np.pi:
137                 ar[j][i] = ar[j][i] + (2*np.pi)
138             if ar[j][i] - ar[j-1][i] > 0.8*2*np.pi:
139                 ar[j][i] = ar[j][i] - (2*np.pi)
140     return ar
141
142 def clean_phase(campaign, before_image_no, shot_image_no):
143     net_phase = get_net_phase(campaign, before_image_no,
      ↪  shot_image_no)
144     clean_net_phase_y = clean_up_y(net_phase)
145     clean_net_phase_yx = clean_up_x(clean_net_phase_y)
146     return clean_net_phase_yx
147
148 def zero_phase(campaign, before_image_no, shot_image_no):
149     clean_net_phase = clean_phase(campaign, before_image_no,
      ↪  shot_image_no)
```

```
150     for i in range(0,y2-y1):
151         zero_point = clean_net_phase[i][x2-x1-1]
152         clean_net_phase[i] = clean_net_phase[i] - zero_point
153     return clean_net_phase
154 
155 def get_areal_density(campaign, before_image_no,
    ↪ shot_image_no):
156     clean_net_phase = zero_phase(campaign, before_image_no,
        ↪ shot_image_no)
157     areal_density = clean_net_phase * S
158     return areal_density
159 
160 def noise_removal(ar):
161     low_values_flags = ar < -5e-4
162     ar[low_values_flags] = 0
163     high_values_flags = ar > 5e-4
164     ar[high_values_flags] = 0
165     return ar
166 
167 def get_density(campaign, before_image_no, shot_image_no):
168     areal_density = get_areal_density(campaign,
        ↪ before_image_no, shot_image_no)
169     density = abel.basex.basex_transform(areal_density, dr=1)
170     density = density*(x2-x1)/radius
171     density = noise_removal(density)
172     density = density*1.5e22
173     return density
174 
175 def get_density_ma(campaign, before_image_no, shot_image_no):
176     density = get_density(campaign, before_image_no,
        ↪ shot_image_no)
177     density_ma = np.zeros((y2-y1,x2-x1))
178     for i in range(0,y2-y1):
179         temp = {'r':list(range(x2-x1)), 'density':density[i]}
180         ma = pd.DataFrame(temp)
181         ma['ma'] = ma.iloc[:,1].rolling(250).mean()
```

```
182             ma = [i for i in ma['ma']]
183             density_ma[i] = ma
184         return density_ma
185 
186 def get_linear_density(campaign, before_image_no,
    ↪  shot_image_no):
187         density = get_density(campaign, before_image_no,
        ↪  shot_image_no)
188         linear_density = []
189         z = np.linspace(0,2,y2-y1)
190         r = list(np.linspace(0,radius,x2-x1))
191         for i in range(0,x2-x1):
192             linear_density.append(cumtrapz(density[:,i], z,
            ↪  initial=0)[y2-y1-1])
193         linear_density = [i*j*2*np.pi for (i,j) in
        ↪  zip(linear_density,r)]
194         return linear_density
195 
196 def get_linear_density_ma(campaign, before_image_no,
    ↪  shot_image_no):
197         linear_density = get_linear_density(campaign,
        ↪  before_image_no, shot_image_no)
198         linear_density_ma = []
199         temp = {'z':list(range(x2-x1)),
        ↪  'linear_density':linear_density}
200         ma = pd.DataFrame(temp)
201         ma['ma'] = ma.iloc[:,1].rolling(50).mean()
202         linear_density_ma = [i for i in ma['ma']]
203         return linear_density_ma
204 
```

APPENDIX E

Fast Framing Camera Analysis

E.1 Image Analysis

The fast framing camera acquires 12 frames with nanosecond resolution, which allows for imaging the implosion trajectory of the gas-puff z-pinch. A computer code was written to calculate the radius of the liner and the standard deviation in making this determination (see Sec. E.2). The code first requires user input to define the anode and cathode planes in just one of the 12 frames. Since this height is known in real units (i.e., 2 cm), all other length scales can be calculated. Defining these planes also allows the code to focus on the region of interest, namely a 1 cm height in the center of the target region (i.e., 0.5 cm above the cathode plane and 0.5 sm below the anode plane). The user then defines the left edge and right edge of each frame. The difference between the average pixel location of each edge can be converted to the liner diameter using the known height of the experiment. Additionally, the standard deviation in the definition of the edge is also calculated and can be used as a proxy for instability growth rates. A characteristic sequence of raw fast framing camera images and the corresponding liner definitions is shown in Fig. E.1

E.2 image_analysis.py

```
1 import os
2 import re
3 import cv2
4 import matplotlib.pyplot as plt
5 import numpy as np
6 import csv
7
8 class analyze_images:
9
```

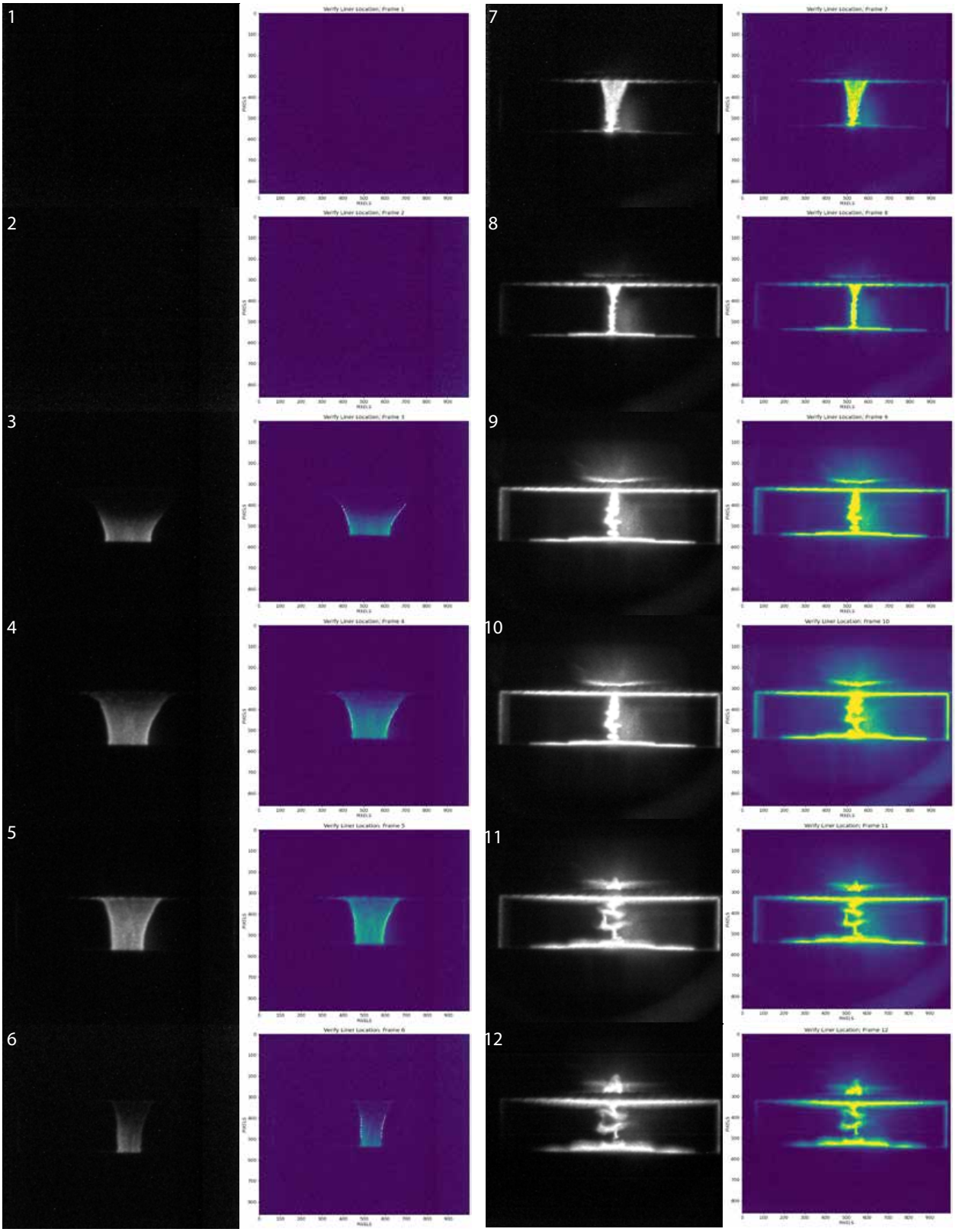

Figure E.1: The sequence of images showing the 12 raw fast framing camera images and the corresponding user defined liner edges. Note that the trajectory is only mapped from when it is visible (frame 3) to when the pinch stagnates (frame 8); the liner is not defined when the pinch begins to dissipate post-stagnation.

```
10      def __init__(self, date, shot):
11          self.date = str(date)
12          self.shot = '0' + str(shot)
13
14      def get_data(self):
15          shot_dir = self.date + '/' + self.shot + '/Shot_' +
             ↪  self.shot + '/'
16          if os.path.isdir(shot_dir) == True:
17              frames = []
18              for file in os.listdir(shot_dir):
19                  if file.startswith('Sequence') and
                     ↪  file.endswith('.jpg'):
20                      frames.append(file)
21              frames.sort(key = lambda x:
                 ↪  int(re.findall(r'[0-9]+', x)[-1]))
22              frames = [shot_dir + file for file in frames]
23          else:
24              print('Shot does not have frames...')
25          return frames
26
27      def get_top_bot(self):
28          frames = self.get_data()
29          picture = cv2.imread(frames[8], flags = 0)
30          font = {'size':12}
31          plt.rc('font', **font)
32          plt.figure(figsize = (10,10))
33          plt.imshow(picture)
34          plt.xticks(np.arange(0, len(picture[0]), 100))
35          plt.yticks(np.arange(0, len(picture), 100))
36          plt.xlabel('PIXELS')
37          plt.ylabel('PIXELS')
38          plt.title('Define Top and Bottom; Frame 8')
39          clicked_points = plt.ginput(2,0)
40          plt.show()
41          plt.close()
42          top_bot_points = []
```

```
43          for j in range(len(clicked_points)):
44              x, y = clicked_points[j]
45              top_bot_points.append((x,y))
46          top_point = top_bot_points[0][1]
47          bot_point = top_bot_points[1][1]
48          return top_point, bot_point
49
50      def get_liner(self):
51          frames = self.get_data()
52          top_point, bot_point = self.get_top_bot()
53          shot_dir = self.date + '/' + self.shot + '/Shot_' +
            ↪  self.shot + '/'
54          pictures = [cv2.imread(file, flags = 0) for file in
            ↪  frames]
55          top_line_point = top_point + (0.5*(bot_point -
            ↪  top_point)/2)
56          bot_line_point = bot_point - (0.5*(bot_point -
            ↪  top_point)/2)
57          left_liner = []
58          right_liner = []
59          i = 0
60          while i < len(pictures):
61              happy = 'no'
62              while happy == 'no':
63                  font = {'size':12}
64                  plt.rc('font', **font)
65                  plt.figure(figsize = (10,10))
66                  plt.imshow(pictures[i])
67                  plt.axhline(top_line_point, color='white',
                    ↪  linewidth=0.5)
68                  plt.axhline(bot_line_point, color='white',
                    ↪  linewidth=0.5)
69                  plt.xticks(np.arange(0, len(pictures[i][0]),
                    ↪  100))
70                  plt.yticks(np.arange(0, len(pictures[i]), 100))
71                  plt.xlabel('PIXELS')
```

```
72                  plt.ylabel('PIXELS')
73                  plt.title('Define Liner (Left); Frame ' +
                     ↪  str(i+1))
74                  clicked_points = plt.ginput(-1)
75                  plt.show()
76                  plt.close()
77                  left_points_sublist = []
78                  for j in range(len(clicked_points)):
79                      x,y = clicked_points[j]
80                      left_points_sublist.append((x,y))
81                  left_liner.append(left_points_sublist)
82                  font = {'size':12}
83                  plt.rc('font', **font)
84                  plt.figure(figsize = (10,10))
85                  plt.imshow(pictures[i])
86                  plt.axhline(top_line_point, color='white',
                     ↪  linewidth=0.5)
87                  plt.axhline(bot_line_point, color='white',
                     ↪  linewidth=0.5)
88                  plt.xticks(np.arange(0, len(pictures[i][0]),
                     ↪  100))
89                  plt.yticks(np.arange(0, len(pictures[i]), 100))
90                  plt.xlabel('PIXELS')
91                  plt.ylabel('PIXELS')
92                  plt.title('Define Liner (Right); Frame ' +
                     ↪  str(i+1))
93                  clicked_points = plt.ginput(-1)
94                  plt.show()
95                  plt.close()
96                  right_points_sublist = []
97                  for j in range(len(clicked_points)):
98                      x,y = clicked_points[j]
99                      right_points_sublist.append((x,y))
100                 right_liner.append(right_points_sublist)
101                 font = {'size':12}
102                 plt.rc('font', **font)
```

```
103                 plt.figure(figsize = (10,10))
104                 if len(left_points_sublist) > 0:
105                     plt.plot(*zip(*left_points_sublist), 'o',
                        ↪  markersize=1, color='w')
106                 if len(right_points_sublist) > 0:
107                     plt.plot(*zip(*right_points_sublist), 'o',
                        ↪  markersize=1, color='w')
108                 plt.imshow(pictures[i])
109                 plt.xticks(np.arange(0, len(pictures[i][0]),
                    ↪  100))
110                 plt.yticks(np.arange(0, len(pictures[i]), 100))
111                 plt.xlabel('PIXELS')
112                 plt.ylabel('PIXELS')
113                 plt.title('Verify Liner Location; Frame ' +
                    ↪  str(i+1))
114                 clicked_points = plt.ginput(-1)
115                 plt.show()
116                 plt.savefig(shot_dir + '/defined_frame_' +
                    ↪  str(i+1) + '.jpg', bbox_inches='tight')
117                 plt.close()
118                 if len(clicked_points) == 0:
119                     happy = 'yes'
120                 else:
121                     happy = 'no'
122             i += 1
123         return top_point, bot_point, left_liner, right_liner
124
125     def get_r_t(self):
126         top_point, bot_point, left_liner, right_liner =
            ↪  self.get_liner()
127         pixel_height = bot_point - top_point
128         left_x = []
129         right_x = []
130         left_var_x = []
131         right_var_x = []
132         for i in range(len(left_liner)):
```

```
133             temp_x = []
134             for j in left_liner[i]:
135                 temp_x.append(j[0])
136             left_x.append(np.mean(temp_x))
137             left_var_x.append(np.var(temp_x))
138             temp_x = []
139             for j in right_liner[i]:
140                 temp_x.append(j[0])
141             right_x.append(np.mean(temp_x))
142             right_var_x.append(np.var(temp_x))
143         liner_radius = [(i-j)/2 for i,j in zip(right_x,
            ↪ left_x)]
144         liner_radius = [i*2/pixel_height for i in liner_radius]
145         left_var_x = [i*pow(2/pixel_height,2) for i in
            ↪ left_var_x]
146         right_var_x = [i*pow(2/pixel_height,2) for i in
            ↪ right_var_x]
147         save_dir = self.date + '/' + self.shot + '/'
148         details = ['Frame 1', 'Frame 2', 'Frame 3', 'Frame 4',
            ↪ 'Frame 5', 'Frame 6', 'Frame 7', 'Frame 8', 'Frame
            ↪ 9', 'Frame 10', 'Frame 11', 'Frame 12']
149         print(liner_radius)
150         with open(save_dir + 'r_t.csv', 'w') as f:
151             write = csv.writer(f)
152             write.writerow(details)
153             write.writerow(liner_radius)
154             write.writerow(left_var_x)
155             write.writerow(right_var_x)
156
```

BIBLIOGRAPHY

[1] S. A. Slutz, M. C. Herrmann, R. A. Vesey, A. B. Sefkow, D. B. Sinars, D. C. Rovang, K. J. Peterson, and M. E. Cuneo. Pulsed-power-driven cylindrical liner implosions of laser preheated fuel magnetized with an axial field. *Physics of Plasmas*, 17(5):056303, 2010.

[2] M. E. Cuneo, M. C. Herrmann, D. B. Sinars, S. A. Slutz, W. A. Stygar, R. A. Vesey, A. B. Sefkow, G. A. Rochau, G. A. Chandler, J. E. Bailey, J. L. Porter, R. D. McBride, D. C. Rovang, M. G. Mazarakis, E. P. Yu, D. C. Lamppa, K. J. Peterson, C. Nakhleh, S. B. Hansen, and M. Matzen. Magnetically driven implosions for inertial confinement fusion at sandia national laboratories. *IEEE Transactions on Plasma Science*, 40:3222–3245, 2012.

[3] S. A. Slutz and R. A. Vesey. High-gain magnetized inertial fusion. *Phys. Rev. Lett.*, 108:025003, 2012.

[4] M. R. Gomez, S. A. Slutz, A. B. Sefkow, D. B. Sinars, K. D. Hahn, S. B. Hansen, E. C. Harding, P. F. Knapp, P. F. Schmit, C. A. Jennings, T. J. Awe, M. Geissel, D. C. Rovang, G. A. Chandler, G. W. Cooper, M. E. Cuneo, A. J. Harvey-Thompson, M. C. Herrmann, M. H. Hess, O. Johns, D. C. Lamppa, M. R. Martin, R. D. McBride, K. J. Peterson, J. L. Porter, G. K. Robertson, G. A. Rochau, C. L. Ruiz, M. E. Savage, I. C. Smith, W. A. Stygar, and R. A. Vesey. Experimental demonstration of fusion-relevant conditions in magnetized liner inertial fusion. *Phys. Rev. Lett.*, 113:155003, 2014.

[5] R. W. Lemke, D. H. Dolan, D. G. Dalton, J. L. Brown, K. Tomlinson, G. R. Robertson, M. D. Knudson, E. Harding, A. E. Mattsson, J. H. Carpenter, R. R. Drake, K. Cochrane, B. E. Blue, A. C. Robinson, and T. R. Mattsson. Probing off-hugoniot states in ta, cu, and al to 1000 gpa compression with magnetically driven liner implosions. *Journal of Applied Physics*, 119(1):015904, 2016.

[6] M. R. Martin, R. W. Lemke, R. D. McBride, J. P. Davis, D. H. Dolan, M. D. Knudson, K. R. Cochrane, D. B. Sinars, I. C. Smith, M. Savage, W. A. Stygar, K. Killebrew, D. G. Flicker, and M. C. Herrmann. Solid liner implosions on z for producing multi-megabar, shockless compressions. *Physics of Plasmas*, 19(5):056310, 2012.

[7] J. E. Bailey, G. A. Chandler, D. Cohen, M. E. Cuneo, M. E. Foord, R. F. Heeter, D. Jobe, P. W. Lake, J. J. MacFarlane, T. J. Nash, D. S. Nielson, R. Smelser, and J. Torres. Radiation science using z-pinch x rays. *Physics of Plasmas*, 9(5):2186–2194, 2002.

[8] G. A. Rochau, J. E. Bailey, Y. Maron, G. A. Chandler, G. S. Dunham, D. V. Fisher, V. I. Fisher, R. W. Lemke, J. J. MacFarlane, K. J. Peterson, D. G. Schroen, S. A. Slutz, and

E. Stambulchik. Radiating shock measurements in the z-pinch dynamic hohlraum. *Phys. Rev. Lett.*, 100:125004, 2008.

[9] G. A. Rochau, J. E. Bailey, R. E. Falcon, G. P. Loisel, T. Nagayama, R. C. Mancini, I. Hall, D. E. Winget, M. H. Montgomery, and D. A. Liedahl. Zapp: The z astrophysical plasma properties collaboration. *Physics of Plasmas*, 21(5):056308, 2014.

[10] B. M. Koval'chuk, V. A. Vizir', A. A. Kim, E. V. Kumpyak, S. V. Loginov, A. N. Bastrikov, V. V. Chervyakov, N. V. Tsoi, P. Monjaux, and D. Kh'yui. Fast primary storage device utilizing a linear pulse transformer. *Russian Physics Journal*, 40(12):1142–1153, 1997.

[11] A. A. Kim, B. M. Kovalchuk, E. V. Kumpjak, and N. V. Zoi. 0.75 MA, 400 ns rise time LTD stage. *Digest of Technical Papers, 12th IEEE International Pulsed Power Conference*, 2:955–958, 1999.

[12] A. A. Kim, M. G. Mazarakis, V. A. Sinebryukhov, B. M. Kovalchuk, V. A. Visir, S. N. Volkov, F. Bayol, A. N. Bastrikov, V. G. Durakov, S. V. Frolov, V. M. Alexeenko, D. H. McDaniel, W. E. Fowler, K. LeChien, C. Olson, W. A. Stygar, K. W. Struve, J. Porter, and R. M. Gilgenbach. Development and tests of fast 1-ma linear transformer driver stages. *Phys. Rev. ST Accel. Beams*, 12:050402, 2009.

[13] J. D. Douglass, B. T. Hutsel, J. J. Leckbee, T. D. Mulville, B. S. Stoltzfus, M. L. Wisher, M. E. Savage, W. A. Stygar, E. W. Breden, J. D. Calhoun, M. E. Cuneo, D. J. De Smet, R. J. Focia, R. J. Hohlfelder, D. M. Jaramillo, O. M. Johns, M. C. Jones, A. C. Lombrozo, D. J. Lucero, J. K. Moore, J. L. Porter, S. D. Radovich, S. A. Romero, M. E. Sceiford, M. A. Sullivan, C. A. Walker, J. R. Woodworth, N. T. Yazzie, M. D. Abdalla, M. C. Skipper, and C. Wagner. 100 gw linear transformer driver cavity: Design, simulations, and performance. *Phys. Rev. Accel. Beams*, 21:120401, 2018.

[14] Yang Li, Liang Sheng, Jian Wu, Xingwen Li, Jizhen Zhao, Mei Zhang, Yuan Yuan, and Bodong Peng. Influence of insulating coating on aluminum wire explosions. *Physics of Plasmas*, 21:102513–12704, 2014.

[15] D. J. Ampleford, S. B. Hansen, C. A. Jennings, B. M.c Jones, C. A. Coverdale, A. J. Harvey-Thompson, G. A. Rochau, G. S. Dunham, N. Moore, E. C. Harding, M. E. Cuneo, Y. K. Chong, R. E. Clark, N. Ouart, J. W. Thornhill, J. L. Giuliani, and J. P. Apruzese. Opacity and gradients in aluminum wire array z-pinch implosions on the z pulsed power facility. *Physics of Plasmas*, 21:031201, 2014.

[16] D. B. Sinars, S. A. Slutz, M. C. Herrmann, R. D. McBride, M. E. Cuneo, K. J. Peterson, R. A. Vesey, C. Nakhleh, B. E. Blue, K. Killebrew, D. Schroen, K. Tomlinson, A. D. Edens, M. R. Lopez, I. C. Smith, J. Shores, V. Bigman, G. R. Bennett, B. W. Atherton, M. Savage, W. A. Stygar, G. T. Leifeste, and J. L. Porter. Measurements of magneto-rayleigh-taylor instability growth during the implosion of initially solid al tubes driven by the 20-ma, 100-ns z facility. *Physical review letters*, 105:185001, 2010.

[17] G. A. Rochau, J. E. Bailey, G. A. Chandler, G. Cooper, G. S. Dunham, P. W. Lake, R. J. Leeper, R. W. Lemke, T. A. Mehlhorn, A. Nikroo, K. J. Peterson, C. L. Ruiz, D. G. Schroen,

S. A. Slutz, D. Steinman, W. A. Stygar, and W. Varnum. High performance capsule implosions driven by the z-pinch dynamic hohlraum. *Plasma Physics and Controlled Fusion*, 49(12B):B591–B600, 2007.

[18] M. E. Cuneo. Double z-pinch-driven hohlraums: Symmetric icf capsule implosions and wire-array z-pinch source physics. *IEEE Conference Record - Abstracts. 2005 IEEE International Conference on Plasma Science*, pages 195–195, 2005.

[19] N. V. Filippov, T. I. Filippova, and V. P. Vinogradov. Dense high-temperature plasma in a non-cylindrical z-pinch compression. *Plasma Physics and Controlled Nuclear Fusion Research: Conference Proceedings, Salzburg, 4-9 September 1961: Translated from Preprints of Russian Papers Presented at the Conference*, page 311, 1963.

[20] J. W. Mather. Investigation of the high-energy acceleration mode in the coaxial gun. *The Physics of Fluids*, 7(11):S28–S34, 1964.

[21] J. Shiloh, A. Fisher, and N. Rostoker. Z-pinch of a gas jet. *Phys. Rev. Lett.*, 40:515–518, 1978.

[22] P. G. Burkhalter, J. Shiloh, A. Fisher, and R. D. Cowan. X-ray spectra from a gas-puff z-pinch device. *Journal of Applied Physics*, 50(7):4532–4540, 1979.

[23] J. Bailey, Y. Ettinger, A. Fisher, and N. Rostoker. Gas-puff z pinches with d2 and d2-ar mixtures. *Applied Physics Letters*, 40:460 – 462, 1982.

[24] C. Stallings, K. Childers, I. Roth, and R. Schneider. Imploding argon plasma experiments. *Applied Physics Letters*, 35(7):524–526, 1979.

[25] T. F. Chang, A. Fisher, and A. Van Drie. X-ray results from a modified nozzle and double gas puff z pinch. *Journal of Applied Physics*, 69(6):3447–3450, 1991.

[26] E. Ruden, H. Rahman, A. Fisher, and N. Rostoker. Stability enhancement of a low initial density hollow gas-puff z pinch by e- beam preionization. *Journal of Applied Physics*, 61:1311 – 1316, 1987.

[27] J. L. Giuliani and R. J. Commisso. A review of the gas-puff z-pinch as an x-ray and neutron source. *IEEE Transactions on Plasma Science*, 43(8):2385–2453, 2015.

[28] R. B. Baksht, A. G. Russkikh, and A. A. Chagin. Study of the effect of pre-ionization on current sharing between sheaths of a double-cascade gas puff. *Plasma Physics Reports*, 23, 1997.

[29] A. Rousskikh, R. Baksht, A. Labetsky, A. Shishlov, and A. Fedyunin. Effect of pre-ionization on the implosion dynamics of single and double argon gas puffs. *Plasma Physics Reports*, 25:527–529, 1999.

[30] B. Moosman, B. V. Weber, S. J. Stephanakis, R. J. Commisso, and A. Fisher. Measurements of gas pre-ionization for plasma radiation sources. *Review of Scientific Instruments*, 70(1):672–676, 1999.

[31] J. S. Levine, P. L. Coleman, B. H. Failor, J. C. Riordan, Y. Song, H. M. Sze, C. A. Coverdale, C. Deeney, J. S. McGurn, J. P. Apruzese, J. Davis, B. Moosman, J. W. Thornhill, A. L. Velikovich, B. V. Weber, D. Bell, and R. Schneider. Long-implosion plasma radiation sources using "solid-fill" nozzles. *Physics of Plasmas*, 8(2):533–541, 2001.

[32] R. D. McBride, W. A. Stygar, M. E. Cuneo, D. B. Sinars, M. G. Mazarakis, J. J. Leckbee, M. E. Savage, B. T. Hutsel, J. D. Douglass, M. L. Kiefer, B. V. Oliver, G. R. Laity, M. R. Gomez, D. A. Yager-Elorriaga, S. G. Patel, B. M. Kovalchuk, A. A. Kim, P. . Gourdain, S. N. Bland, S. Portillo, S. C. Bott-Suzuki, F. N. Beg, Y. Maron, R. B. Spielman, D. V. Rose, D. R. Welch, J. C. Zier, J. W. Schumer, J. B. Greenly, A. M. Covington, A. M. Steiner, P. C. Campbell, S. M. Miller, J. M. Woolstrum, N. B. Ramey, A. P. Shah, B. J. Sporer, N. M. Jordan, Y. Y. Lau, and R. M. Gilgenbach. A primer on pulsed power and linear transformer drivers for high energy density physics applications. *IEEE Transactions on Plasma Science*, 46(11):3928–3967, 2018.

[33] D.D. Ryutov, M.S. Derzon, and M.K. Matzen. The physics of fast Z pinches. *Rev. Mod. Phys.*, 72:167–223, 2000.

[34] J. Katzenstein. Optimum coupling of imploding loads to pulse generators. *Journal of Applied Physics*, 52(2):676–680, 1981.

[35] W. H. Bennett. Magnetically self-focussing streams. *Phys. Rev.*, 45:890–897, 1934.

[36] R. S. Pease. Equilibrium characteristics of a pinched gas discharge cooled by bremsstrahlung radiation. *Proceedings of the Physical Society. Section B*, 70(1):11–23, 1957.

[37] T. Miyamoto. Analysis of high-density z-pinches by a snowplow energy equation. *Nuclear Fusion*, 24:337, 2011.

[38] J. E. Allen. An elementary theory of the transient pinched discharge. *Proceedings of the Physical Society. Section B*, 70(1):24–30, 1957.

[39] P. Coleman, J. Thompson, M. Krishnan, and B. L. Bures. An alternative concept for the structure of an x-ray emitting z -pinch. *IEEE Transactions on Plasma Science*, 38(4):626–630, 2010.

[40] R. D. McBride, T. A. Shelkovenko, S. A. Pikuz, D. A. Hammer, J. B. Greenly, B. R. Kusse, J. D. Douglass, P. F. Knapp, K. S. Bell, I. C. Blesener, and D. A. Chalenski. Implosion dynamics and radiation characteristics of wire-array z pinches on the cornell beam research accelerator. *Physics of Plasmas*, 16(1):012706, 2009.

[41] D. Mosher, M. Krishnan, N. Qi, P. L. Coleman, E. M. Waisman, and H. Sze. Current scaling of optimum k-shell x-ray yield and load mass applied to argon gas-puff z-pinches. *Digest of Papers. 2001 IEEE International Conference on Plasma Science and International Pulsed Power Conference.*, 1:277–280, 2001.

[42] A. L. Velikovich, R. W. Clark, J. Davis, Y. K. Chong, C. Deeney, C. A. Coverdale, C. L. Ruiz, G. W. Cooper, A. J. Nelson, J. Franklin, and L. I. Rudakov. Z-pinch plasma neutron sources. *Physics of Plasmas*, 14(2):022701, 2007.

[43] R. M. Gilgenbach, M. R. Gomez, J. C. Zier, W. W. Tang, D. M. French, Y. Y. Lau, M. G. Mazarakis, M. E. Cuneo, M. D. Johnston, B. V. Oliver, T. A. Mehlhorn, A. A. Kim, and V. A. Sinebryukhov. Maize: a 1 ma ltd-driven z-pinch at the university of michigan. *AIP Conference Proceedings*, 1088(1):259–262, 2009.

[44] M. R. Gomez. *Experimental Examination of Plasma Formation and Current Loss in Post-Hole Convolutes*. PhD thesis, University of Michigan, 2011.

[45] A. P. Shah, P. C. Campbell, S. M. Miller, J. M. Woolstrum, B. J. Sporer, S. G. Patel, N. M. Jordan, R. M. Gilgenbach, and R. D. McBride. Optimization of switch diagnostics on the maize linear transformer driver. *Review of Scientific Instruments*, 90(12):124707, 2019.

[46] A. L. Velikovich, F. L. Cochran, and J. Davis. Suppression of rayleigh-taylor instability in Z-pinch loads with tailored density profiles. *Phys. Rev. Lett.*, 77:853–856, 1996.

[47] N. Qi, E. Rosenberg, P. A. Gourdain, P. Grouchy, B. R. Kusse, D. A. Hammer, K. Bell, T. A Shelkovenko, W. M. Potter, L. Atoyan, A. Cahill, M. Evans, J. B. Greenly, C. Hoyt, S. A. Pikuz, P. Schrafel, E. Kroupp, A. Fisher, and Y. Maron. Study of gas-puff z-pinches on cobra. *Physics of Plasmas*, 21:112702, 2014.

[48] H. Sze, J. Banister, B. H. Failor, J. S. Levine, N. Qi, A. L. Velikovich, J. Davis, D. Lojewski, and P. Sincerny. Efficient radiation production in long implosions of structured gas-puff z pinch loads from large initial radius. *Phys. Rev. Lett.*, 95:105001, 2005.

[49] R. J. Commisso, J. P. Apruzese, D. Mosher, D. P. Murphy, B. V. Weber, J. W. Banister, B. H. Failor, J. S. Levine, N. Qi, H. M. Sze, A. Bixler, P. L. Coleman, A. Jarema, J. Knight, S. Lee, M. Krishnan, J. Thompson, K. Wilson, C. A. Coverdale, and C. Deeney. Energetics of a long-implosion-time, 12-cm-diameter argon-gas-puff z pinch at 6.5 ma. *2007 IEEE International Pulsed Power Conference*, 2:1773–1779, 2007.

[50] M. Krishnan, K. W. Elliott, R. Madden, P. L. Coleman, J. Thompson, A. Bixler, D. C. Lamppa, J McKenney, T. Strizic, D. Johnson, O. Johns, M. Vigil, B. M. Jones, D. Ampleford, M. E. Savage, M. E. Cuneo, and M. C. Jones. Architecture, implementation, and testing of a multiple-shell gas injection system for high current implosions on the z accelerator. *The Review of scientific instruments*, 84:063504, 2013.

[51] P. C. Campbell, J. M. Woolstrum, F. Antoulinakis, T. M. Jones, D. A. Yager-Elorriaga, S. M. Miller, N. M. Jordan, Y. Y. Lau, R. M. Gilgenbach, and R. D. Mcbride. Diagnostic and power feed upgrades to the maize facility. *IEEE Transactions on Plasma Science*, 46(11):3973–3981, 2018.

[52] C. L. Ruiz, J. D. Styron, D. L. Fehl, K. D. Hahn, B. McWatters, M. A. Mangan, G. W. Cooper, J. D. Vaughan, G. A. Chandler, B. M. Jones, J. A. Torres, S. A. Slutz, D. J. Ampleford, M. R. Gomez, E. Harding, A. J. Harvey-Thompson, and P. F. Knapp. Novel beryllium-scintillator, neutron-fluence detector for magnetized liner inertial fusion experiments. *Phys. Rev. Accel. Beams*, 22:042901, 2019.

[53] E. G. Harris. Rayleigh-taylor instabilities of a collapsing cylindrical shell in a magnetic field. *The Physics of Fluids*, 5(9):1057–1062, 1962.

[54] Y. Y. Lau, J. C. Zier, I. M. Rittersdorf, M. R. Weis, and R. M. Gilgenbach. Anisotropy and feedthrough in magneto-rayleigh-taylor instability. *Phys. Rev. E*, 83:066405, 2011.

[55] M. R. Weis, P. Zhang, Y. Y. Lau, I. M. Rittersdorf, J. C. Zier, R. M. Gilgenbach, M. H. Hess, and K. J. Peterson. Temporal evolution of surface ripples on a finite plasma slab subject to the magneto-rayleigh-taylor instability. *Physics of Plasmas*, 21(12):122708, 2014.

[56] M. R. Weis, P. Zhang, Y. Y. Lau, P. F. Schmit, K. J. Peterson, M. Hess, and R. M. Gilgenbach. Coupling of sausage, kink, and magneto-rayleigh-taylor instabilities in a cylindrical liner. *Physics of Plasmas*, 22(3):032706, 2015.

[57] M. Sadowski, H. Herold, H. Schmidt, and M. Shakhatre. Filamentary structure of the pinch column in plasma focus discharges. *Physics Letters A*, 105(3):117–123, 1984.

[58] M. G. Haines. Physics of high-density z-pinch plasmas. *Journal of Plasma Physics*, 64(3):309–310, 2000.

[59] M. G. Haines, P. D. LePell, C. A. Coverdale, B. Jones, C. Deeney, and J. P. Apruzese. Ion viscous heating in a magnetohydrodynamically unstable z-pinch at over 2×10^9 kelvin. *Phys. Rev. Lett.*, 96:075003, 2006.

[60] J. L. Giuliani, J. W. Thornhill, J. P. Apruzese, B. Jones, A. J. Harvey-Thompson, D. J. Ampleford, A. Dasgupta, C. A. Jennings, S. B. Hansen, N. W. Moore, D. C. Lamppa, C. A. Coverdale, M. E. Cuneo, and G. A. Rochau. Two dimensional rmhd modeling of effective ion temperatures in recent zr argon experiments. *AIP Conference Proceedings*, 1639(1):31–34, 2014.

[61] E. Kroupp, E. Stambulchik, A. Starobinets, D. Osin, V. I. Fisher, D. Alumot, Y. Maron, S. Davidovits, N. J. Fisch, and A. Fruchtman. Turbulent stagnation in a z-pinch plasma. *Phys. Rev. E*, 97:013202, Jan 2018.

[62] A. M. Steiner, D. A. Yager-Elorriaga, S. G. Patel, N. M. Jordan, R. M. Gilgenbach, A. S. Safronova, V. L. Kantsyrev, V. V. Shlyaptseva, I. Shrestha, and M. T. Schmidt-Petersen. Determination of plasma pinch time and effective current radius of double planar wire array implosions from current measurements on a 1-ma linear transformer driver. *Physics of Plasmas*, 23(10):101206, 2016.

[63] E. M. Waisman, D. B. Reisman, B. S. Stoltzfus, W. A. Stygar, M. E. Cuneo, T. A. Haill, J.-P. Davis, J. L. Brown, C. T. Seagle, and R. B. Spielman. Optimization of current waveform tailoring for magnetically driven isentropic compression experiments. *Review of Scientific Instruments*, 87(6):063906, 2016.

[64] W. A. Stygar, T. J. Awe, J. E. Bailey, N. L. Bennett, E. W. Breden, E. M. Campbell, R. E. Clark, R. A. Cooper, M. E. Cuneo, J. B. Ennis, D. L. Fehl, T. C. Genoni, M. R. Gomez, G. W. Greiser, F. R. Gruner, M. C. Herrmann, B. T. Hutsel, C. A. Jennings, D. O. Jobe, B. M. Jones,

M. C. Jones, P. A. Jones, P. F. Knapp, J. S. Lash, K. R. LeChien, J. J. Leckbee, R. J. Leeper, S. A. Lewis, F. W. Long, D. J. Lucero, E. A. Madrid, M. R. Martin, M. K. Matzen, M. G. Mazarakis, R. D. McBride, G. R. McKee, C. L. Miller, J. K. Moore, C. B. Mostrom, T. D. Mulville, K. J. Peterson, J. L. Porter, D. B. Reisman, G. A. Rochau, G. E. Rochau, D. V. Rose, D. C. Rovang, M. E. Savage, M. E. Sceiford, P. F. Schmit, R. F. Schneider, J. Schwarz, A. B. Sefkow, D. B. Sinars, S. A. Slutz, R. B. Spielman, B. S. Stoltzfus, C. Thoma, R. A. Vesey, P. E. Wakeland, D. R. Welch, M. L. Wisher, and J. R. Woodworth. Conceptual designs of two petawatt-class pulsed-power accelerators for high-energy-density-physics experiments. *Phys. Rev. ST Accel. Beams*, 18:110401, 2015.